Université de Neuchâtel

Institut de Microtechnique

Optical Properties of Nano-Structured Materials Studied by Means of Interferometric Techniques

Thèse

Présentée à la faculté des sciences
pour obtenir le grade de docteur ès science
par

Pierpasquale Tortora

Neuchâtel , septembre 2005

Thèse de l'Université de Neuchâtel

Date de soutenance : 6 Octobre 2005

Rapporteurs: Prof. Dr. R. Dändliker
Prof. Dr. H-P. Herzig (directeur de thèse)
Prof. Dr. D. Courjon
Prof. Dr. D. Sandoghdar

Mots-clés: Microscopie optique à balayage; interférométrie; détection hétérodyne; polarisation du champ optique; propagation des ondes; récupération de phase; analyse de Fourier complexe; guides d'onde; cristaux photoniques.

Keywords: Scanning near-field optical microscopy (SNOM); interferometry; heterodyne detection; field polarization; wave propagation; phase retrieval; complex Fourier analysis; photonic crystal waveguides.

Université de Neuchâtel

IMPRIMATUR POUR LA THESE

Optical properties of nanostructured materials studied by means of interferometric techniques

Pierpasquale TORTORA

UNIVERSITE DE NEUCHATEL

FACULTE DES SCIENCES

La Faculté des sciences de l'Université de Neuchâtel,
sur le rapport des membres du jury

MM. H.-P. Herzig (directeur de thèse),
R. Dändliker,
V. Sandoghdar (ETH Zürich),
et D. Courjon (Besançon F)

autorise l'impression de la présente thèse.

Neuchâtel, le 25 octobre 2005

Le doyen :

J.-P. Derendinger

Faculté des Sciences
■ Rue Emile-Argand 11 ■ CP 2 ■ CH-2007 Neuchâtel
■ Téléphone : +41 32 718 21 00 ■ Fax : +41 32 718 21 03 ■ E-mail : secretariat.sciences@unine.ch ■ www.unine.ch

Introduction

In science one generally discriminates between pure and applied research. The first aims to study the fundamental principles of Nature, the second, to apply such principles to modern technology. After a season of deep changes in the scientific thought, consider the formulation of Quantum Mechanics, we live today an epoch of straightening and application of the acquired knowledge. The invention of lasers in the sixties, for instance, is one of the most significant examples of this process. Optics plays a crucial role in applied research. The interaction properties of electromagnetic waves with matter are at the basis of a wide set of devices employed in the field of telecommunications, computer science, data storage, robotics and many others. We can doubtless identify a trend in modern applied research: daily usage devices are, nowadays, demanded to be mobile, multifunctional and compact. The key word for all this is *miniaturization*. Several techniques, have been developed in the past decades to enable the fabrication of micro- and nano-structured materials. Photolithography, ion and e-beam, chemical etching are among the most used. In some cases, the structure features become too small to be observed by means of a classical microscope. This circumstance led to the invention of new kind of microscopes that allow to overcome the fundamental diffraction limit of lens-based optical systems: the Scanning Electron Microscope (SEM) and the Scanning Probe Optical Microscope (SPOM). A SEM provides information on the topography of the sample surface and is suitable for imaging surface of conductor and semiconductor materials. SPOMs present more extended properties and can be designed to investigate both topographical and optical properties of samples. Moreover, a SPOM is suitable to investigate hard materials as well as biological tissues.
The term microscope derives from the ancient Greek prefix *mikròs-* meaning small. However, small is a relative concept. In Optics, the wavelength of light is the parameter that determines how small an object is. When the light interacts with a sub-wavelength featured object, part of it is reflected or diffracted away from the object, part remains localized in the nearness of the surface. This last component is called evanescent and its intensity decreases exponentially with the distance from the object, therefore, it cannot be collected by the system of lenses of a classical microscope. Unfortunately, the evanescent light is associated to the finest details of the surface, which are then lost in a classical image. The SPOM overcomes this limitation by scanning a sub-wavelength probe in the near-field of the sample. The evanescent light is locally frustrated by the probe and is then propagated in the far-field, where it can be eventually collected. Therefore, this technique allows to recover the information generated by the evanescent field, and consequently improve the image resolution.
The key element in the use of the SPOM technique is the interaction of the probe with the investigated optical field. Both the theoretical and the experimental study of the probe-field interaction properties are complicated by the sub-wavelength characteristics of a scanning probe. We notice, therefore, a singular circumstance in which the investigating tool is itself an object of investigation. Actually, in the last years, the number of published works aimed to investigate the optical properties of scanning probes, is nearly comparable to the number of works in which

scanning probes are successfully used as an investigating tool.
The work presented in these pages reflects very well the state of the art of the SPOM technique. Actually, we avail ourselves of optical interferometric techniques in order to study the optical properties of nanostructured materials including different kinds of scanning probes.

In the first chapter, we introduce the working principles of a heterodyne SPOM (H-SPOM). In this case, the microscope is provided with a heterodyne detection system which enables simultaneous detection of amplitude and phase of the probed field. We introduce a suited optical set-up which provides the instrument with the additional beam-labeling property. The sample can be simultaneously illuminated by different beams whose contribution to the optical signal is discriminated by means of the heterodyne signals.
In the second and third chapter we investigate the polarization transfer properties of an uncoated tapered fiber probe in the case of transverse and longitudinally polarized fields respectively. For this purpose, we provide the H-SPOM with a detection system which is sensitive to the polarization state of the detected field. The study of the optical response to longitudinally polarized fields is of particular interest in SPOM microscopy. Actually, the near-field region is generally characterized by non-paraxial field configurations in which longitudinal components can be non negligible and, in same cases, prevalent.
In the fourth chapter, we use a high-resolution interference Mach-Zehnder microscope in order to study the electromagnetic properties of a microfabricated cantilevered fully-metal coated scanning probe designed to operate in illumination-collection mode. The microscope allows to detect simultaneously intensity and phase patterns. Comparison of the experimental results with a numerical model of the probe allowed us to identify selective injection techniques for the excitation of propagating modes in the probe structure.
Finally, in chapter 5, we employ a heterodyne scanning near-field optical microscope (H-SNOM), working at wavelength around $1.55\mu m$, for the investigation of the propagation properties of light in photonic crystal waveguides.

Contents

Chapter 1

Multiple-Heterodyne scanning probe optical microscope

1.1 Introduction

The idea to overcome the classical limits of the optical microscopy, by scanning a small aperture in the near-field region of the investigated sample, was first suggested by Synge in the far 1928 [1]. After several decades, the principle was successfully applied, in the visible domain, first by by Pohl *et al.* in a landmark work published in 1984 [3]. Since that time, various scanning near-field optical microscopes (SNOM's) with subwavelength resolutions have been developed, and a number of interesting applications of near-field microscopy have been demonstrated during the last two decades.
In this work, we deal with a recent evolution of SNOM which is named heterodyne-SNOM. The technique consists of integrating a scanning microscope into a Mach-Zehnder-like interferometer. In this case, both amplitude and phase of the probed field are simultaneously determined with a subwavelength resolution.(In the first section of this chapter, we provide a chronological evolution of this technique, by commenting the contents of the most relevant work published in the past ten years).
In this chapter, we investigate the possibility of extending the well-established working principles of the H-SNOM to two additional capabilities. The first consists in a *beam-labeling* technique. Beams with different optical properties are simultaneously shone on the sample, and their contribution to the optical signal is discriminated by means of the heterodyne detection. In fact, the interaction of light with sub-wavelength structured materials is influenced by many factors. One of these is the polarization state of the optical field. It has been theoretically [4, 5] and experimentally [6] demonstrated that the imaging properties of a scanning microscope are strongly influenced by the polarization state of the optical field. A beam-labeling technique would allow to illuminate the sample with different polarization states and to determine the relative optical responses simultaneously. In this case, the polarization response is determined without any influence of possible temporal changes in the experimental conditions and without any handing of additional optical elements. In the next sections, we describe the optical arrangement for the application of the beam-labeling technique to the H-SNOM.
The second capability we want to develop is the sensitivity of the instrument to the polarization state of the probed field. In modern Optics, there are some notions, like polarization and coherence, whose definitions, properties and correlations are still controversial [7]. In particular, the definition of a polarization state demands the optical properties of a light wave to be defined

over at least one spatial period. It has been pointed out by Nye in 1990, that in the case of a non-paraxial field configuration, this canonical definition can no longer be applied and the polarization state assumes rather local properties [8]. In this sense, the unique capability of a scanning probe to detect local properties of the optical field opens interesting perspectives. The possibility of making a H-SNOM sensitive to the polarization state of the probed field runs through two steps. First, one has to determine the polarization state of the light at the detector plane. Second, the polarization transfer properties of the whole collecting system have to be determined.
In this first chapter, we analyze the problematic related to the first point, whereas the polarization transfer properties of the whole system will be analyzed in chapter 2.

1.2 Heterodyne scanning near-field optical microscope

The basic set-up for an optical heterodyne detection consists of two electromagnetic waves, generated from a single coherent source, and a square-law detector device [9]. The first wave is called the *object beam* and transports the information on the amplitude and phase of the field under investigation. The second wave is called the *reference beam* and its phase and amplitude are kept constant during the experiment. The angular frequency of the reference beam undergoes a slight shift $\Delta\omega$ by passing through an acousto-optic device. The two beams are then superposed in the square-law detector. The detected signal will be proportional to the modulus square of the total field. If $E\exp(\omega t - \varphi_E)$ and $R\exp[(\omega + \Delta\omega)t - \varphi_R)$ are the expressions for the object and the reference beam respectively, the detected signal will be proportional to:

$$S(t) \propto |R|^2 + |E|^2 + 2|R||E|m\cos[\Delta\omega t - (\varphi_E - \varphi_R)]. \tag{1.1}$$

In Eq. (1.1), E and R are the amplitudes of the object and reference beam respectively, whereas φ_E and φ_R are the corresponding optical phases. We observe that Eq. (1.1) is composed of a DC term, due to the intensity of the reference and the object field, and an interference AC term which is time modulated at the shifted angular frequency $\Delta\omega$ (usually called the *beat frequency*). The beat frequency is generally of the order of tens of kHz so that the ac signal can be coherently detected by means of ordinary lock-in amplifiers. As the amplitude of the reference field is constant during the experiment, the measurement of the amplitude of the AC term is directly proportional to the amplitude of the object field. The phase of the reference field is also kept constant in the experiment in such a way that the cosine in Eq. (1.1) is modulated by variations of the phase of the object field. In this way, both amplitude and phase of the object beam are simultaneously determined.
The factor $m(0{\leq}m{\leq}1)$ is called the *relative interference amplitude*. This factor influences the quality of the interference and depends on the experimental conditions. In experiments in which the coherence length of the leaser source is much longer than the difference of the beam optical paths, and both beams are shined on the whole active surface of the detector, the interference quality is influenced only by the polarization state of the interfering beams. For instance, if $\vec{E}$ and $\vec{R}$ are linearly polarized field, then the factor m will assume the form $m = \cos\alpha$ where α is the angle between the field vectors at the plane of the detector. We will discuss in detail the implications of this term on the heterodyne detection in chapter 2. Our current goal is to show how this detection technique can be integrated into a SNOM.

SNOM is a modern well-established imaging technique widely used in nanotechnology, surface and material physics, biology and other fields [10]. The method consists in scanning a

subwavelength-size light source (or collector) very close to the investigated sample surface. This technique enables to detect optical signals with a spatial resolution much higher than the Abbe diffraction limit of the conventional far-field microscopy [13]. When the probe is used like a subwavelength source, SNOM is operated in *illumination* mode. On the contrary, when light is shined externally and collected by the probe, the microscope is operated in *collection* mode [11, 12]. This last configuration is very well suited for investigation with a heterodyne detection system. The light collected into the probe is generally propagated across a fiber. Therefore, a basic schematic of a heterodyne scanning probe optical microscope is depicted in Fig. 1.1.

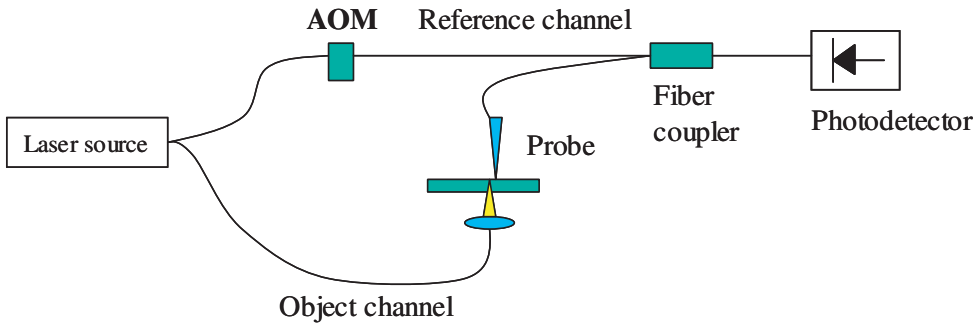

Figure 1.1: *Schematic of a fibered heterodyne scanning near field optical microscope operating in collection mode.*

The optical arrangement in Fig.1.1 recalls the one of a Mach-Zehnder interferometer. The laser beam is split in two arms and then injected in two fibered channels. An acoustooptic modulator (AOM) provides the frequency shift in the reference channel. Light collected in the fiber probe recombines with the reference beam by means of a fiber coupler and, then, reaches the photodetector. The choice of the detector depends, in general, on the wavelength and the characteristics of the laser source and on the noise level which is expected in the detection process [14]. In the next section, we will report more in details some data concerning the signal to noise ratio (SNR) achievable with such a kind of configuration.
In the past few years, H-SNOM's have been widely used in order to detect amplitude and phase of the probed field with sub-wavelength resolution. The idea of implementing a scanning probe microscope on a Mach-Zehnder interferometer was first proposed by Vaez-Iravani *et al.* [15] in 1993. In this work it was pointed out the potentiality of a pseudoheterodyne detection to enhancing the contrast in amplitude and phase images. The same kind of set-up was used later by Phillips *et al.* [16] in order to measure phase variations in the LP_{11} mode in an multi-mode optical fiber. In this paper were reported first considerations on the accuracy with which a phase profile can be detected. Recently, the interferometric technique has been improved and extended to even more interesting investigations. Detection of simultaneous amplitude and phase is particularly useful in the study of modes propagation in optical waveguides. First remarkable results, in this sense, have been reported by Balistreri *et al.* [17, 18], who demonstrated the interference of different propagating modes by detecting phase singularities across the investigated waveguide corresponding two loci where the modes interfered destructively. These two works also opened the perspective of using a H-SNOM in order to reveal, with high spatial resolution, phase singularities. Remarkable results, in this sense, have been obtained by Nesci *et al.* [19], who reported the detection of phase singularities produced by the superposition of diffraction orders in the near field of a microfabricated grating. In particular, it has been pointed out the importance of

careful consideration of the detection process in phase imaging with SNOM. It was established for the first time the crucial role of the vectorial coupling properties of the scanning probe in the interpretation of amplitude and phase images. Part of this thesis work has been, therefore, devoted to the study of such properties.

1.3 Signal to noise ratio in heterodyne detection

In the previous section, we have pointed out that heterodyne detection can be applied in those lightwave systems in which both amplitude and phase of the optical field need to be detected. The second advantage in employing this technique is that the signal power is amplified by a factor corresponding to the reference power. Moreover, compared to direct detection of the optical signal, the coherent detection provides a better signal to noise ratio (SNR). This property is particularly advantageous in scanning probe microscopy operated in collection mode. In fact, in a scanning probe imaging process, we deal with very weak signals, being the object light transferred to the detector after coupling to the nanometric probe, whose transmission efficiency is of the order of per thousand.
In order to estimate the SNR of the heterodyne detection, we start by retaking the expression in Eq. (1.1). The optical power, P, is proportional to the intensity of the optical field, so the received power at the photodetector is $P = k|E + R|^2$ where k is a constant of proportionality. The expression for the photocurrent generated in the detector takes the form:

$$I(t) = \xi(P_R + P_E) + 2\xi\sqrt{P_R P_E}\cos[\Delta\omega t - (\varphi_E - \varphi_R)] \quad , \tag{1.2}$$

where $P_R = k|R|^2$, $P_E = k|E|^2$ and we assume $m = 1$. Parameter ξ is called the detector *responsivity*. It is defined as

$$\xi = \frac{\eta q}{h\nu} \quad , \tag{1.3}$$

where $h\nu$ is the energy transported by a single photon, q is the electron charge, η is the *quantum efficiency* defined as $\eta = N_e/N_p$, where N_e is the electron-generation rate and N_p is the photon-incidence rate [20]. If the optical power P_{im} impinges on the detector surface, then the induced photocurrent will be $I = \xi P_{im}$.
The photodetector response fluctuates because of two main sources of noise. The first is called the Johnson noise or *thermal-noise* and its average signal power is expressed

$$\sigma_T^2 = (4k_B T/R_L)\Delta f \quad , \tag{1.4}$$

where $k_B T$ is the thermal energy at absolute temperature T, R_L is the circuit load resistance [20], Δf is the detector bandwidth.

The second noise source is called the *shot-noise* and its average signal power has the form

$$\sigma_s^2 = 2q(I + I_d)\Delta f \quad , \tag{1.5}$$

where I is the induced photocurrent of Eq. (1.2) and I_d is the dark current.
The total average noise-signal power, will be the sum of both contributions

$$\sigma^2 = \sigma_T^2 + \sigma_s^2 \quad . \tag{1.6}$$

We observe that while the thermal-noise is independent from the induced photocurrent, I, the shot-noise is proportional to it. We will see that this peculiarity allows to make the SNR of the

heterodyne signal only shot-noise limited.
The SNR is obtained by dividing the avarege signal power by the average noise power. Because it is in general $P_R \gg P_E$, the induced photocurrent can be approximated by the dominant term ξP_R. So, in this case, SNR is written as

$$SNR = \frac{\langle I_{ac}^2 \rangle}{\sigma^2} = \frac{2\xi^2 \bar{P_E} P_R}{2q(\xi P_R + I_d)\Delta f + \sigma_T^2} \quad . \tag{1.7}$$

where $\bar{P_E}$ is the average signal power. From Eq. (1.7) one can see the main advantage of the coherent detection. Actually, as the reference power, P_R, at the detector, can be controlled at will, it can be made large enough to make the detector noise dominated by the shot-noise. In practice, we have $\sigma_s^2 \gg \sigma_T^2$ when $P_R \gg \sigma_T^2/(2q\xi\Delta f)$. Under the same condition the dark current contribution to the shot-noise becomes negligible ($I_d \ll \xi P_R$). By applying all this conditions to Eq. (1.7), we find that the SNR in the shot-noise limit is given by

$$SNR = \frac{\xi \bar{P_E}}{q\Delta f} \quad . \tag{1.8}$$

We can alternatively express the SNR in terms of average number of photons N_p striking the detector surface during the integration time $\tau = 1/(2\Delta f)$. The signal power is related to N_p BY $\bar{P_E} = N_p h\nu 2\Delta f$. By substituting into Eq. (1.8), we finally have

$$SNR = 2\eta N_p \quad . \tag{1.9}$$

In Eq. (1.9), a factor 2 appears, if compared to direct detection, which is known as *heterodyne gain*. This final expression also stresses the fact that the SNR is strictly related to the detector quantum efficiency. In a photomultiplier (PM), for instance, η_{PM} is typically 10%, while in a photodiode (PD) we have a typical η_{PD} of 70%. A photodiode is a *p-i-n* semiconductor device whose performance is prevalently affected by thermal-noise [20,21]. However, as discussed above, the heterodyne detection allows to achieve the shot-noise limit also in this kind of device. By the moment that a photodiode is also characterized by a superior quantum efficiency, it becomes the best choice to adopt in the interferometric scanning probe set-up.
The SNR is also related to the accuracy with which amplitude and phase can be measured. From Eq. (1.7) we find that the SNR is proportional to $|E| = \sqrt{\bar{P_E}}$, then the standard deviation of the amplitude is found to be

$$\frac{\delta E}{|E|} = \frac{1}{\sqrt{SNR}} \quad . \tag{1.10}$$

The accuracy of the phase measurement is instead given by [22]

$$\delta\varphi = \frac{1}{\sqrt{SNR}} \quad . \tag{1.11}$$

Formulae reported in this section will be used in chapter 2 to evaluate the performances of our detection system.

1.4 Multiple-heterodyne scanning probe microscope

We have seen in the previous sections that a H-SNOM presents two main advantages which are particularly desirable in scanning probe measurements. The first is provided by the fact that such a set-up enables simultaneous measurements of amplitude and phase of the probed field.

The second is represented by the fact that this detection technique can be only shot-noise limited. This means that, in principle, heterodyne detection can achieve precision in determining wave properties that is limited only by the basic uncertainty principle of quantum mechanics [21]. This advantage is particularly evident in collection scanning probe microscopy where the transmission efficiency of commercially available probe ranges between 10^{-3}, for uncoated tapered fibers, and 10^{-4} for metal-coated aperture probes.
In this section, we introduce the optical set-up for a novel apparatus which combines the characteristics mentioned above with two new capabilities. The first consists in enabling simultaneous illumination from different beams, and being able to discriminate their optical signals (*beam labeling*). The second is represented by the fact that the instrument set-up is sensitive to the polarization state of the detected field. As these properties rise from the fact that several heterodyne signals are produced in the set-up, we have named this instrument Multiple-Heterodyne Scanning Probe Optical Microscope (MH-SPOM).

1.4.1 Optical set-up for multiple-beam generation

The optical arrangement for the multiple-beam generation is displayed in Fig.1.2. The laser source is a 150mW single mode (TEM00) frequency-doubled Nd:YAG diode-pumped solid state laser (λ=532)(*Coherent Inc., Model COLCOMPASS 315M-150*). The laser beam is initially split in two by the beam splitter (BS). Light in the two beams is distributed in such a way that about 96% of the power is sent into the object channel, while the remaining is sent into the reference channel. As the object channel is composed by the beams which will illuminate the samples and which will be collected by probe, as much power as possible has to be concentrated in these beams. From this point ahead, both arms of the interferometer are similarly built up. Each beam passes through a $\lambda/4$ plate in order to turn the polarization from linear to circular. A polarizing beam splitter (PBS), separates the two field components parallel and orthogonal to the optical bench respectively. Each polarization goes through an acousto-optic modulator frequency shifters (AOM) (*IntraAction Corp.*, model AOM-40 series) in order to undergo the right frequency shift for the heterodyne detection. The AOM devices are provided with the required radio frequency (RF) drive signal by means of two frequency generators (*IntraAction Corp.*, Dual Channel Frequency Synthesizer, model DFE-404A4). Both generators provide two synthesized RF signals. The first is fixed, while the second can be varied with a resolution of 10kHz. In the course of our experiments, $\mathrm{AOM}_{\omega 1}$, $\mathrm{AOM}_{\omega 2}$, $\mathrm{AOM}_{\omega 3}$ and $\mathrm{AOM}_{\omega 4}$ were excited at 40.00, 40.02, 40.05 and 40.09 MHz respectively. Subsequently, each beam is sent through a Glan-Taylor polarizer to assure a clean linear polarization. A shutter is placed at the exit of each polarizer in order to select the required diffraction order. At the end of this path, in both the reference and the object channel, we obtain two frequency shifted orthogonally polarized beams. Each pair of beams is finally superposed by means of a PBS. The double-reference beam is injected into a single mode fiber, while the superposed object beams propagate in free-space and are available for illuminating the investigated sample.

1.4.2 Signal analysis

The system has been tested by means of the simple configuration displayed in Fig. 1.3. The light coupled into the probe and the light from the reference fiber are superposed in a fiber coupler before reaching the detector. As both reference and object channels transport two beams shifted in frequency by different values, in the detector we have the generation of several beat-signals. The frequency shifts induced by the acousto-optic modulations together with all the beat-signals due to the their relative combinations are listed in Fig.1.4. During the experiment, it is very

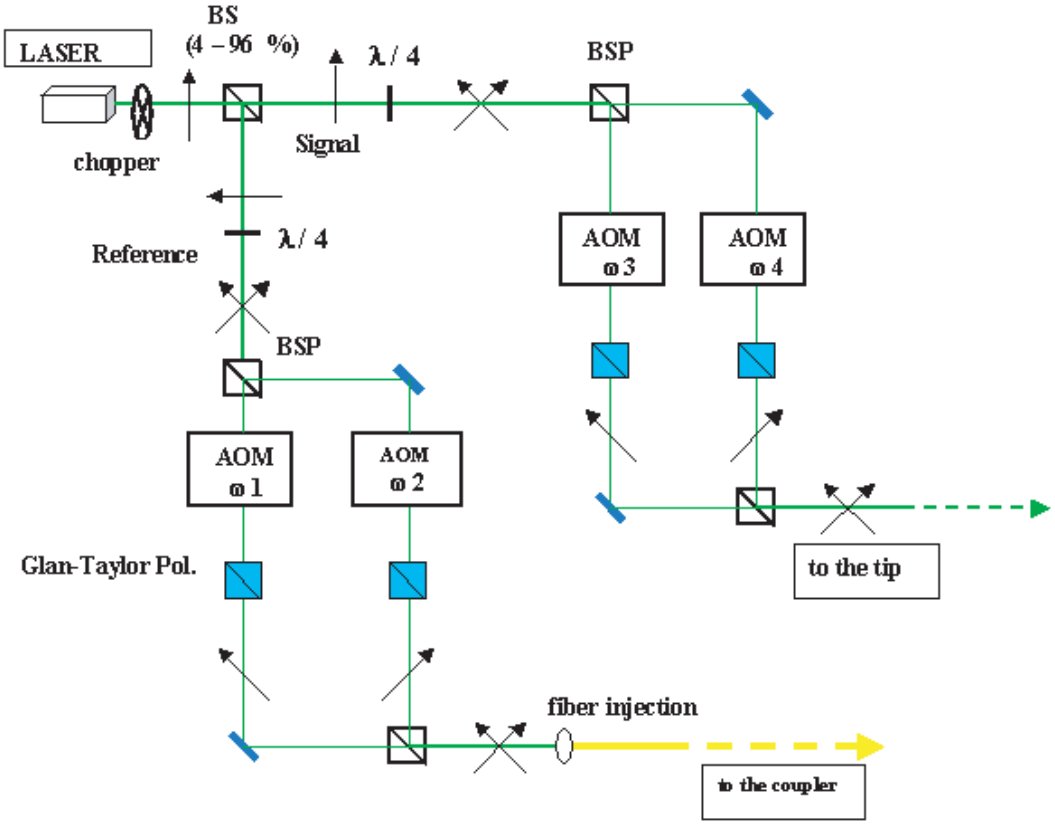

Figure 1.2: *Schematic of the optical set-up for the beam generations of the MH-SPOM.*

useful to monitor the actual generation and the quality of the beat-signals. We monitored them

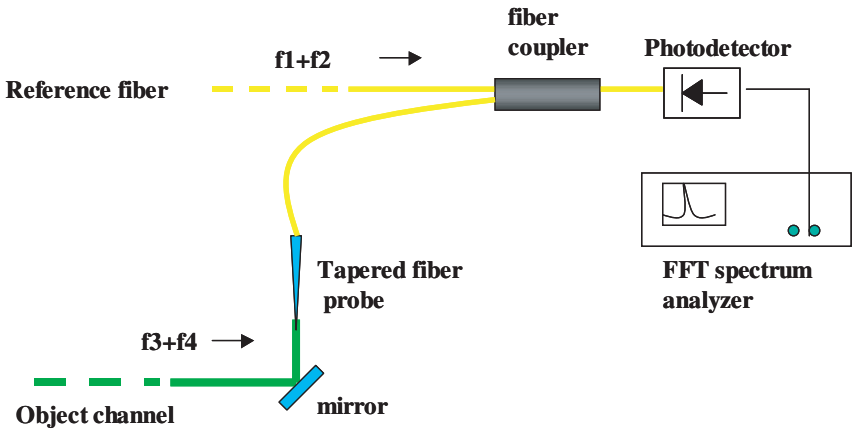

Figure 1.3: *Set-up for the monitoring of the multiple-heterodyne signals.*

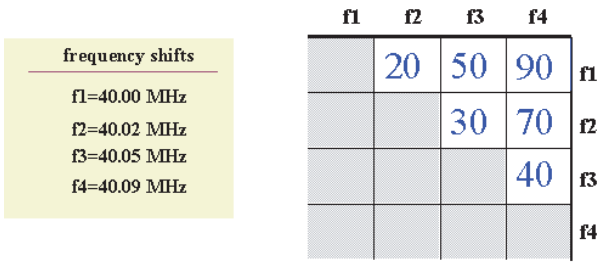

Figure 1.4: *a)List of the frequency shifts induced on the four beams by the acoust-optic modulation.b) Possible combinations of the electronic beat-signals generated in the photodetector by the superposition of the four beams.*

by means of a FFT spectrum analyzer (*Stanford Research System, Model SR770 FFT Network Analyzer*) with an input impedance R_{in}=1$M\Omega$ and working frequency range from 0 to 100kHz. Since the spectrum analyzer measures signals which have a frequency modulation, the detected signals correspond to the term of interference in Eq. (1.1) for each pair of interfering beams. The following equations represent the expressions for the modulated part of all the heterodyne signals:

$$S_{r1,r2}(t) \propto 2\sqrt{I_{r1}I_{r2}}\cos[(\omega_1-\omega_2)t-(\varphi_{r1}-\varphi_{r2})], \tag{1.12}$$
$$S_{r1,o1}(t) \propto 2\sqrt{I_{r1}I_{o1}}\cos[(\omega_1-\omega_3)t-(\varphi_{r1}-\varphi_{o1})], \tag{1.13}$$
$$S_{r1,o2}(t) \propto 2\sqrt{I_{r1}I_{o2}}\cos[(\omega_1-\omega_4)t-(\varphi_{r1}-\varphi_{o2})], \tag{1.14}$$
$$S_{r2,o1}(t) \propto 2\sqrt{I_{r2}I_{o1}}\cos[(\omega_2-\omega_3)t-(\varphi_{r2}-\varphi_{o1})], \tag{1.15}$$
$$S_{r2,o2}(t) \propto 2\sqrt{I_{r2}I_{o2}}\cos[(\omega_2-\omega_4)t-(\varphi_{r2}-\varphi_{o2})], \tag{1.16}$$
$$S_{o1,o2}(t) \propto 2\sqrt{I_{o1}I_{o2}}\cos[(\omega_3-\omega_4)t-(\varphi_{o1}-\varphi_{o2})]. \tag{1.17}$$

In equations (1.12)- (1.17), I_{ri} and I_{oi} *(i=1,2)* represent the intensity of the two reference beams and the intensity of the two object beams respectively at the photodetector surface. Similarly, φ_{ri} and φ_{oi} *(i=1,2)* represent the relative optical phases. We indicate the angular frequencies as they are associated to the AOMs modulators in Fig.1.2 and to the frequency shifts in Fig.1.4 so that $\omega_j = 2\pi\Delta f_j$ *(j=1..4)*. As a result, the superposition of the four beams generates six beat-signals. In Fig.1.5 we report the signal detected at the spectrum analyzer. In order to remove the noise, the measurement has been taken in averaged mode over 100 measurements. We can

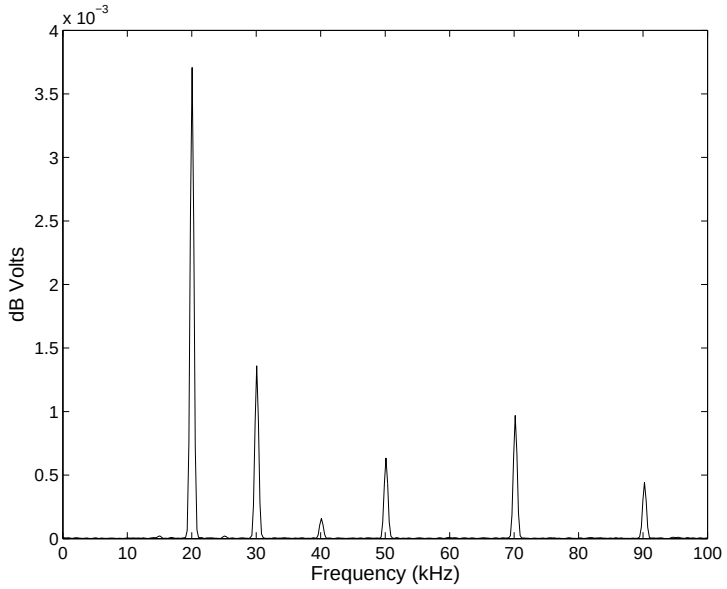

Figure 1.5: *Signals detected at the spectrum analyzer when both object beams are coupled into the probe and both reference beams are superposed in the fiber coupler. The signal is recorded by averaging over 100 measurements in order to remove the noise level.*

actually observe six signals each corresponding to the expected beat-frequency. The signal at 20kHz is due to the interference of the two reference beams. It is the highest measured signal because these beams are directly transferred to the detector through the reference fiber. Signals at 30, 50, 70 and 90kHz are weaker and they are due to the interference of the reference beams with the object beams. Actually, the object beams are transferred to the detector through the probe whose transmission factor is $\sim 10^{-3}$. Nevertheless, their amplitude is amplified in the heterodyne signal. The reason why we observe these interference signals, in spite of the orthogonality of the involved polarizations, is a consequence of the propagation in the fiber. In fact, a linear polarization will be in general turned into an elliptical one because of the birefringence induced in the fiber by torsion and wrapping . These five signals represent the information we mainly exploited in our experiments. In the measurement in Fig.1.5 it is also observable a small signal at 40kHz, which corresponds to the interference of the two object beams. Measurements in Fig.1.5 demonstrate the first additional characteristic of the MH-SNOM set-up. Actually, even though the two object beams are completely superposed one to each other and they are simultaneously coupled to the probe, their contributions to the detector signal is discriminated by their different beat signals. Therefore, information on amplitude and phase for object beam 1 can be extracted by signals at 30 and 50 kHz, while the same information for object beam 2 can be extracted by signals at 70 and 90 kHz. This procedure enables the

labeling of the different beams employed in the experiments. This property is particularly useful when one wishes to investigate the optical response of a given structure to different polarizations of light in the same experimental conditions. The reader may argue that the double-labeling procedure described above is redundant, and that one could use a single reference beam to discriminate the contribution of the two object beams. However, we will see in the next chapter the utility of providing the instrument with a second reference beam.

1.5 MH-SPOM polarization transfer properties

An electromagnetic wave is characterized by amplitude, phase and a polarization state. The state of polarization is completely determined if, at each position along the path of propagation, the electric field (light vector) is known. As the wave covers the distance of one wavelength, the light vector can describe in space either a line, or a circle or an ellipse. We will say, then, that the wave is linearly, circularly and, more in general, elliptically polarized. The geometric figure swept by the light vector is called the light ellipse. In this section, we will introduce the main parameters which characterize the light ellipse together with some notions of the Jones formalism which provides the mathematical representation of the light vector. These notions will be used to discuss the polarization transfer properties of the MH-SPOM. Actually, as already mentioned in section 1.4.2, the MH-SPOM is provided with a reference and an object channel in order to enable heterodyne detection of the optical signals. Reference and object beams are initially linearly polarized. However, as they propagate to the detector, their polarization state is arbitrarily modified by the birefringence in the reference and object fiber respectively. Therefore, the beams reach the detector surface with an arbitrary state of polarization. We are interested in setting up a system which enables the determination of this state of polarization. In the case of the reference channel, the polarization state can be determined with a general method which will be exposed later on in this section. This method could in principle be applied also to the object channel. However, the extremely weak signals transmitted by the probe make its application more complicated. We will demonstrate that the use of the heterodyne signal can overcome this experimental limitations.

1.5.1 Light ellipse parameters and Jones formalism

The most general polarization state is the elliptical polarization. In a Cartesian coordinate system ($\widehat{x}$ - $\widehat{y}$) the ellipse can be characterized by three independent parameters which can be either the components A_x and A_y of the light vector and their phase difference $\delta = \delta_y - \delta_x$, or the lengths of the major and minor semi-axes **a** and **b** and the angle Ψ of inclination of

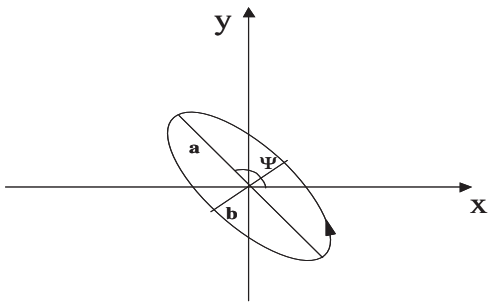

Figure 1.6: *Parameters defining the state of polarization of an optical field in the plane x-y.*

the major axis with respect to the $\widehat{x}$ axis (see Fig.1.6). The light ellipse is fully characterized when the direction of rotation of the light vector is defined. Such orientation is determined by the value of the phase difference δ. A right-handed elliptical polarization corresponds to a δ value in the interval $0^o < \delta < 180^o$, while a left-handed polarization corresponds to the range $180^o < \delta < 360^o$.
The expression that relates the light ellipse parameters has the form [23]:

$$\tan 2\Psi = \frac{2A_xA_y}{A_x^2 - A_y^2}\cos\delta. \tag{1.18}$$

An alternative formula is obtained by introducing the angle γ, such that $\tan\gamma = A_y/A_x$, from which 1.18 can be written as:

$$\tan 2\Psi = \tan 2\gamma \cos\delta. \tag{1.19}$$

Another important parameter for the definition of the polarization state is the *ellipticity* which is defined as the ratio $(\mathbf{b}/\mathbf{a})$. By introducing the angle ω, such that $\pm\mathbf{b}/\mathbf{a} = \tan\omega$ $(-45^o \leq \omega \leq 45^o)$, this parameter can be expressed like a function of γ and δ as follows:

$$\sin 2\omega = \sin 2\gamma \sin\delta. \tag{1.20}$$

When a light wave passes through a series of optical elements, its polarization state can be, in general, modified. In order to determine the transformed polarization state, the new parameters have to be found. As one is interested only in the shape transformation of the light ellipse, the quantity to be measured is the ratio between the two components A_x and A_y. In this way, the intensity can be expressed in the normalized form $A_x^2 + A_y^2 = 1$, and the polarization state is univocally determined by the two angles Ψ and ω in the Poincaré sphere representation [23].
Mathematically, the polarization state can be described by means of a two-element complex column vector, a , called the Jones vector, which has the form:

$$a = \begin{bmatrix} A_xe^{i\delta_x} \\ A_ye^{i\delta_y} \end{bmatrix} = e^{\delta_x}\begin{bmatrix} A_x \\ A_ye^{i\delta} \end{bmatrix} \quad \delta = \delta_y - \delta_x, \tag{1.21}$$

where A_x and A_y are the a components in an orthogonal coordinate system, δ_x and δ_y are the respective phases and δ_x is the their difference. If the elements of this vector are known, it is possible to determine through Eqs. (1.18),(1.19) and (1.20) the light ellipse parameters. Conventional optical elements are characterized by a complex 2×2 matrix J, called the Jones matrix, which allows to calculate the transformation of the polarization state of an optical beam as it passes through the element. In mathematical terms, the transformed vector is obtained by applying the operator J to the initial vector a.

1.5.2 Reference beam polarization state at the detector plane

As a first step, we want to determine the state of polarization of one of the reference beams of the MH-SPM set-up at the detector surface. For this purpose, we use the optical arrangement displayed in Fig.1.7. No light is coupled into probe so that only reference beams reach the fiber coupler. We first define a coordinate system ($\widehat{x}_d$ - $\widehat{y}_d$) at the detector plane in which the Jones vector of the reference beam will be written as:

$$A_{rd} = \begin{bmatrix} a_{rx} \\ a_{ry} \end{bmatrix} = \begin{bmatrix} A_{rxd} \\ A_{ryd}e^{i\delta_r} \end{bmatrix} \quad \delta_r = \delta_{rx} - \delta_{ry} \tag{1.22}$$

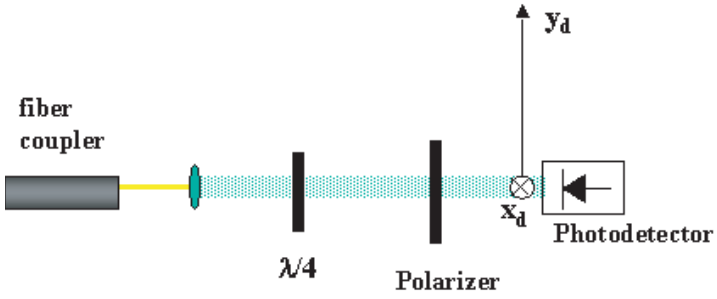

Figure 1.7: *Optical arrangement for the determination of the Jones vector of the reference beam at the detector plane.*

A quarter wave plate ($\lambda/4$) and a polarizer are placed in sequence in front of the exit of the fiber coupler. The Jones matrix for an ideal (non absorbing) polarizer, P, and for the $\lambda/4$, L, in the detector coordinate system are respectively:

$$P = \begin{bmatrix} \cos\theta^2 & sin\theta cos\theta \\ \sin\theta cos\theta & sin\theta^2 \end{bmatrix}, \tag{1.23}$$

and

$$L = \begin{bmatrix} i\cos\theta^2 + sin\theta^2 & (i-1)sin\theta cos\theta \\ (i-1)sin\theta cos\theta & i\sin\theta^c os\theta^2 \end{bmatrix}, \tag{1.24}$$

where θ is the angle formed by the axes of polarizer and $\lambda/4$ with axis x_d.
The procedure to determine the light ellipse parameters consists in performing four intensity measurements for different orientations of the optical elements. The sequence of measurements is like follows:
I) *Single polarizer with its axis parallel to* x_d ($\theta = 0^o$).

In this case, the transformed vector is given by

$$A'_{rd} = P(0)A_{rd} = \begin{bmatrix} 1 & 0 \\ 0 & 0 \end{bmatrix} \begin{bmatrix} a_{rx} \\ a_{ry} \end{bmatrix} = \begin{bmatrix} a_{rx} \\ 0 \end{bmatrix}. \tag{1.25}$$

The field intensity I_1 is given by

$$I_1 = A'_{rd}A'^{*}_{rd} = \begin{bmatrix} a_x & 0 \end{bmatrix} \begin{bmatrix} a_{rx} \\ 0 \end{bmatrix} = A^2_{rx}. \tag{1.26}$$

II) *Single polarizer with its axis parallel to* y_d ($\theta = \pi/2$).

In this case,

$$A'_{rd} = P(\pi/2)A_{rd} = \begin{bmatrix} 0 & 0 \\ 0 & 1 \end{bmatrix} \begin{bmatrix} a_{rx} \\ a_{ry} \end{bmatrix} = \begin{bmatrix} 0 \\ a_{ry} \end{bmatrix}. \tag{1.27}$$

The intensity I_2 will be

$$I_2 = [\ 0 \quad a_{ry}\ ] \begin{bmatrix} 0 \\ a_{ry} \end{bmatrix} = A_{ry}^2. \tag{1.28}$$

III) *Single polarizer with the axis at* 45^o *with respect to* x_d ($\theta = \pi/4$).

We can write:

$$A'_{rd} = P(\pi/4)A_{rd} = \frac{1}{2}\begin{bmatrix} 1 & 1 \\ 1 & 1 \end{bmatrix}\begin{bmatrix} a_{rx} \\ a_{ry} \end{bmatrix} = \frac{1}{2}\begin{bmatrix} a_{rx} + a_{ry} \\ a_{rx} + a_{ry} \end{bmatrix}. \tag{1.29}$$

By explicitly writing the complex vectorial components, intensity I_3 will have the form:

$$\begin{aligned} I_3 &= \frac{1}{4}[\ A_{rx} + A_{ry}e^{\delta} \quad A_{rx} + A_{ry}e^{\delta}\ ] \begin{bmatrix} A_{rx} + A_{ry}e^{-\delta} \\ A_{rx} + A_{ry}e^{-\delta} \end{bmatrix} \\ &= \frac{1}{2}(A_{rx}^2 + A_{ry}^2 + 2A_{rx}A_{ry}\cos\delta). \end{aligned} \tag{1.30}$$

IV) $\lambda/4$ *followed by the polarizer with both the respective axes at* 45^o *with respect to* x_d ($\theta = \pi/4$).

By substituting $\theta = \pi/4$ in 1.23 and 1.24, we obtain for the transformed vector:

$$A'_{rd} = P(\pi/4)L(\pi/4)A_{rd} = \frac{1}{2}\begin{bmatrix} 1 & 1 \\ 1 & 1 \end{bmatrix}\begin{bmatrix} i & 0 \\ 0 & 1 \end{bmatrix}\begin{bmatrix} a_{rx} \\ a_{ry} \end{bmatrix} = \frac{1}{2}\begin{bmatrix} ia_{rx} + a_{ry} \\ ia_{rx} + a_{ry} \end{bmatrix}. \tag{1.31}$$

Finally, we find for intensity I_4

$$\begin{aligned} I_4 &= \frac{1}{4}[\ iA_{rx} + A_{ry}e^{\delta} \quad iA_{rx} + A_{ry}e^{\delta}\ ] \begin{bmatrix} -iA_{rx} + A_{ry}e^{-\delta} \\ -iA_{rx} + A_{ry}e^{-\delta} \end{bmatrix} \\ &= \frac{1}{2}(A_{rx}^2 + A_{ry}^2 + 2A_{rx}A_{ry}\sin\delta). \end{aligned} \tag{1.32}$$

From the expressions for intensities I_1 and I_2, one gets components A_{rx} and A_{ry} of the light vector, whereas from intensities I_3 and I_4 one determines the value of δ. The procedure exposed above can be applied to determine the polarization state of the second reference beam.

1.5.3 Object beam polarization state at the detector plane

The object channel is the part of the MH-SPOM which is composed by the scanning probe and the object fiber. Even though, nowadays, the guiding properties of an optical fiber are well documented in literature [24], the vectorial properties of a scanning probe have been very little investigated. This is not surprising given the difficulty of modeling and interpreting the interaction processes of an electromagnetic wave with the probe structure, which has in general nanometric fabrication features [25]. It is not a misconception, then, to assume a priori that the probe and the fiber can modify the polarization state of the probed light by two different mechanisms which result in the final state of polarization observed at the detector surface. In this section we will show how to determine the resulting polarization state at the exit of the fiber coupler by exploiting the heterodyne signals. A more detailed investigation about the vectorial properties of the system *probe+fiber* will be presented in the next chapter.

In the previous section, we have seen that the polarization state of the reference beams at the detector surface can be determined by a sequence of four intensity measurements. When an object beam is superposed to the reference beam in the fiber coupler, the general situation at the detector plane will be as depicted in Fig.1.8. Both beams reach the detector surface with an arbitrary polarization and their superposition gives rise to the relative heterodyne signal. For the description of the measurement procedure we choose the reference beam modulated at the angular frequency ω_1 and the object beam modulated at the angular frequency ω_3. The heterodyne signal corresponds in this case to Eq. (1.13).

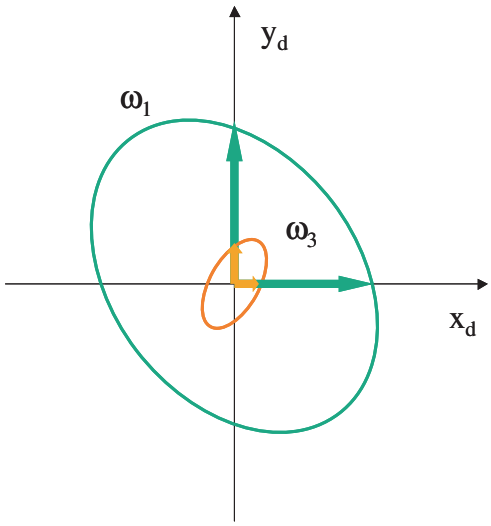

Figure 1.8: *Both reference and object signals reach the detector surface with an arbitrary polarization state. The single components interfere producing heterodyne signals on each axis.*

The optical arrangement is similar to the one displayed in Fig.1.7 without the $\lambda/4$, which is removed. Firstly, we orientate the polarizer axis parallel to axis x_d, in such a way that the field components along y_d are filtered and cannot contribute to the signal. The resulting heterodyne signal, S_x, is given by

$$S_x(t) \propto 2\sqrt{I_{r1x}I_{o1x}}\cos[(\omega_1-\omega_3)t+(\varphi_{r1x}-\varphi_{o1x})], \tag{1.33}$$

where $\sqrt{I_{r1x}} = A_{r1x}$ and $\sqrt{I_{o1x}} = A_{o1x}$ are the $\widehat{x}_d$ light vector components of reference and object beam respectively. We will indicate with $A_x = 2A_{r1x}A_{o1x}$ the amplitude of S_x and with $\Phi_x = \varphi_{r1x} - \varphi_{o1x}$ its phase.
Secondly, we rotate the polarizer axis of 90° and we detect the heterodyne signal S_y as

$$S_y(t) \propto 2\sqrt{I_{r1y}I_{o1y}}\cos[(\omega_1-\omega_3)t+(\varphi_{r1y}-\varphi_{o1y})], \tag{1.34}$$

where $\sqrt{I_{r1y}} = A_{r1y}$ and $\sqrt{I_{o1y}} = A_{o1y}$ are in this case the y_d light vector components along axis. We will indicate, in this case, the amplitude and the phase of S_y as $A_y = 2A_{r1y}A_{o1y}$ and $\Phi_y = \varphi_{r1y} - \varphi_{o1y}$ respectively.
We have seen in section 1.5.1, that the light ellipse is determined once the ratio of the light vector components and their phase difference are known. We can obtain this information by exploiting both amplitudes and phases of S_x and S_y. The ratio of the components is obtained by taking the ratio of the heterodyne signal amplitudes as follows:

$$\frac{A_y}{A_x} = \frac{2A_{r1y}A_{o1y}}{2A_{r1x}A_{o1x}} \quad \Longrightarrow \frac{A_{o1y}}{A_{o1x}} = \frac{A_y}{A_x}\frac{A_{r1x}}{A_{r1y}}. \tag{1.35}$$

The components of the reference beam have previously been determined from the four-step measurement discussed in section 1.5.2, therefore, all the values in the second hand of Eq. (1.35) are known and the ratio A_{o1y}/A_{o1x} can be easily calculated.
On the other hand, the phase difference is obtained by subtracting phases Φ_y and Φ_x as follows:

$$\begin{aligned} \Phi_y - \Phi_x = (\varphi_{r1y} - \varphi_{o1y}) - (\varphi_{r1x} - \varphi_{o1x}) \Longrightarrow \\ (\varphi_{o1y} - \varphi_{o1x}) = (\Phi_y - \Phi_x) - (\varphi_{r1y} - \varphi_{r1x}). \end{aligned} \tag{1.36}$$

Also in this case, phases in the second hand of Eq. (1.36) are obtained experimentally and the phase difference of the object light vector can be calculated as a function of them.
The procedure exposed above allows to determine the parameters of the light ellipse associated to the object beam. It presents two main advantages. The first is that the light vector components are obtained through heterodyne signals whose amplification allows to work out the weakness of the field transmitted by the probe. The second is that, once the polarization state of the reference beam is determined, the light ellipse of the object beam is obtained in only two steps and without using the quarter-wave plate.

1.6 Conclusions

In this chapter we have introduced the characteristics of the multiple-heterodyne scanning probe optical microscope (MH-SPOM). The instrument preserves all the advantages of the H-SNOM. First, it allows simultaneous detection of the amplitude and the phase of the probed field. Second, the heterodyne signals are characterized by a SNR which can be increased at will by operating on the optical power of the reference beam. In addition, the MH-SPOM is provided with tow more capabilities: beam-labeling and polarization sensitivity. The multiple-beat-signal generation, for the beam-labeling technique, has been demonstrated experimentally. The determination of the polarization state of the detected field at the detector plane has been described by introducing the notions of light ellipse, light vector and Jones vector. We have demonstrated that the polarization state of the object beam can be determined in spite of the weakness of the transmitted signal by means of the heterodyne signal. Moreover, compared to a canonical procedure, the Jones vector associated to the object beam is determined in only two steps and with the use of a single polarizer.

Chapter 2

MH-SPOM polarization transfer properties

2.1 Introduction

In the previous chapter, we have seen that the polarization state of the object beam at the detector plane, can be determined once the Jones vector of the reference beam is known. The procedure is operated in only two steps and with the use of a single polarizer. In this chapter, we will introduce a more elegant procedure which allows to obtain the light ellipse parameters by exploiting only the heterodyne signals without any additional optical element and without any previous measurement of the polarization state of the reference beam. By applying this different procedure, we will investigate the possibility of characterizing the polarization transfer properties of the MH-SPOM by means of a single Jones matrix.
In a conventional imaging system, the optical field distribution at the image plane is related to the field distribution at the object plane in a way which depends on the transfer characteristics of the interposed optical elements. The function, which relates the field distributions in the two planes, is generally called the Optical Transfer Function (OTF) of the system. In case of coherent light, the OTF relates the complex amplitudes of the image and the object field distributions, whereas, in case of incoherent light, a relationship is established between the intensity distributions. The OTF concept is strictly related to the notion of the light angular spectrum in Fourier Optics [27]. The possibility to extend this notion to the image formation in scanning near-field optical microscopy has been questioned or investigated especially in the past decade. In 1993, it was demonstrated theoretically by Van Lebeke [33] *et al.* that the signal collected in a SNOM experiment is proportional to square modulus of the electric near-field. In the same year, it was introduced the usage of an intensity transfer function (ITF), which relates the Fuorier transform (FT) of a near-field optical image to the FT of a corresponding intensity distribution [28]. The same approach was adopted in [29] to determine the spatial resolution and the coupling efficiency of a scanning probe. Assumed the proportionality between the detected signal and the intensity distribution in the near-field, there are other circumstances which complicate the interpretation of the scanned images. Actually, the near-field distribution is, in general, composed by homogeneous and evanescent waves. It means that, at each constant plane above the sample surface, the superposition of the different waves gives rise to a field profile which not necessarily reproduces the features of the investigated surface [37–39]. In order to solve the inverse problem, one has to compare the experimental data with numerical simulations of the interaction between the light and the sub-wavelength structure. This means that the

main features of the sample surface have to be known a priori. It has been shown by Carminati *et al.* [30], that, in case in which the multiple scattering between the probe and the sample can be neglected, it is possible to determine an OTF for the probe. In this work, the detected signal is assumed to be proportional to the convolution of a probe function, which accounts for the finite size of the probe, with the near-field intensity. In the Fourier space, the convolution becomes a product, and the OTF of the probe is obtained from the ratio of the signal transform to the intensity transform. Computations were performed for different features of the simulated structure and different scanning plane distances. The results were comparable in all the circumstances, showing that the calculated OTF was an actual property of the simulated probe. The relationship between the near-field intensity, above the sample surface, and the surface features has been worked out by Fornel *et al.* [40] in 1996. When this relationship is applied in the formula proposed in [30], the resulting expression is no longer in the form of a product, and the OTF cannot be calculated anymore. As a result, one can conclude that it is possible, in simplified circumstances, to determine an OTF for the probe, which relates the detected signal to the optical near-field distribution, but such a function cannot be found for relating the detected signal to the topography of the investigated surface. Therefore, as one attempts to solve the inverse problem, the spatial resolution in SNOM images is determined by the resolution with which the intensity of the near-field is detected [31, 32].
In more realistic circumstances, SNOM images are also affected by the interaction of the probe with the sample. Actually, such an interaction breaks the spatial invariance of the detection [35, 36, 71].
A more recent approach to the problem has been proposed, through a rigorous theory, by Greffet *et al.* [41]. In this theory, the angular spectrum of the optical near-field is associated to the modes propagating into the fiber, once the light has been coupled to the probe. The different spatial frequencies contribute to the excitation of a fiber mode by means of a coupling coefficient. However, it has been pointed out later, in [25], that such a theory can be realistically applied only assuming two restrictive conditions. The first is that the angular spectrum has to be narrow enough to assume such coefficients nearly constant. The second is that one has to assume the probe response, to the different components of the optical field, to be uniform. This last requirement is particularly restrictive, and in reality, the vectorial properties of scanning probes are, nowadays, still object of investigation.
In this and in the next chapter, we will introduce some experimental procedures, which involve the MH-SPOM, to investigate the vectorial response of an uncoated tapered fiber probe. The idea is to relate the known vectorial properties (polarization state) of the object field with the vectorial properties of the detected field. Such a relationship can be established if the Jones matrix of the whole collecting system is determined. In the next sections, we investigate the possibility to determine a Jones matrix for the MH-SPOM. For this purpose, we introduce a definitive polarization sensitive detection system, which avoid mechanical handling and experimental condition perturbations by exploiting only the series of multiple heterodyne signals introduced in chapter 1.

2.2 Polarization sensitive detection system

In chapter 1, we have introduced the idea to set up a detector system which would be sensitive to the polarization state of the optical beams at the detector plane. Moreover, we have introduced the four-step intensity measurement which allows to determine the light ellipse for the reference beam. Such a procedure involves two additional optical elements: a polarizer and a quarter-wave plate (QWP). We have also seen that it is possible to apply a two-steps procedure, involving a

single polarizer, which allows to determine the light ellipse of the object beam by exploiting the heterodyne signals. Even though the reported procedures can be straightforwardly applied to the current system, they present a couple of undesired aspect. Firstly, in order to measure the light ellipse parameters, one has to acquire more signals for different orientation of the polarizer and the QWP. This need is not compatible with a realistic interferometric scanning probe experiment. Actually, the phase detection can be extremely sensitive to air stream blowing and, more in general, to environmental vibrations. In order to screen the optical system from these disturbances, the whole set-up is embedded into a plexiglas box which covers the entire optical bench. During the multiple-step measurements exposed in chapter 1, the box need to be open in order to handle and rotating the optical elements. It is then unimaginable to expect the light vector properties not to be affected by the consequent produced vibrations. Secondly, the procedures demand a certain time to be completed and this means that one has to assume a high reliability of all the mechanical components. These problems may be solved by providing the optical set-up with a series of automated devices which can be, nevertheless, expensive and space demanding.

2.2.1 Electronic system

In this section, we introduce an alternative detection system arrangement which works out the inconveniences listed above. The complete detection system is displayed in Fig.2.1.The polarizer

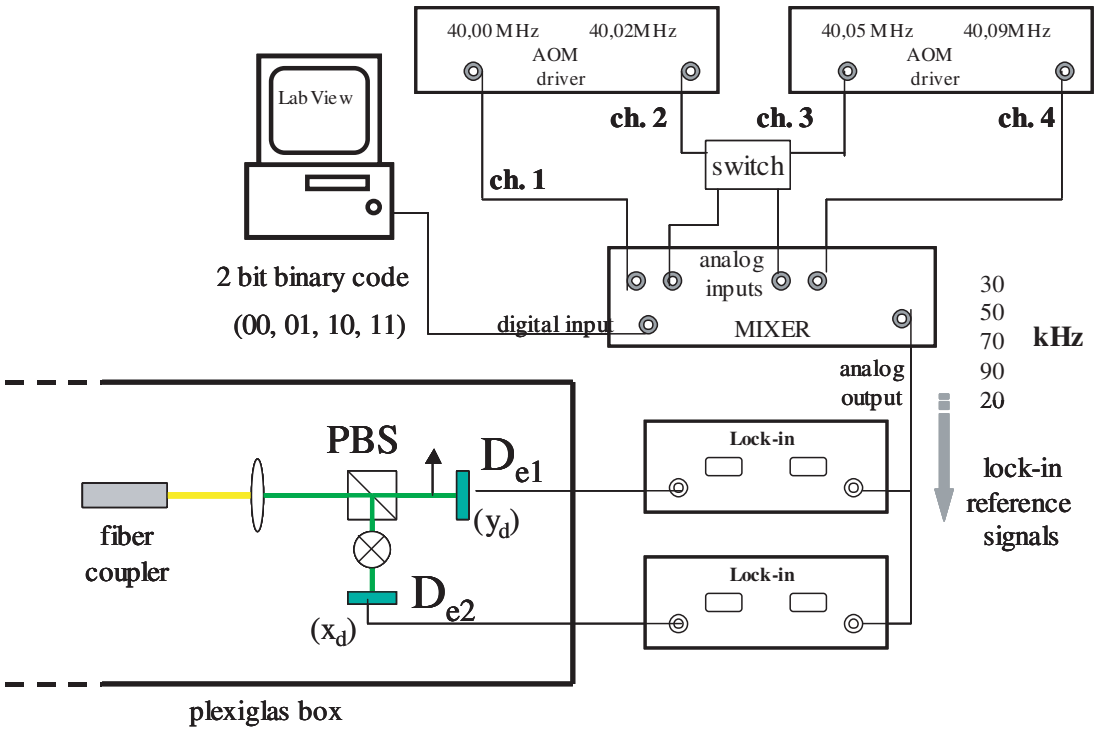

Figure 2.1: *Polarization sensitive detection system. The PBS automatically determines the coordinate system ($\widehat{x}_d$ - $\widehat{y}_d$).*

used in the multiple-steps procedure exposed in chapter 1 is substituted by a polarizer cube (PBS). The PBS splits the light from the fiber coupler into two linearly, mutually orthogonal,

polarized components. In this way, the detector coordinate system ($\widehat{x_d}$ - $\widehat{y_d}$) is automatically defined. The two components are separately detected by two photodiodes D_{e1} and D_{e2}. In both detectors, the superposition of reference and object beams generates heterodyne signals. The signals are coherently detected by means of a pair of lock-in amplifiers (*Stanford Research System, Model SR530*). The lock-in reference signals (LRS) are provided by an electronic system composed of the AOM drivers, a digital/analog mixer and a commercial PC. The AOM drivers are provided with low voltage output signals whose frequency modulation corresponds to the one used to excite the acoustic wave into the acouto-optic devices. This outputs can be mixed electronically in order to produce the same frequency modulations associated with the optical heterodyne signals. The mixing is operated by a home made mixer. It is provided with one digital input, four analog inputs and one analog output. The four analog inputs receive simultaneously the signals from the AOM drivers through channels 1, 2, 3 and 4. The signals are mixed two by two and are sent, through the analog output, to the reference channel of both the lock-in amplifiers. The frequency outputs are controlled by means of a 2 bit binary code provided by a commercial PC. A computer code, written with the commercial software LabView, allows to select the digital codes either one by one or in a closed loop sequence. The sequence of codes, mixed channels and relative LRS outputs are reported in Fig.2.2. In order to calculate the light

Code	Mixed Channels	Output LRS (kHz)
00	ch.1 –ch.4	90
01	ch.2 –ch.4	70
10	ch.1 –ch.3	50
11	ch.2 –ch.3	30
Switch on		
10	ch.1 –ch.2	20

Figure 2.2: *Table of computer generated codes, corresponding mixed channels and lock-in frequency signal (LRS) outputs . The LRS at 20kHz is obtained by activating the analog switch.*

ellipse parameters, we need to detect also the beat-signal between the two reference beams (i.e., 20kHz). The relative LRS cannot be coded in the digital sequence, which allows to select only four possible outputs. To this purpose, we provided the system with an analog switch which receives signals from channel 2 and 3. When the switch is on, ch.3 is deactivated and replaced by ch.2. In this way, by computer selecting code (10), the resulting LRS is modulated at 20kHz and the corresponding heterodyne signal can be coherently detected. Detectors D_{e2} and D_{e1} are home made silicon photodiodes with a bandwidth of $\Delta f = 62.5Hz$ at $T = 300K$, a $R_L \cong 1M\Omega$ and a quantum efficiency $\eta = 70\%$. At a wavelength of $\lambda = 532nm$ the resulting signal to noise ratio is $SNR = 45dB$. According to Eqs. (1.10) and (1.11), the accuracy in the amplitude and phase measurements are $\delta|E| = 6 \cdot 10^{-3}$ and $\delta\varphi = 6mrad$ ($\cong 2\pi/10^{30}$ or 0.33^{o} [26].

2.2.2 Signal processing algorithm

In a scanning probe experiment, we are interested in detecting the object beams properties which transport the information on the investigated field. We will describe now the algorithm used to determine the light vector associated to the object beams at the detector plane. The

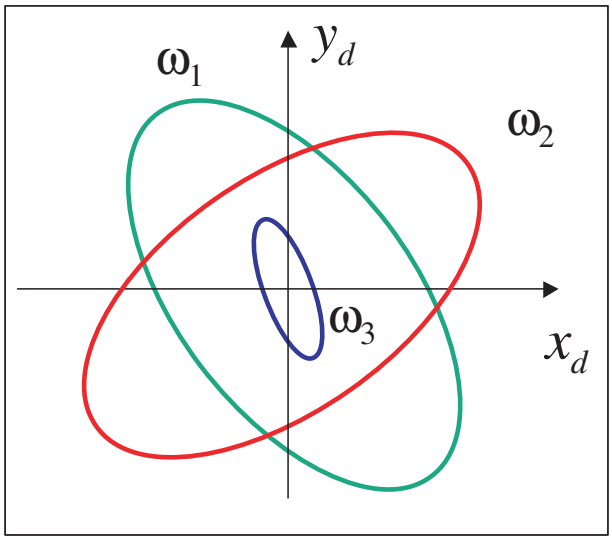

Figure 2.3: *General condition observable at the detector plane when both reference beams are superposed to an object beam. In a real experiment the ratio between the area swept by the object ellipse and the reference ellipses is much smaller then the one represented here.*

calculation is the same for both object beams of the MH-SPOM set-up, so we will proceed by describing the case of object beam 1 modulated at the angular frequency ω_3. When both reference beams are superposed in the coupler to the object beam, the situation at the detector plane is as depicted in Fig.2.3. Beam components along $\widehat{x}_d$ and $\widehat{y}_d$ are detected by detectors D_{e2} and D_{e1} respectively.
We first record the following series of signals

$$S_{r1,r2,xd,yd}(t) \propto 2A_{r1,xd,yd}A_{r2,xd,yd}\cos[(\omega_1-\omega_2)t-(\varphi_{r1,xd,yd}-\varphi_{r2,xd,yd})], \tag{2.1}$$

$$S_{r1,o1,xd,yd}(t) \propto 2A_{r1,xd,yd}A_{o1,xd,yd}\cos[(\omega_1-\omega_3)t-(\varphi_{r1,xd,yd}-\varphi_{o1,xd,yd})], \tag{2.2}$$

$$S_{r2,o1,xd,yd}(t) \propto 2A_{r1,xd,yd}A_{o1,xd,yd}\cos[(\omega_2-\omega_3)t-(\varphi_{r2,xd,yd}-\varphi_{o1,xd,yd})], \tag{2.3}$$

where $\mathrm{A}_{r1,xd,yd}$, $\mathrm{A}_{r2,xd,yd}$ and $\mathrm{A}_{o1,xd,yd}$ are the light vector components of reference beams 1 and 2 and the object beam 1 along axis $\widehat{x}_d$ and $\widehat{y}_d$ respectively. The same symbology has been applied to identify the corresponding phases $\varphi_{r1,xd,yd}$, $\varphi_{r2,xd,yd}$ and $\varphi_{o1,xd,yd}$. Eq. (2.1) represents the expressions for the beat-signal between the two reference beams on both detectors D_{e2} ($\widehat{x}_d$ axis) and D_{e1} ($\widehat{y}_d$ axis). Eqs. (2.2) and (2.3) are the analogues for the beat-signals between object beam 1 and reference beam 1 and 2 respectively. Once the three signals have been recorded, the object beam light vector components and their phase difference are straightforwardly calculated. By indicating with $\mathbf{S}_{r1,r2,xd,yd}$, $\mathbf{S}_{r1,o1,xd,yd}$ and $\mathbf{S}_{r2,o1,xd,yd}$ the amplitudes of the heterodyne signals in Eqs. (2.1) - (2.3), the light vector components are calculated as

$$A_{o1,xd,yd} \propto \sqrt{\frac{\mathbf{S}_{r2,o1,xd,yd}\cdot\mathbf{S}_{r1,o1,xd,yd}}{\mathbf{S}_{r1,r2,xd,yd}}}. \tag{2.4}$$

In Fig.1.8, we have explicitly represented the superposition of the light vector components of reference and object beams. One can notice that, in case in which the reference beam is circularly polarized, its light vector components are equal, and the heterodyne amplification factor is the same for both components of the object light vector. This condition can always be achieved by providing the reference fiber with a Babinet-Soleil polarization controller ($PolaRITE^{TM}$), which allows to modify at will the polarization state of the reference fiber output. Since the orthogonality of the reference beams is preserved by the fiber, in case of circularly polarization, one finds the following condition for the light vectors of the reference beams

$$\frac{A_{r1,yd}}{A_{r1,xd}} = \frac{A_{r2,xd}}{A_{r2,yd}} = 1, \tag{2.5}$$

and

$$(\varphi_{r1xd} - \varphi_{r2xd}) - (\varphi_{r1yd} - \varphi_{r2yd}) = \pm\pi \quad . \tag{2.6}$$

This conditions can be reproduced experimentally by acting on the polarization controller. In particular, for the phase difference in the two beams we will have

$$(\varphi_{r1yd} - \varphi_{r1xd}) = \pm\frac{\pi}{2}, \quad and \quad (\varphi_{r2yd} - \varphi_{r2xd}) = \mp\frac{\pi}{2}. \tag{2.7}$$

The phase difference of the object light vector is easily calculated from the heterodyne signals and Eqs. (2.7). By taking, for instance, the first of Eqs. (2.7), and by indicating with $\mathbf{\Phi}_{r1,o1,xd,yd}$ the heterodyne phase signals in Eq. (2.2), after a little algebra, we find

$$\varphi_{o1yd} - \varphi_{o1xd} = \mathbf{\Phi}_{r1,o1,yd} - \mathbf{\Phi}_{r1,o1,xd} \pm \frac{\pi}{2} \quad . \tag{2.8}$$

One can, alternatively, calculate the same value by using the heterodyne phase signal in Eq. (2.3) and the second of Eqs. (2.7).

2.3 Experimental determination of the MH-SPOM Jones matrix

Most optical elements are characterized by a Jones matrix, which allows to calculate the transformation of the light vector as an optical wave passes through the element. The definition of a similar matrix for the MH-SPOM is complicated by the presence of the scanning probe, whose vectorial properties are not yet well defined. When light couples to the probe, the light vector of the object field is modified by the interaction with the probe and by the successive propagation in the object fiber. Because the fiber and the probe constitute a single element, the two contributions cannot be discriminated. For this reason, we will investigate the possibility to define a Jones matrix for the system *probe+fiber*. As a first approach to the problem, we investigate the vectorial response of such a system to transverse optical fields. The goal of this experiment is illustrated in Fig.2.4. The tip is illuminated from below by both the object beams, which propagate parallel to the tip axis. We introduce an object plane coordinate system $(\widehat{x}_o, \widehat{y}_o)$ in the plane orthogonal to the tip axis, in which we define the Jones vectors associated to the beams. We want to determine a matrix J such that, if $E_{o1,2}$ are the light vectors of object beams 1 and 2 at the object plane, the transformed light vectors at the detector plane, $E_{d1,2}$, can be calculated as

$$E_{d1,2} = JE_{o1,2} \tag{2.9}$$

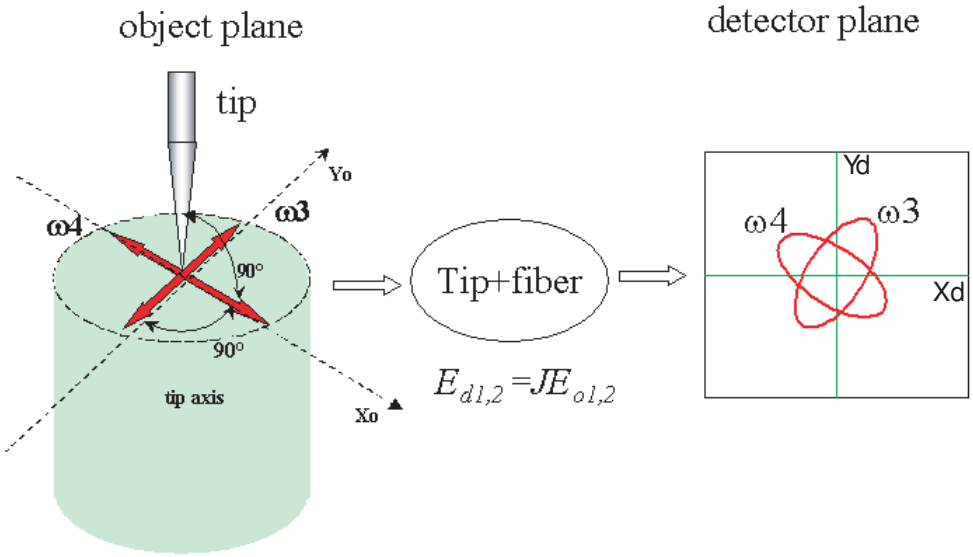

Figure 2.4: *The goal of the experiment is to calculate the Jones matrix of the system tip+fiber, which transforms vectors in the object plane into vectors at detector plane.*

In the previous section, we have introduced the signal processing algorithm which enables the measurement of the object beam light vectors by exploiting only heterodyne signals, without any handling of additional optical elements. We will use such an algorithm to characterize the Jones matrix, **J**, of the MH-SPOM. The experimental set-up is displayed in Fig.2.5.

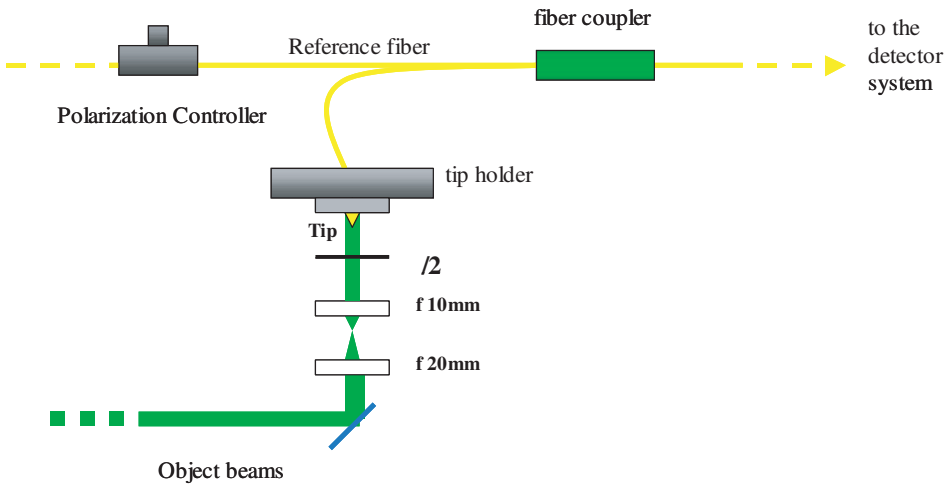

Figure 2.5: *Schematic for testing the calculation procedure for the MH-SPOM Jones matrix.*

Before reaching the probe, the object beams are collimated by a system of two lenses. As displayed in Fig. 2.4, we impose the object beams to be initially polarized along the axes of the object coordinate system. The Jones vectors have, therefore, the form

$$\mathbf{E}(\omega_4) = \begin{bmatrix} A_{o1,xo}e^{i\varphi_{o1xo}} \\ 0 \end{bmatrix} \quad , \mathbf{E}(\omega_3) = \begin{bmatrix} 0 \\ A_{o2,yo}e^{i\varphi_{o1xo}} \end{bmatrix}. \tag{2.10}$$

Elements J_{11} and J_{21} of $\mathbf{J}$ are determined by detecting $\mathbf{E}(\omega_4)$ as follows

$$\begin{bmatrix} J_{11} & J_{12} \\ J_{21} & J_{22} \end{bmatrix} \begin{pmatrix} A_{o1,xo}e^{\varphi_{o1xo}} \\ 0 \end{pmatrix} = \begin{pmatrix} A_{o1,xd}e^{i\varphi_{o1xd}} \\ A_{o1,yd}e^{i\varphi_{o1yd}} \end{pmatrix}$$

$$\Longrightarrow \begin{array}{l} J_{11}A_{o1,xo}e^{i\varphi_{o1xo}} = A_{o1,xd}e^{i\varphi_{o1xd}} \Longrightarrow J_{11} = \frac{A_{o1,xd}}{A_{o1,xo}}e^{i(\varphi_{o1xd}-\varphi_{o1xo})} \\ J_{21}A_{o1,xo}e^{i\varphi_{o1xo}} = A_{o1,yd}e^{i\varphi_{o1yd}} \Longrightarrow J_{21} = \frac{A_{o1,yd}}{A_{o1,xo}}e^{i(\varphi_{o1yd}-\varphi_{o1xo})}. \end{array} \tag{2.11}$$

The phase difference of J_{11} and J_{21} is found to be $(\varphi_{o1yd} - \varphi_{o1xo}) - (\varphi_{o1xd} - \varphi_{o1xo})$, which is obtained from Eq. (2.8). The remaining elements J_{12} and J_{22} are obtained similarly by using the second object beam in Eq. 2.10.

2.3.1 System testing

The procedure reported above allows to determine the elements of the Jones matrix of the system *tip+fiber*. In order to test the reliability of this calculation, we provided the MH-SPOM with an uncoated single-mode tapered fiber probe with a radius of curvature of 50nm (*Nanonics Ltd, Israel*). A SEM image of the probe apex is displayed in Fig.2.6. The testing procedure

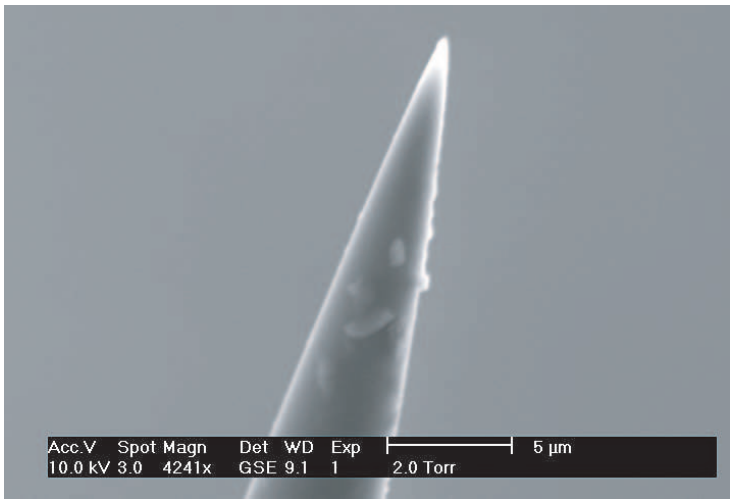

Figure 2.6: *SEM image of the very end part of the uncoated tapered fiber probe.*

consists in rotating the orientation of the linear polarizations in the object plane, and detecting the corresponding transformed vectors at the detector plane. The rotation is enabled by the Half-Wave Plate (HWP) reported in Fig.2.5. The HWP is mounted on a motorized rotating stage (*OWIS GmbH, Model DMT65, SM 440*) in order to adjust, without any handling, the plate axis orientation. Signals are recorded simultaneously for both the object beams.
We first calculate the Jones matrix for the field configuration at 0^o, which corresponds to vectors oriented along the coordinate axes (see Fig.2.4). Then, we proceed, with a series of discrete steps, by rotating the vectors from 0^o to 90^o. In Figs.2.7 and 2.8, we report the light ellipses measured at the detector plane, for beams 1 and 2 respectively, for the different angular steps. These results lead to interesting conclusions about the vectorial properties of the investigated probe. Firstly, the orientation of the light ellipse for beam 1 at 0^o looks nearly orthogonal to the corresponding ellipse of beam 2. The orthogonality condition is preserved for all the other intermediate orientations. Hence, we conclude that the orthogonality of the object beams is

preserved by the system *probe+fiber*. This behavior is generally expected when light propagates in the optical fiber. However, the reported results demonstrate that the orthogonality condition is preserved also in the interaction of the light with the nano-sized probe. Ellipses show different ellipticities, which depend on the birefringence of the whole system. On the other hand, we observe that the ellipse azimuths reproduce quite well the rotation angles of the object plane. Secondly, we observe that the light ellipse of beam 1 at 90° superposes quite well, both for orientation and shape, to the light ellipse of beam 2 at 0°. The same is observed for beam 2 with respect to beam 1. This result seems to suggest that, given the light vector orientation at the object plane, the transformation operated by the system can be calculated a priori. The last conclusion represents our most remarkable result, and we are in condition to verify it numerically.

The transformation, induced by the HWP on the Jones vectors at the object plane, can be

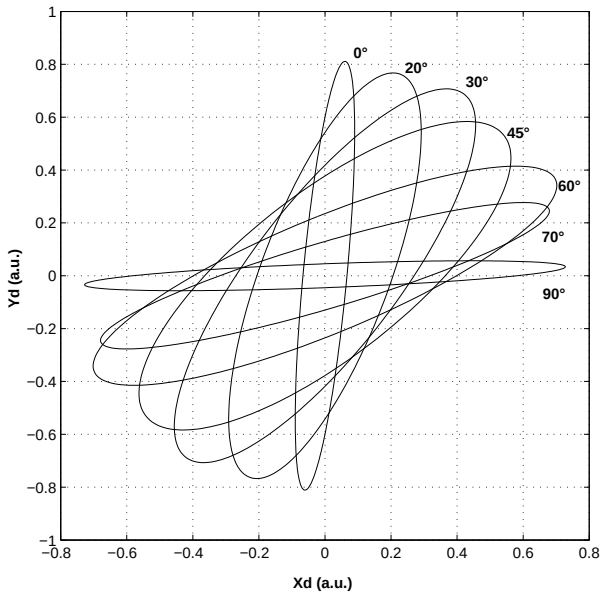

Figure 2.7: *Light ellipses recorded at the detector plane for object beam 1. Angles associated to each ellipse represent the corresponding angular rotation, θ, of the HWP at the object plane.*

expressed as

$$\mathbf{E}_{o1,2}(\theta) = \mathbf{R}(\theta)\mathbf{E}_{o1,2}(0^{\circ}), \tag{2.12}$$

where $\mathbf{R}$ is the rotation matrix and θ is the rotation angle. For each θ, the transformed vectors, at the detector plane, are calculated, by means of the Jones matrix, $\mathbf{J}$, as

$$\mathbf{E}_{d1,2}(\theta) = \mathbf{J}\mathbf{R}(\theta)\mathbf{E}_{o1,2}(0^{\circ}), \tag{2.13}$$

We compared the Jones calculus with the experimental results for the case of beam 1. Calculations of azimuth and ellipticity, for each value of θ, have been performed by means of Eqs. (1.18) and (1.19). A comparison of calculated versus experimental data, for both these parameters, is reported in Fig.2.9. The curves show a very good agreement. This result demonstrates that the system *tip+fiber* can actually be characterized by a Jones matrix, and that the procedure, proposed in this section, provides a reliable method to calculate it. We can observe, in Fig.2.9, that the ellipticity is more pronounced around 45°. This effect is also observable in the corresponding ellipse, in Fig.2.8, for the case of object beam 2. The fact that the ellipticity is not constant can be an indication of some asymmetry in the probe structure.

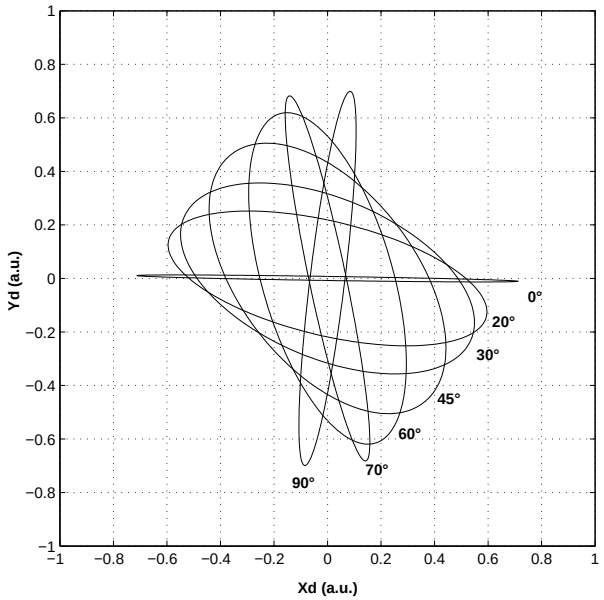

Figure 2.8: *Light ellipses recorded at the detector plane for object beam 2. Angles associated to each ellipse represent the corresponding angular rotation, θ, at the object plane.*

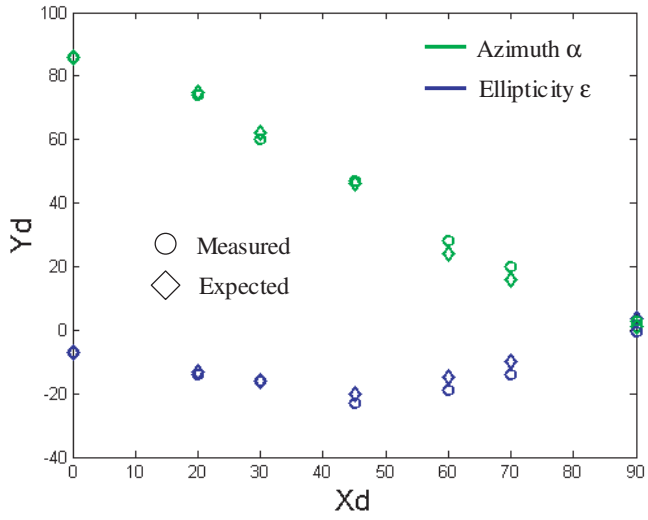

Figure 2.9: *Comparison of experimental and calculated light ellipse parameters for object beam 1.*

2.4 Conclusions

We have presented an electrooptical detection system which provides the MH-SPOM with the capability to detect the polarization state of the detected object beam. The Jones vector of the object light is measured at the detector plane by employing only heterodyne signals without any adding or handling of additional optical elements. The possibility to characterize the whole collection system by means of a single Jones matrix have been investigated. Such a possibility

is strictly related to the field vectorial response of the scanning probe. The system has been tested by mounting on the MH-SPOM a commercial uncoated tapered fiber tip. The response of the system to the illumination of transverse linearly polarized beams have been investigated in details. The reported results show that, in spite of probe nanometric fabrication features, the polarization response of the whole collection system is linear and that the transformation of the light vectors from the object to the detector plane can actually be determined by means of a Jones matrix. This conclusion represents a remarkable result, which opens the perspective to extend the application of a scanning probe microscope also to the studies of local properties of a generic optical field. In fact, if both the polarization state of the detected field and the transfer properties of the instrument are known, one can solve the inverse problem and determining the unknown polarization state of the probed field with subwavelength spatial resolution.

Chapter 3

Detection of Non-Paraxial Optical Fields by Optical Fiber Tip Probes

3.1 Introduction

In most experiment in Optics, the interaction of light with matter strictly depends on the vectorial properties of the electromagnetic field. In those configurations, in which the paraxial approximation is valid, electric and magnetic fields oscillate in planes orthogonal to the direction of propagation of the light wave. In this case, we deal with transverse electromagnetic waves. This condition is at least partially modified in those experiments in which light is constrained in waveguides [24] , or tightly focussed by means of microscope objectives [42]. In these cases, the field is no longer paraxial and both electric and magnetic fields present components in the direction of propagation. Therefore, these components are called *longitudinal*. In chapter 2, we have investigated the response of an uncoated tapered fiber probe to transverse fields. In this chapter we want to extend the investigation to the case of a 3D polarized field in which also longitudinal components appear.

Even though scanning probe fabrication processes have reached, nowadays, a high level of reliability, some aspects of the interaction of a nanometric probe with the vectorial characteristics of the optical field are still not fully understood. Until recently, this vectorial aspect was largely ignored, and in many cases this does not significantly affect the results: for example where the optical polarization is unambiguous in the scanning region [43]. However, as the techniques and applications of SNOM evolve and expand, the consideration of the optical field orientation and longitudinal fields in particular is increasingly important.

Recently, several experiments, which emphasize the vectorial properties of scanning probes, have been carried out. Special emphasis has been given to the response of the probe to longitudinally oriented electric field components. First, since the interaction of light with sub-wavelength structures produces non paraxial field configurations in which longitudinal field components are non negligible. Second, recent simulation results have shown that the resolution of some SNOM probes highly depends on the optical field polarization characteristics, providing the best performances with longitudinally polarized fields [44]. However, the ability of a scanning probe to couple these components is still not clear. Some experimental results demonstrated that the investigated probe was sensitive to such components [45,46]; on the contrary, some others found that the probe was unable, or partially able, to image optical patterns prevalently characterized by longitudinal fields [47, 48]. In most of these studies, the longitudinal field is generated by interaction of light with sub-wavelength structured materials or by focussing mechanisms. For

our experiment, we chose an extremely simple field configuration, still enabling the generation of a non paraxial field, with the appearance of longitudinal components. First, following the way traced in [49], we construct a crossed-beam interferometer to produce a 3D optical field configuration. Second, we exploit the labeling properties and the polarization sensitivity of our MH-SPOM to detect the different field components and extrapolate information on the longitudinal field coupling mechanism. Third, we introduce a simple coupling model to describe the mapping of the 3D optical fields scanned by the probe onto the two dimensional polarization eigenmodes of the single mode fiber. Finally, and most importantly, we exploit our techniques in order to compare the collection, or coupling efficiency, of the longitudinally polarized field components with respect to the transversely oriented components.

3.2 3D polarized optical configuration

Let us start our investigation by introducing the simple experiment in Fig. 3.1(a). As mentioned in the introduction, we will describe the field in a coordinate system which accounts for the geometry and the orientation of the probe. For this purpose, we define the coordinate system $(\widehat{x}, \widehat{y}, \widehat{z})$ in which the probe axis is parallel to the $\widehat{z}$-direction. The probe is illuminated at an angle θ by a plane wave having both TE and TM polarization components with respect to the plane of incidence. The electric field of the TE polarization has a single component, $\overrightarrow{E}_y$, parallel to $\widehat{y}$. Whatever the angle θ , the electric field is orthogonal to the plane of incidence and transverse with respect to the tip axis. In the case of the TM polarization, the field can be decomposed into a component, $\overrightarrow{E}_x$, transverse to the tip axis and a component, $\overrightarrow{E}_z$, parallel to it. If the tip scans the TM-polarized beam, both components will contribute to the excitation of the propagating modes in the fiber. However, in this configuration it is not possible to separate the contribution to the detected signal of the the individual components $\overrightarrow{E}_x$ and $\overrightarrow{E}_z$. In order to separate such contributions, the experiment can be modified as displayed in Fig 3.1(b).

A second similar beam is superposed onto the previous one, with each beam forming an angle of 45° with respect to the tip axis. For the TE polarization case, the two crossing beams are described by

$$\overrightarrow{E}_{TE1}(r,t) = E_{TE01}\begin{pmatrix} 0 \\ 1 \\ 0 \end{pmatrix} exp[i(\omega_{TE}t - k_{1x}x - k_{1z}z)] \quad and$$

$$\overrightarrow{E}_{TE2}(r,t) = E_{TE02}\begin{pmatrix} 0 \\ 1 \\ 0 \end{pmatrix} exp[i(\omega_{TE}t + k_{2x}x - k_{2z}z)], \tag{3.1}$$

where

$$\begin{cases} k_{1x} = k_{2x} = k/\sqrt{2} \\ k_{1z} = k_{2z} = k/\sqrt{2} \end{cases} \quad and \quad |k| = 2\pi/\lambda, \tag{3.2}$$

λ is the wavelength and ω_{TE} is the optical angular frequency. The resulting field in the region of superposition is

$$\overrightarrow{E}_{TE} = \overrightarrow{E}_{TE1} + \overrightarrow{E}_{TE2} = \begin{pmatrix} 0 \\ E_{TE01}e^{-ik_{1x}x} + E_{TE02}e^{-ik_{2x}x} \\ 0 \end{pmatrix} exp[i(\omega_{TE}t - k_z z)], \tag{3.3}$$

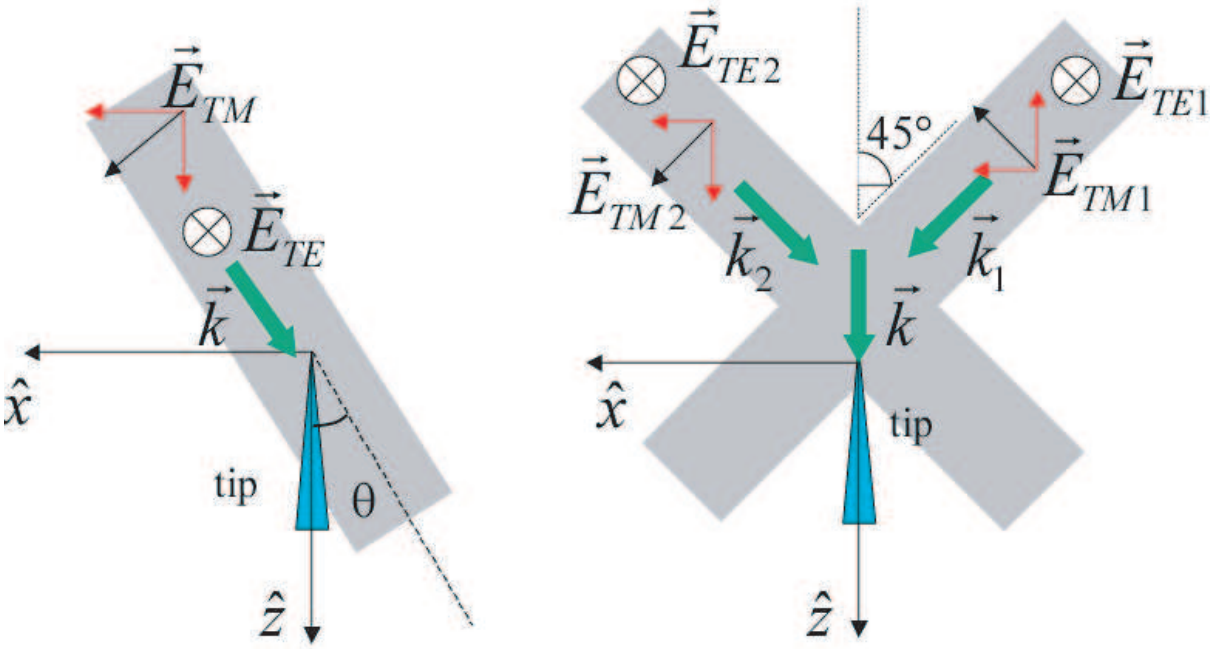

Figure 3.1: *(a) Superposed TE and TM polarized plane waves illuminate at an angle an uncoated tapered fiber probe. The optical field is transverse to the probe axis. The field lies in the plane of incidence and is decomposed into a component transverse and a component parallel to the probe axis. (b) The superposition of a second pair of plane waves intersecting the first at an angle of* 90^o*, generating a 3D field configuration including a longitudinal component.*

where $k_z = k_{1z} = k_{1z}$.
For the TM polarization, the fields are described by

$$\overrightarrow{E}_{TM1}(r,t) = \frac{E_{TM01}}{\sqrt{2}} \begin{pmatrix} 1 \\ 0 \\ -1 \end{pmatrix} exp[i(\omega_{TM}t - k_{1x}x - k_{1z}z)] \quad and$$

$$\overrightarrow{E}_{TM2}(r,t) = \frac{E_{TM02}}{\sqrt{2}} \begin{pmatrix} 1 \\ 0 \\ 1 \end{pmatrix} exp[i(\omega_{TM}t - k_{2x}x - k_{2z}z)], \tag{3.4}$$

where

$$\begin{cases} k_{1x} = k_{2x} = k/\sqrt{2} \\ k_{1z} = k_{2z} = k/\sqrt{2} \end{cases} \quad and \quad |k| = 2\pi/\lambda, \tag{3.5}$$

ω_{TM} is the optical angular frequency (possibly distinct from the TE case by the multiple heterodyne detection). In the region of superposition, the field is

$$\overrightarrow{E}_{TE} = \overrightarrow{E}_{TE1} + \overrightarrow{E}_{TE2} = \begin{pmatrix} E_{TM01}e^{-ik_{1x}x} + E_{TM02}e^{ik_{2x}x} \\ 0 \\ -E_{TM01}e^{-ik_{1x}x} + E_{TM02}e^{ik_{2x}x}0 \end{pmatrix} exp[i(\omega_{TE}t - k_z z)], \tag{3.6}$$

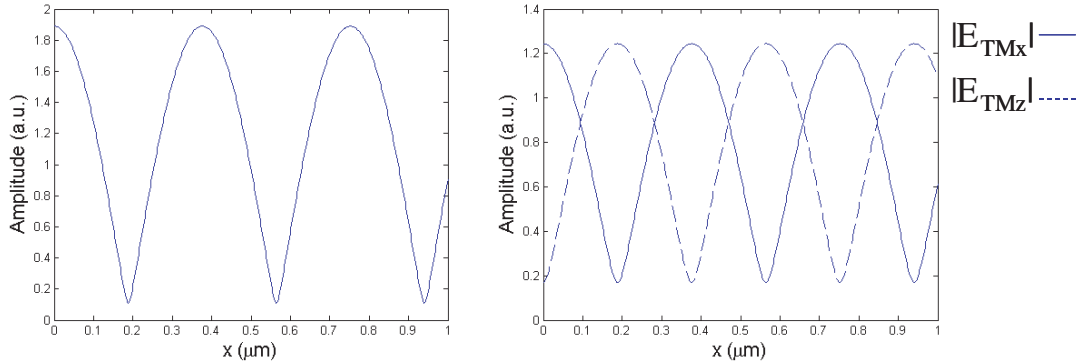

Figure 3.2: *(a) Absolute value of the total field amplitude, computed as a function of x, in the region of superposition, for TE polarization. (b) Absolute value of the field components,E_{TMx} and E_{TMz}, computed as a function of x, in the region of superposition, in the case of TM polarization.*

In Fig.3.2, we report calculations of the total E-field in the region of superposition, as a function of x, for both polarizations. Calculations were performed by taking in account the actual experimental ratio of the amplitude of the interfering beams. The ratios were measured by means of a powermeter, and were found to be $E_{TE1}/E_{TE2} = 0.89$ for the TE polarization and $E_{TE1}/E_{TE2} = 0.89$ for the TM polarization. In the field configuration depicted in Fig.3.1, TE polarized beams have parallel orientation of the electric fields, therefore, calculations lead to a conventional interference pattern. Note that this pattern is characterized by a sub-wavelength profile which could not be resolved by a classical microscope. We will see in the experimental section that this fundamental limit is overcome by scanning the nanoprobe in this region. The TM polarization case shows more interesting characteristics. In the case of equal amplitudes, $|E_{TM1}|/|E_{TM2}| = 1$, the resulting k-vector in the region of superposition gives

$$\overrightarrow{k} = \sqrt{2}\begin{pmatrix} 0 \\ 0 \\ k \end{pmatrix}. \tag{3.7}$$

We find that the resulting wave vector is parallel to $\widehat{z}$. As a consequence, the z component of the electric field has the characteristics of a longitudinal field. Secondly, in the plane of intersection, the electric fields of the TM polarized beams are orthogonal, therefore, they do not interfere. Nevertheless, as displayed in Fig.3.2, computation of the individual components $\overrightarrow{E_x}$ and $\overrightarrow{E_z}$ shows that they are periodic functions of x, shifted by a quarter of the period $\lambda/\sqrt{2}$. Therefore, there are locations where only one of the two components, $\overrightarrow{E_x}$ or $\overrightarrow{E_z}$, is dominant. This situation will be exploited to separately detect the conversion of the transverse and the longitudinal components of the field by the fiber tip. The contribution of the TE and TM polarizations are discriminated by means of the multiple heterodyne detection system.

3.3 Coupling model

The characteristics of the scanning probe investigated in this experiment have been already described in chapter 2. In particular, we have mentioned that the fiber probe is a single mode

fiber. Bulk single-mode fibers are weakly guiding and support only two orthogonally polarized propagating modes . Therefore, although the optical field to be probed may have a 3-D polarization configuration, the optical field, that is carried by the single-mode fiber to the detector, will be reduced to a 2D polarization state. In order to investigate the polarization-dependent coupling properties of the scanning probe, we introduce a coupling model which accounts for the mapping of the 3-D fields scanned by the probe onto the 2D basis of the propagating modes in the fiber. We define two polarization states in the fiber probe, $\overrightarrow{E_u}$ and $\overrightarrow{E_\nu}$, such that

$$\overrightarrow{E}_u \cdot \overrightarrow{E}_\nu = 0. \tag{3.8}$$

Any propagating mode can be expressed as a linear combination of $\overrightarrow{E}_u$ and $\overrightarrow{E}_\nu$. Without any loss of generality, we assume that the $\overrightarrow{E}_u$ mode is excited when the probe couples to the TE polarization. In this case, we can assume that:

$$\overrightarrow{E}_u \propto \overrightarrow{E}_{TE}. \tag{3.9}$$

Since the TE polarization is transverse with respect to the tip axis, the relationship of proportionality with a transverse fiber mode, in Eq. (3.9), is quite intuitive.
A more complex situation arises when the tip couples to the TM-polarized field. In this case, the field is decomposed into a component $\overrightarrow{E}_{TMx}$, transverse to the tip axis and a component $\overrightarrow{E}_{TMz}$ parallel to it. The transverse component lies in the plane of intersection of the two beams and is orthogonal to the TE polarization. In chapter 2, we have demonstrated, by means of the polarization sensitive detection system, that the condition of orthogonality of linearly polarized fields is preserved by the collecting system of the MH-SPOM. On the basis of this information, and according to Eqs. (3.8) and (3.9) we assume this component to excite only the mode $\overrightarrow{E}_\nu$. As observed in section 3.2, the component $\overrightarrow{E}_{TMz}$ has, in the region of superposition, the characteristics of a longitudinal field. Propagation in the fiber can occur only via transformation into a transverse mode. Unlike the previous two cases, it is not possible to predict which mode will be excited and so we assume that the component $\overrightarrow{E}_{TMz}$ contributes to the excitation of both $\overrightarrow{E}_u$ and $\overrightarrow{E}_\nu$. Therefore, for the case of the TM polarized field, we can write:

$$\overrightarrow{E_u} \propto c_u \overrightarrow{E}_{TMz}, \tag{3.10}$$

and

$$\overrightarrow{E_\nu} \propto c_\nu \overrightarrow{E}_{TMz} + \overrightarrow{E}_{TMx}, \tag{3.11}$$

where c_u and c_ν are complex coefficients which account for the transformation of the longitudinal field into the two transverse fiber modes $\overrightarrow{E_u}$ and $\overrightarrow{E_\nu}$, respectively. It is worthwhile to remark that in the most general case c_u and c_ν are complex values, because they have to take into account a possible phase delay between the transformation of the longitudinal and transverse components of the field into the propagating eigenmodes of the fiber.

3.4 Signal Detection

In Fig.3.3, is displayed the optical arrangement which was used to generate the field configuration, discussed in section 3.2, (see Fig3.1(b)). The object channel (superposition of the TE and TM polarized beams) is split in two by means of the beam splitter (BS). Two mirrors, M1 and M2 are placed at equal distance from the reflecting surface of BS and oriented at 45^o with respect to the BS facets. Once reflected on mirrors M1 and M2, the beams superpose with an

angle of 90°. The probe is scanned in the region of superposition with its axis oriented parallel to the bisectrix of the angle formed by the light beams. This orientation corresponds to the condition in which the probe axis is parallel to axis $\widehat{z}$. The tip is mounted on a x-y-z piezoelectric closed loop translation stage (*Physik Instrumente GmbH, Model P-517-3CL*). This scanner is a solid-state actuator, allowing nano-metric displacements, whose resolution is basically limited by the noise in the piezo amplifier which provides the voltage to the piezo-material cells. The resolution of the step displacement in z-direction is 0.1 nm and 1 nm in the x and y directions. Light collected into the probe is detected by the detection system presented in chapter 2. According to Eqs. (3.10) and (3.11), we assume, that as soon as light couples into the probe,

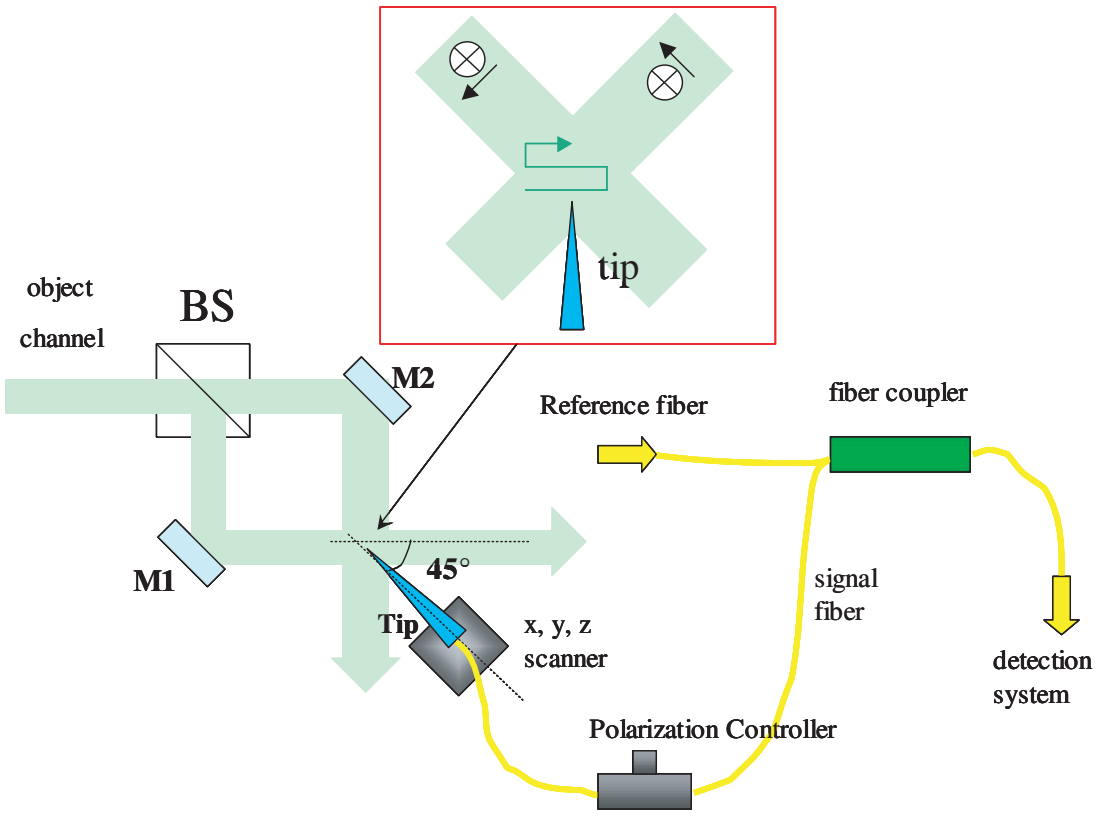

Figure 3.3: *Optical arrangement for the construction of the 3D field.*

it excites a linear combination of the fiber eigenmodes. At the exit of the fiber coupler (see Fig.2.1), the output beam, which contains the superposition of the fields $\overrightarrow{E_u}$ and $\overrightarrow{E_\nu}$, is split into two orthogonal components by means of the (PBS). In the most general case, the two beams generated after the PBS, will result from a linear combination of $\overrightarrow{E_u}$ and $\overrightarrow{E_\nu}$. By indicating with $\mathbf{S}_{De1}$ and $\mathbf{S}_{De2}$ the signals detected by detector D_{e1} and D_{e2} respectively, we can express their values in the following form:

$$\begin{pmatrix} \mathbf{S}_{De1} \\ \mathbf{S}_{De1} \end{pmatrix} \propto \mathbf{J} \begin{pmatrix} E_u \\ E_\nu \end{pmatrix}, \tag{3.12}$$

where $\mathbf{J}$ is the Jones matrix of the collecting system.
To identify the Jones matrix, we first illuminated the tip only with the TE polarization. In the general case, the output of the fiber at the detector plane will be elliptically polarized,

depending on the birefringence of the fiber. This means that both object beams are expected, in general, to excite a linear combination of $\overrightarrow{E_u}$ and $\overrightarrow{E_\nu}$. We are mostly interested in analyzing the signal produced by the TM polarization. In fact, the superposition of the TM polarized beams generates the longitudinal component that we wish to investigate. For this purpose, we chose to put ourself in the particular condition in which the TE polarized light excites only one of the eigenmodes, as indicated by Eq. (3.9), and that this mode corresponds to a linear polarization oriented parallel to $\widehat{y_d}$. In this case, the signal generated by the TE polarization is detected only by D_{e1}. In order to obtain this condition, we provide the signal fiber with a polarization controller. When only TE light is coupled to the probe, one can control the polarization of the output beam in order to reach the required condition. The advantages of looking for this circumstance will be evident in the following discussion. Firstly, we observe that, if mode $\overrightarrow{E_u}$ is detected only by D_{e1}, for the orthogonality of the base $\{E_u, E_\nu\}$, we expect mode E_ν to be detected only by D_{e2}. Therefore, the Jones matrix in Eq. (3.12) becomes the identity matrix:

$$\begin{pmatrix} J_{11} & J_{12} \\ J_{21} & J_{22} \end{pmatrix} = \begin{pmatrix} 1 & 0 \\ 0 & 1 \end{pmatrix} \tag{3.13}$$

The experiment is carried out by scanning the probe along lines parallel to $\widehat{x}$ (see Fig.3.1(b), and inset in Fig.3.3), with its axis parallel to $\widehat{z}$. The detected signals are proportional to the amplitudes of the excited modes in the fiber probe. By combining Eqs. (3.3) and (3.6) for the field distribution and the equations (3.10) and Eqs. (3.11) for the excited fiber modes, it possible to predict the pattern of the detected signals during the scan. According to Eq. (3.9), for the TE polarization the signal detected by detector D_{e1} is proportional to $|E_u|$. It follows:

$$|E_u| \propto \left[|E_{TE01}|^2 + |E_{TE02}|^2 + 2|E_{TE01}||E_{TE02}| \cos(2{\cdot}k_x x + \phi_{TE}) \right]^{\frac{1}{2}}. \tag{3.14}$$

As the interfering fields are parallel, an interference term appears in Eq. (3.14). The phase value ϕ_{TE} accounts for the relative offset of the interfering beams.
For the TM polarization, the expressions for the transverse and the longitudinal components of the electric field, as they are seen by the fiber tip, are obtained from Eq. (3.6) as

$$E_{TMx} = E_{1x} + E_{2x} = \frac{1}{\sqrt{2}} \Big[E_{01} e^{-ik_{1x}x} + E_{02} e^{ik_{2x}x}] exp[i(\omega_{TM} t - k_z z)] \tag{3.15}$$

and

$$E_{TMz} = E_{1z} + E_{2z} = \frac{1}{\sqrt{2}} \Big[- E_{01} e^{-ik_{1x}x} + E_{02} e^{ik_{2x}x}] exp[i(\omega_{TM} t - k_z z)], \tag{3.16}$$

where ϕ_{TM} is the relative offset of the interfering beams for the TM polarization.
In this case, both E_u and E_ν are excited. By substituting Eqs. (3.15) and (3.16) in Eqs. (3.10) and (3.11) respectively, we obtain for the expected detected amplitudes:

$$|E_u| \propto \left\{ |c_u| \cdot \left[\frac{|E_{01}|^2}{2} + \frac{|E_{02}|^2}{2} - |E_{01}||E_{02}| \cos(2{\cdot}k_x x + \phi_{TE}) \right] \right\}^{\frac{1}{2}} \tag{3.17}$$

and

$$|E_\nu| \propto \Bigg[\frac{|E_{01}|^2}{2} |1 - |c_\nu e^{i\phi\nu}|^2| + \frac{|E_{02}|^2}{2} + |1 + |c_\nu e^{i\phi\nu}|^2| +$$

$$|E_{01}||E_{02}|[(1 - |c_\nu|^2|) \cos(2{\cdot}k_x x + \phi_{TM}) + 2|c_\nu| sin(\phi\nu) sin(2{\cdot}k_x x + \phi_{TM}) \Bigg]^{\frac{1}{2}}, \tag{3.18}$$

where ϕ_ν is the phase of the complex coefficient c_ν . The phase ϕ_{TM} accounts for the relative offset of the interfering beams . We observe that Eq. (3.17) depends only on the modulus of the coupling coefficient c_u , while Eq. (3.18) depends on both the modulus and the phase of the coupling coefficient c_ν.

3.5 Experimental results

In Fig. 3.4 we report the amplitude signals recorded by detectors D_{e1} and D_{e2} while the probe was scanned over a length of $1\mu m$ detecting TE polarized light. As expected, only detector D_{e1} recorded a significant signal, while the signal in D_{e2} was close to zero. The expected interference pattern was reproduced experimentally, as confirmed by comparison of the two curves in Fig.3.4. The expected amplitude pattern can be computed using Eq. (3.14). As

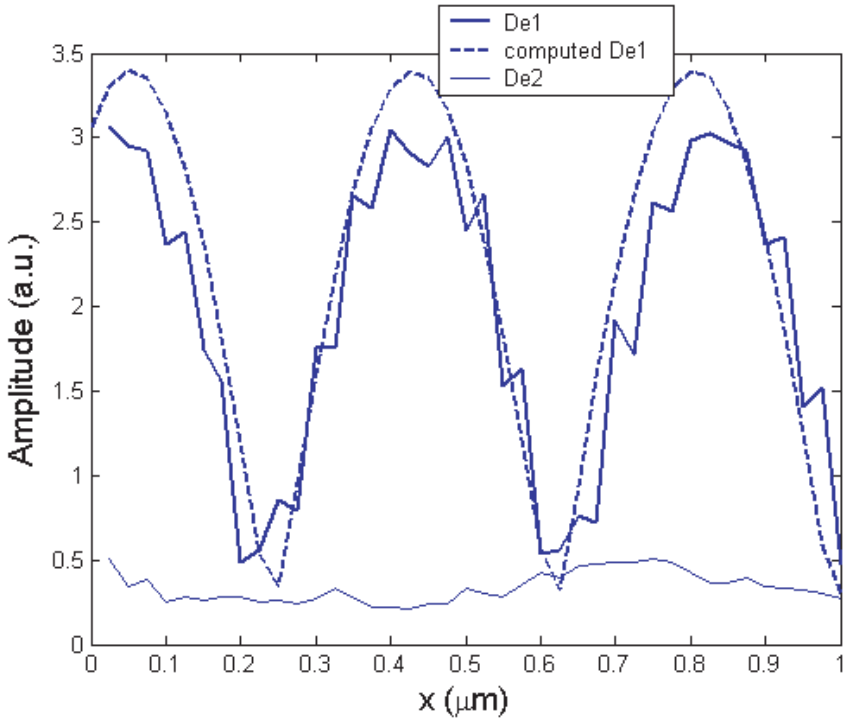

Figure 3.4: *Amplitude signal (solid lines) recorded by scanning the probe parallel to x in the region of intersection of the TE polarized beams. The scan was performed over a line of* $1\mu m$ *with a step of 25 nm. Only detector De1 detected a significant signal. The expected computed profile is also shown (dashed line).*

mentioned in section 3.2, (see Fig.3.1(a)), in the case of the TE polarization it is possible to estimate separately the amplitudes of the interfering beams as they are detected through the probe. These values produced an amplitude ratio of 0.86 which is in good agreement with the amplitude ratio,0.89, of the illuminating beams measured by means of the power meter. This result suggests that the tip response is predominantly symmetric with respect to the two beams. The numerical values of the probed amplitudes have been introduced in Eq. (3.14) in order to calculate the expected pattern of interference. The arbitrary phase offset ϕ_{TE} was chosen in order to align the calculated and experimental curves. We observe a very good agreement

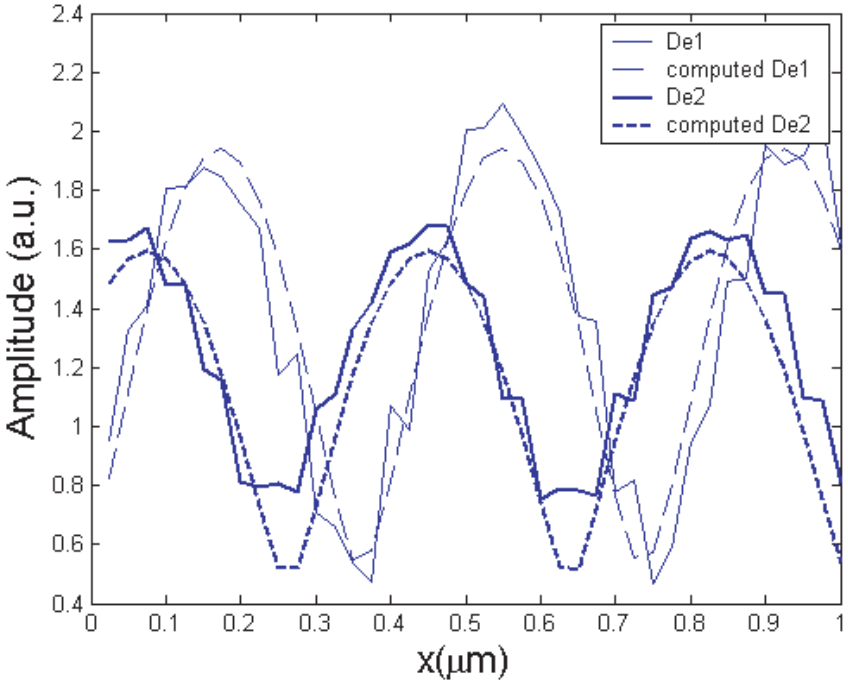

Figure 3.5: *Amplitude signal recorded by scanning the probe parallel to x in the region of intersection of the TM polarized beams. Both detectors detect a significant signal. The experimental data (solid lines) are compared to the results of a multi-parameter curve fit (dashed lines) to determine the complex coupling coefficients and* c_ν *and* c_u.

between the calculated and experimental curves. While no signal is expected in the other detector, we observe a nearly constant value of approximately 0.4 at D_{e2}, which is probably due to stray light. In Fig.3.5, we report the recorded signals detected when the tip simultaneously scanned the TM polarization. In this case, we see that both detectors record a significant signal characteristic of a fringe pattern. According to Eqs. (3.17) and (3.18), this means that in addition to transverse components of the field the longitudinal one contributes to the detected signal. In particular, we observe that because of its orthogonality to TE polarization, the transverse component should be detected only by detector D_{e2}. According to Eq. (3.18) the total signal will be given by the contribution of the transverse and by a partial contribution of the longitudinal component. On the other hand, detector D_{e1} will measure only a contribution from the longitudinal component. The weight of these contributions depends on the coupling coefficients. We observe that Eqs. (3.17) and (3.18) depend on four unknown parameters which are the amplitudes and the phases of the complex coupling coefficients. An estimation for these parameters can be achieved by fitting the experimental data with the theoretical equations. As mentioned in section 3.2, in the case of the TM polarization it is not possible to estimate the amplitudes of the single components of the interfering fields as they are detected through the probe. The only accessible information is the amplitude ratio $|E_{TM2}|/|E_{TM1}| = 0.76$ of the illuminating beams measured by means of the power meter. Introducing the parameter A such that $E_{TM1} = A$, and, consequently, $E_{TM2} = 0.76A$, we obtain, from Eqs. (3.17) and (3.18), the

expressions

$$|E_u| \propto |c_u| \cdot A \left[\frac{1}{2}(1 + 0.578) - 0.76 \cdot \cos(k_x x + \phi_{TE}) \right]^{\frac{1}{2}} + A_{De1}, \tag{3.19}$$

$$|E_\nu| \propto A \Bigg\{ \frac{1}{2}|1 - |c_\nu e^{i\phi\nu}|^2| + \frac{1}{2}(0.76)^2 + |1 + |c_\nu e^{i\phi\nu}|^2| +$$

$$0.76 \cdot [(1 - |c_\nu|^2|) \cos(2 \cdot k_x x + \phi_{TM}) + 2|c_\nu| sin(\phi\nu) sin(2 \cdot k_x x + \phi_{TM}) \Bigg\}^{\frac{1}{2}}. \tag{3.20}$$

A non-zero amplitude offset A_{De1} is added to better fit Eq. (3.19) to the measured curves. This offset is attributable to stray light, similar to the one observed in Fig.3.4 for D_{e2} . The phase ϕ_{TM} in Eqs. (3.19) and (3.20) accounts for an offset of the interfering beams.

The values of c_ν, ϕ_ν, A and ϕ_{TM}, which best fit Eq. (3.20) to the experimental data, were found by applying a *polynomial least square* algorithm. The calculated parameters, A and ϕ_{TM}, are then used in Eq. (3.19) to find the best value for c_u. The numerical values which best fit Eqs. (3.19) and (3.20) to the experimental data are reported in Table 1.

The calculated curves are shown in Fig.3.5 together with the experimental data. We observe

$A = 1.3$	$\|c_\nu\| = 0.80$	$\|\phi_\nu\| = 1.7rad$	$\|c_u\| = 0.71$	$\phi_{TM} = -1.46rad$	$A_{De1} = 0.3$

Table 3.1: *Parameters obtained from the polynomial least squares fit of the predicted and experimental results. Parameters $|c_u|$, $|c_\nu|$ and $|\phi_\nu|$ describe the coupling of the longitudinal field component with the probe.*

that Eq. (3.20) does not depend on the parameter ϕ_u , therefore it is not possible to determine its numerical value. The numerical values of $|c_u|$ and $|c_\nu|$ represent the relative coupling efficiencies of the longitudinal field component with respect to the transverse component for the two orthogonal polarizations in the fiber. We find $|c_u| = 0.80$ and $|c_\nu| = 0.71$. It is very important to note that these values are not vanishingly small; they are on the order of magnitude of 1. Thus, these results demonstrate that, at least for this probe, in this 3D field configuration, the longitudinal field component couples to the tip with an efficiency comparable to that of the transverse field component. This conclusion is also in agreement with previously reported results in similar optical configurations [19]. The calculated value for $|\phi_\nu|$ corresponds to a phase delay of approximately 95^o between the coupling of the transverse and the longitudinal components. The modulated patterns in Fig.3.5 show that the spatial shift between the maxima of interference does not correspond to the one displayed in Fig.3.2. This is due to the fact that the coupling process is accompanied by the introduction of the additional phase $|\phi_\nu|$. Numerical calculations also showed that this parameter is responsible for the observed shift, while the amplitude values of the coupling coefficients affect only the relative values of the signal amplitudes and the contrast of the interference fringes.

3.6 Conclusions

In this chapter, we have introduced an experimental technique for the investigation of the vectorial response of a scanning probe to 3D optical fields including longitudinal components. The

technique has been demonstrated in the case of an uncoated tapered fiber tip. The three dimensional field has been produced by the interference of two beams, each consisting of superposed TE and TM polarized fields, producing an interference pattern having a nonzero polarization component along each cardinal axis of the probe frame of reference. The different polarizations have been measured simultaneously but independently by means of a multi-heterodyne scanning probe microscope. The tip was scanned in this 3D field zone, and this configuration permitted the characterization of the relative coupling efficiency of a longitudinally oriented electric field with respect to the transverse orientation. These results indicate that, for the investigated tip, the coupling efficiency of the longitudinal field is approximately equal to the coupling efficiency of the transverse field components. Further experimental investigation with different field configurations will be necessary to understand the 3D polarization coupling completely and to develop a more detailed electromagnetic coupling model.

Chapter 4

Selective Coupling of HE_{11} and TM_{01} modes into Microfabricated Fully Metal-Coated Quartz Probes

4.1 Introduction

In the previous chapter we have investigated the vectorial response of an uncoated tapered fiber probe to transverse and longitudinally polarized fields. Such properties have been determined by exploiting conventional and novel capabilities of the MH-SPOM.
In this chapter, we investigate the electromagnetic properties of a standard fully metal-coated micro-fabricated cantilevered probe designed for SNOM operation in illumination mode. This technique relies on the generation of local nano-sources at the end of narrow probes brought in proximity of the sample to illuminate [13]. Such a confined source can be achieved by opening a nano-aperture at the apex of a metal-coated tapered fiber [3]. However, the need to providing the probe with an aperture for the field transmission (collection) revealed itself to be a misconception. In 1995, Novotny *et al.* first demonstrated theoretically the transmission properties of the fundamental HE_{11} mode through a fully metal-coated fiber tip [58]. Light focussed at the apex of the aperture-less probe showed an even better confinement compared to the case of an aperture probe. Beside the perspective of improving the lateral resolution, aperture-less probes are preferable to aperture probe for additional reasons. Firstly, the opening of the aperture in the metallic layer demands additional and delicate fabrication processes, which are not always reliable. Secondly, an aperture probe, compared with uncoated tapered fibers and aperture-less tips, is more susceptible to be damaged in the interaction mechanisms with the sample surface. However, the mechanisms that rule the propagation of the light through the probe are complicated by the subwavelength features of the structure, and still represent a subject of investigation. Interesting alternatives have been proposed in a series of papers in which the possibility to achieve an apertureless probe by using a single scattering molecule is investigated [59–61].
In the next sections, we present both a theoretical and an experimental study of the transmission optical properties of a standard micro-fabricated fully metal-coated probe. The numerical investigation is carried out by introducing a 3D model of the structure. Calculations of both internal guided modes and external throughput are carried out by solving the Maxwell's equation in a finite volume surrounding the probe structure, by means of a Finite Difference Time Domain (FDTD) algorithm. The theoretical study individuates two modes of particular interest that we investigate in detail: the fundamental linearly polarized HE_{11} and the radially polarized TM_{01}.

The experimental work has been conducted by means of a high resolution Mach-Zehnder microscope. The set-up is provided with an acquisition software, which allows to record intensity and phase of the imaged optical patterns, and a liquid crystal element for the generation of axially symmetric polarized beams. Contrarily to the case of a typical SNOM experiment, the fields investigated in this work are not purely evanescent and present propagating components. Since the microscope records field patterns at a few microns from the probe apex, we expect this region to be still characterized by a superposition of evanescent and homogeneous waves. For this reason, we will indicate this region as the intermediate-field.
By combining theoretical and experimental results, we demonstrate that the injection of the HE_{11} and TM_{01} modes can be selectively operated by choosing suitable injection conditions.

4.2 Light propagation in metalized scanning probes

Light transmission and propagation in waveguide devices have been widely treated in modern literature [24, 50]. When light is constrained into a finite domain, the field distribution, in a plane transverse to the direction of propagation, is influenced by the geometry and the material of the waveguide structure. In a canonical waveguide, the medium in which the light propagates is called the *core*. The core is generally embedded into a different material, characterized by a lower diffractive index, which is called the *cladding*. The main propagation mechanism is the total internal reflection at the interface between the two media. The propagation of an electromagnetic wave in a finite structure requires the optical field to satisfy some boundary conditions which account for the properties of the electric and the magnetic field at the boundaries between the core and the cladding. These conditions are, in general, satisfied for a discrete number of field distributions, therefore, the modes into a waveguide cavity are quantized. Given the geometry and the material, the different modes are classified according to a certain order. In general, a regularly structured waveguide owns some transverse space symmetries on the basis of which one can classify the field distributions associated to the propagating modes.
In cylindrical hollow metal waveguide, a dielectric core is surrounded by a metallic layer. The supported modes are commonly indicated as TE_{nm} (Transverse Electric) or TM_{nm} (Transverse Magnetic) [51]. In the first case, the electric field lays on a plane orthogonal to the direction of propagation. The second group of modes are, instead, characterized by a prevalent transverse distribution of the magnetic field. The index n accounts for the angular symmetry of the mode, whereas the index m denotes the radial dependence of the field. In the case of an ideal step-index fiber, modes are neither pure transverse electric nor transverse magnetic, and they are indicated as *hybrid*. As these modes are almost TM or almost TE, they are classified as EH_{nm} and HE_{nm} respectively.
The problematic related to the classification and the propagation characteristics of the electromagnetic field in a cylindrical metallic waveguide has been discussed in a theoretical review paper by Novotny *et al.* in 1994 [52]. The review reports several results which can be applied to the theoretical study of the electromagnetic properties of metalized scanning probes. First, it is analyzed the case of a waveguide with an infinite cladding, then the case of a bulk metallic waveguide. The results for the first two cases are finally combined to get an insight into the properties of a realistic (finite cladding, finite core) metallic waveguide. Mode properties are derived as a function of the core radius and the optical frequencies. As it will be clarified later on in this work, we are mostly interested in the mode dependence on the core diameter, and both experimental and theoretical analysis are conducted at a single wavelength. As a function of the core radius, ρ, the analysis of the modes shows interesting properties. Firstly, when ρ is large, compared to wavelength, the waveguide has multimodal characteristics. This means

that several of the quantized modes can propagate in the waveguide with different propagation constant. In [52], it is shown that, as ρ decreases, most modes run first into a transition from propagating to evanescent modes, then they completely vanish when the core radius reaches the *cutoff* value.
In this chapter, we investigate some transmission properties of a fully metal-coated cantilevered probe conceived for SNOM operated in illumination or illumination-collection mode. This kind of probes have, in general, cylindrical symmetric conical shape, characterized, at the apex, by a very narrow radius of curvature (typically of some tents of nanometers) [44, 54–56]. Alternative geometries are, for instance, proposed in [53]. In a typical probe, then, as light propagates towards the apex, the geometry of the waveguide is modified and its core radius becomes smaller and smaller. As recently suggested by Hecht *et al.* [57], the results reported in [52] can be used to describe the evolution of the modes propagating in a tapered fiber. One can assume that, as a mode propagates in the probe, it experiences a change in its propagation constant, due to the decreasing of the radius core, which eventually leads to a transition to an evanescent wave or to a complete vanishing. The mechanisms which determine the vanishing of a mode can be many and not yet well-established in the concerned literature. A mode can, for instance, be reflected back into the structure, or coupled to surface modes and subsequently radiated in vacuum. We see, then, that cutoff radius is a crucial parameter and its determination is extremely useful because it indicates which modes are likely to survive till the very end of the tip and then contribute to the probe throughput. Unfortunately, it is found in [52], that most modes run into cutoff for core radii much larger than the typical radius of curvature of the very end of the probe. However, there is another interesting aspect of the propagation of the light in the probe core which has to be taken in account. Actually, propagation can be accompanied by mode transformation mechanisms. In fact, the propagation constant of a given mode can, at a certain point in the structure, match the one associated to a surface mode. In this circumstance, we can have a mutual coupling of a core into a surface mode. A surface mode propagates with different mechanisms which can eventually transmit a ratio of the carried energy as far as the probe apex. From this point of view, there are two modes of particular interest: the linearly polarized mode HE_{11} , and the radially polarized mode TM_{01}.
Contrarily to higher order modes, the fundamental mode HE_{11} does not present a real cutoff. Actually, its transition from propagating to evanescent occurs at a distance sufficiently close to the tip apex to allow the transfer of its energy to surface modes or directly to the bulk cladding. If the cladding is sufficiently thin, the evanescent field can penetrate till the end of the structure. The distance from the probe apex, at which the transition to the evanescent mode occurs, depends on the cone angle of the taper. In fact, it has been demonstrated, in [58], that larger cone angles would drastically improve the transmission of such a mode through the probe apex. The radially polarized mode TM_{01} has a larger cutoff compared to the mode HE_{11}. However, as the core radius decreases, its propagation constant increases. This circumstance leads to the possibility of coupling the TM_{01} to surface plasmons. The idea that surface plasmons can propagate on the surface of a metal-coated fiber tip has been advanced 1999 by Keilmann [63] and demonstrated numerically by Bouhelier *et al.* in 2002 [62]. The coupling mechanism is similar to the one occurring in the well-known Kretschmann configuration applied to the excitation of surface plasmons on planar structures. An important, role in the coupling mechanism, is played by the cladding thickness. It was in fact demonstrated by Rather in 1988 [65], that the plasmon excitation is optimized for certain thickness of the metal layer. Investigations on the optimum thickness value for the cladding layer, in the case of gold coating and a cone aperture of 20^{o}, are also reported in [62]. Optimum thickness are found in the range between 50 and 70 nm.

4.3 3D numerical simulations

The study of the interaction of the optical field with sub-wavelength structured materials is, in general, a complicated task. In the case of scanning probe optical microscope, main difficulties arise from the study of the interaction of the nano-sized probe with optical waves. In this domain, main attention is payed to the research of optimum fabrication designs and processes which would eventually improve the resolution and the transmission properties of a scanning probe. In this sense, the possibility to construct computational models for the investigated structures represents a very useful and versatile tool. Many parameters, like geometrical properties or dielectric constants (i.e. material choice), can be easily modified in the modeled structure, and the device response can be investigated without involving any real fabrication process or experimentation.
In this section we present a 3D computational model for the propagation simulation of electromagnetic modes in the investigated aperture-less scanning probe. The model has been developed with the help of a commercial software (Microwave Studio, CST, Darmstadt, Germany) which uses a Finite Difference Time Domain (FDTD) algorithm. The main goal of the numerical sim-

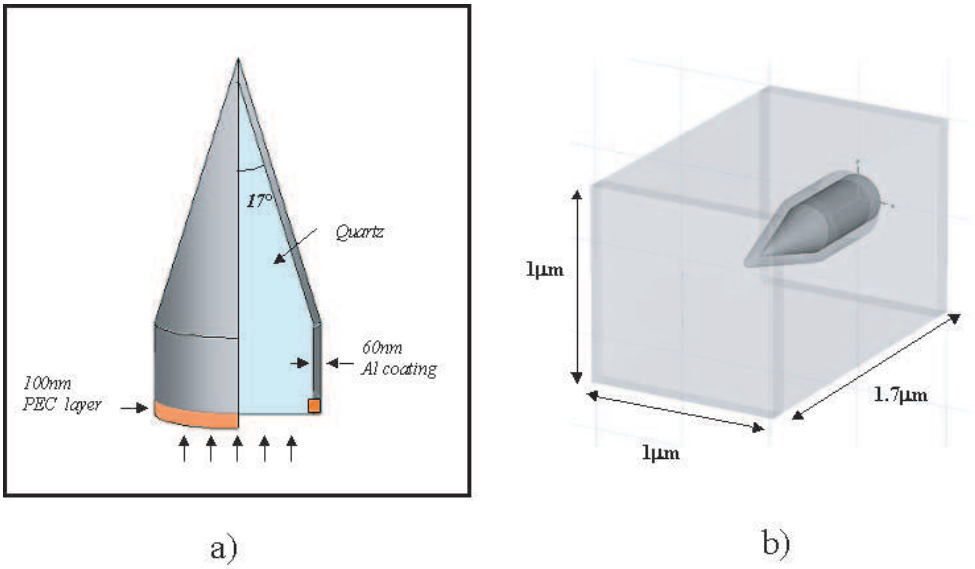

Figure 4.1: *(a) Three dimensional model of the fully-coated quartz SNOM probe. The apex angle of the tip is* 34^o*, the Aluminum coating thickness is 60 nm and the cylindrical waveguide has a cross-sectional diameter of 250 nm. (b) The modeled domain is a 3D rectangular air box surrounding the probe.*

ulation is to individuate a set of modes whose characteristics would optimize the transmission and the lateral resolution of the probe. For this purpose, the probe is modeled as displayed in Fig.4.1(a). In the beginning, the structure is composed of a 500nm long cylindrical waveguide with a quartz core of 250 nm in diameter. The core is coated with a 60 nm Aluminum cladding. The tapered region is modeled by a conical part with a cone angle of 34^o. The cone apex is rounded with a final radius of 30 nm. This design has been chosen in order to match as much as possible a realistic structure. The tapered region is also composed by a quartz core coated by a 60nm Aluminum layer. Because we are interested in studying not only propagation of light inside the probe, but also the throughput field from the probe, the computed domain is extended to a 3D rectangular air box of $1\mu m \times 1\mu m \times 1.7\ \mu m$ which surrounds the entire struc-

ture (see Fig.4.1(b)). Calculations are performed at the optical frequency $\omega = 3.543{\cdot}10^{15}s^{-1}$ ($\lambda = 532nm$).
The entrance of the cylindrical part of the probe lays on the input facet of the investigated volume. This facet is constituted by a 100nm layer of Perfectly Electric Conducting (PEC). In the beginning, then, the PEC layer surrounds the core of the cylindrical section of the probe.
The computational procedure consists of two steps. First, we calculate the eigenmodes supported by the probe region surrounded by PEC. The presence of the PEC layer has two main advantages. The first is that it avoids leakage from the input facet. This light would actually propagate in the air volume and, eventually, superpose to the light emitted by the probe, generating, optical patterns of difficult interpretation. Secondly, because of the PEC layer, the initial part of the cylindrical section behaves like a loss-less metallic waveguide. The modes supported by a similar structure are well known and classified as transverse magnetic (TM) and transverse electric (TE). The calculation leads in general to several eigenmodes. Therefore, the second step consist in selecting modes of major interest and running their propagation through the modeled domain.
As mentioned in the previous section, there are two modes of particular interest on which we will focus our attention: the linearly polarized TE_{11} mode, and the radially polarized TM_{01} mode.

4.3.1 TE_{11} mode

The lowest order eigenmodes calculated at the entrance of the simulated structure correspond to the two orthogonal modes TE_{11}. The corresponding field distributions are identical and transform one into each other after a rotation of 90°. In Fig.4.2, it is displayed the case in which the field is mostly polarized along the $\hat{x}$ axis of the transverse plane. Because the linear polarization cannot match exactly the symmetry of the waveguide, we observe the appearance of a weak field component, along the y-direction, mainly concentrated on the borders. The graphs are normalized to the maximum value of the total amplitude $\sqrt{|E_x(x,y)|^2 + |E_y(x,y)|^2}$. As soon as the mode TE_{11} enters the tapered region, its propagation continues in the form of

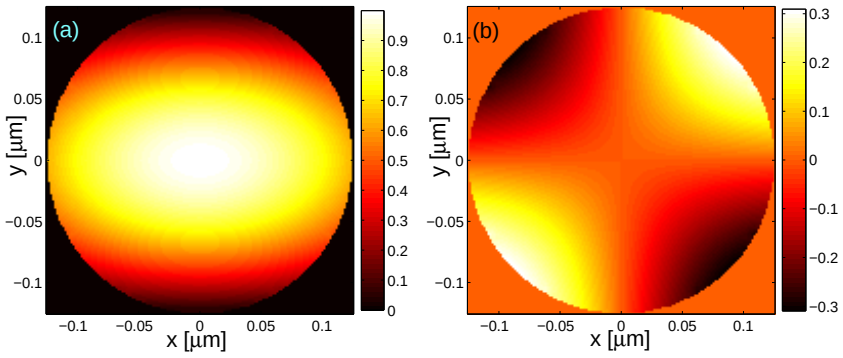

Figure 4.2: *Real part of the normalized electric field associated to a TE_{11} mode at the entrance of the loss-free metallic waveguide: (a) $Re\{E_x\}$ and (b) $Re\{E_y\}$*

the hybrid mode HE_{11}. In section 4.2, we have introduced the different phases and mechanisms which are experienced by the mode during its propagation in the conical region of a metalized probe. In particular, we have seen that this mode presents a radius cutoff value which allows a ratio of the energy to be transmitted as far as the probe apex and eventually transmitted through the thin Aluminum layer. As the experimental part of this work is conducted with

a canonical microscope, which cannot image the near-field of the probe apex, we are mostly interested in studying the optical patterns calculated at some hundreds of nanometers from the probe apex. An analysis of the near-field throughput associated to the mode HE_{11} was recently reported by Vaccaro *et al.* [44]. In this paper, it is shown that the near-field distribution, at a few nanometers from the probe apex, is characterized by two linearly polarized lobes oriented along the direction of polarization. A very weak filed is instead located above the probe apex. This result seems to correspond well with the propagation mechanism suggested in [62]. The two lobes are then the result of the coupling of the propagating HE_{11} mode with the corresponding HE_1 surface mode, which propagates till the probe apex.

In Fig.4.3, we report the field distribution and the phase patterns calculated at 250 nm from the

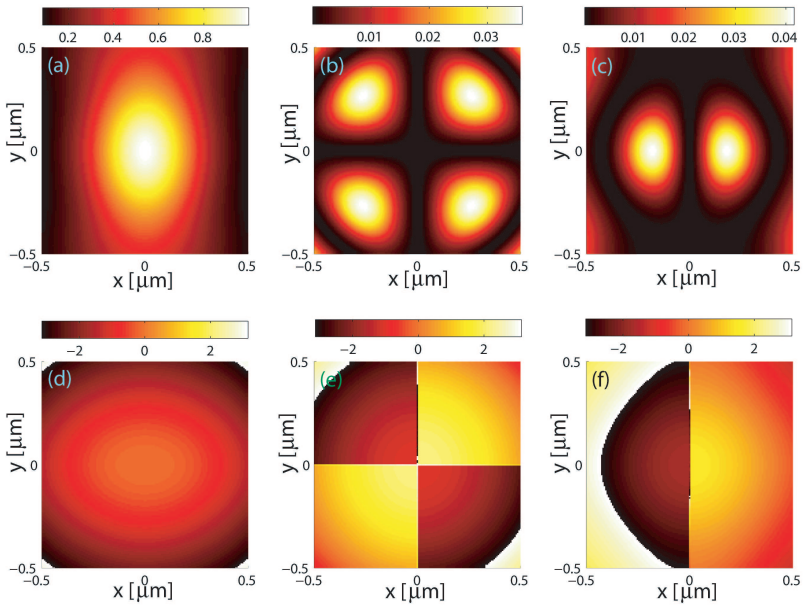

Figure 4.3: *Tip emission of the HE_{11} mode in a transverse plane 250 nm from the tip apex: (a,b,c) amplitude and (d,e,f) phase distributions of the E_x, E_y and E_z electric field components respectively.*

tip apex. We can observe that the field components evolution, at this plane, presents interesting characteristics. The plots are also in this case normalized to the maximum value of the total electric field amplitude $\sqrt{|E_x(x,y)|^2 + |E_y(x,y)|^2 + |E_z(x,y)|^2}$. Firstly, we find that most of the energy is concentrated in the component E_x. This means that the throughput is mostly linearly polarized and that the resulting polarization coincides with the input polarization. The phase map shows a parabolic profile which is due to the divergence of the propagating beam. The field component E_y is characterized by a four-lobe distribution. The phase map shows a jump of π between two adjacent lobes and is also characterized by a slight parabolic profile. This depolarization effect, due to the propagation of a linearly polarized beam across the probe, has already been reported experimentally in [55]. The field distribution is also characterized by a weak longitudinal component characterized by two lobes aligned along the x-direction. The limited domain in our calculation does not allow to determine a farther evolution of such a component, however we suppose it disappears in the transition from the near- to the far-field, where the field becomes paraxial.

4.3.2 TM_{01} mode

The second mode of particular interest is the radially polarized mode TM_{01}. The relative eigenmode distribution at the input plane is shown in Fig.4.4. Note that in this case most of the field

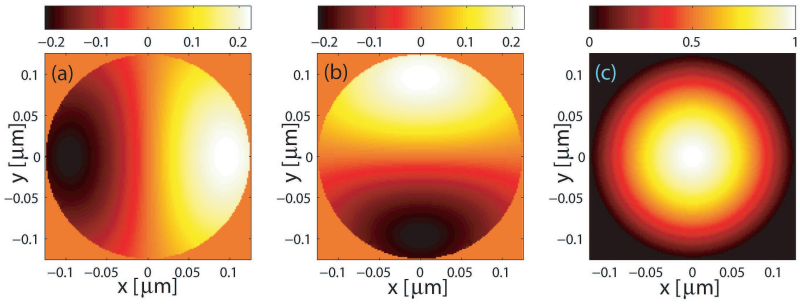

Figure 4.4: *Real part of the normalized electric field associated to a TM_{01} mode at the entrance of the loss-free metallic waveguide: (a) $Re\{E_x\}$, (b) $Re\{E_y\}$ and (c) $Re\{E_z\}$.*

is concentrated in a longitudinally polarized spot. Components E_x and E_y are mostly concentrated on the borders and the sum of their intensities generates a ring surrounding the central longitudinal spot. It is worth, in this case, to analyze also the throughput field distribution in proximity of the probe apex. In Fig.4.5 are plotted the square amplitudes of the three field components computed in a plane placed at 10 nm from the probe apex. Also in this plane all three field components appear. It is interesting to note that we find again a field distribution comparable with the one in input. Actually, the intensities associated to the transverse components form a ring which surrounds a more intense longitudinal spot. The lateral extension of such a spot (Fig.4.5(c)) is ∼40 nm. It is worth to note that this size is smaller than the

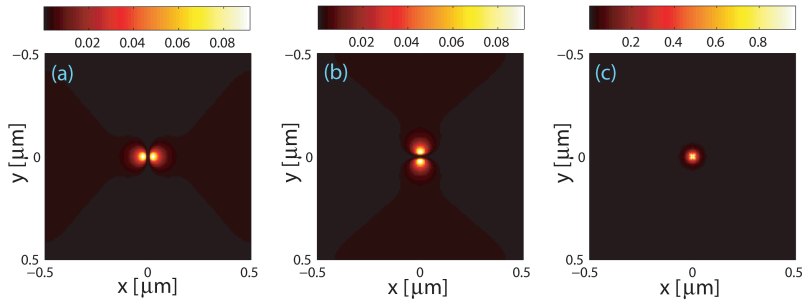

Figure 4.5: *Tip emission of the TM_{01} mode: normalized squared amplitude distributions of the electric field cartesian components in a transverse plane at 10 nm from the tip apex. (a) $|E_x|^2$, (b) $|E_y|^2$ and (c) $|E_z|^2$.*

metallic apex of the modeled probe ($\sim 60nm$). In fact, it is widely accepted that the lateral resolution of a scanning probe coincides with the radius of curvature of the tip apex, in the case of uncoated tapered fibers, or with the aperture radius in case of metalized tapered fiber probes. The reported results show that the use of aperture-less scanning probes, combined with

a radially polarized illumination source, allows to improve the lateral resolution beyond the limits imposed by the probe geometry. In a typical scanning near-field experiment, the probe is scanned at few nanometers from the sample surface. The intense near-field longitudinal spot reported in Fig.4.5(c), would act like a nano-source able to illuminate the sample surface with a sub-wavelength resolution, which in our case would correspond to $\sim \lambda/13$.
In Fig.4.6 are displayed the distributions of the field components, together with the corresponding phase maps, in a plane at 250 nm from the tip apex. It is possible to notice that the longitudinal component remains prevalent. However, a bigger ratio of the total energy has been transferred from the longitudinal component to the transverse components E_x and E_y. A slight wavefront divergence is observable in the phase map associated to the transverse components. As mentioned above, the modeled domain is too small to enable the plotting of the far-field

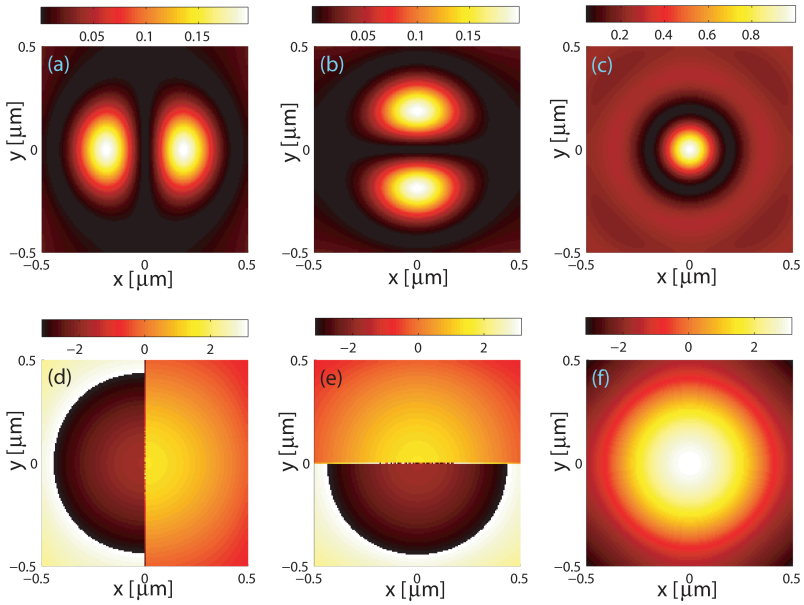

Figure 4.6: *Tip emission of the TM_{01}^{x} mode in a transverse plane at 250 nm from the tip apex: (a,b,c) amplitude and phase (d,e,f) distributions of the E_x, E_y and E_z electric field components respectively.*

evolution. However, as light propagating in the far-field has mostly paraxial characteristics (i.e., transverse filed distributions), we assume that the longitudinal component would eventually disappear at some λ from the probe apex. The resulting far-field should present an annular distribution due to the sum of the transverse component intensities. This conclusion is in agreement with numerical results reported in [44].

4.4 Experimental set-up

In the previous sections, we have presented a 3D numerical analysis of the electromagnetic properties of light propagating into an apertureless scanning probe. The FDTD algorithm is based on the decomposition of the investigated domain in several unit cells. The solution of the Maxwell's equations leads to constant values of the electric and magnetic field in each unit cell. This means that the accuracy, with which the field configuration of the investigated domain can

be determined, depends on the number of cells in which the domain has been decomposed. This is a critical aspect of numerical simulations. Actually, the higher the number of cells, the longer the time needed to calculate the fields in the entire volume. The best strategy, in this case, is to reduce the investigation to those critical features of the structure which can be of particular interest. By reducing the volume of investigation, it is possible to increase in a reasonable way the number of unit cells. In the case of the apertureless probe the most critical part is the tapered region. The study of the transmission properties of scanning probes, limited only to the tapered region, has been already attempted in previously cited publications [30, 44, 62, 64]. Because limitations in the computational power impose some compromise in the choice of the modeled structures, one can wonder how reliable and consistent can be the numerical results with the real behavior of a realistic sample.
In this section we try to answer this question for the case of a fully metalzed microfabricated cantilevered probe. The analysis is conducted by means of a Mach-Zehnder interferometer mounted on a high-magnification optical microscope. Both information on intensity and phase distributions are obtained by exploiting the interferometric technique. We have seen, in section 4.3.2, that at some microns from the probe apex, the field is definitely not paraxial. As the images recorded with the present set-up belong to plane placed at a few microns from the probe apex, we will refer to this region like an intermediate-field.
The phase information contained in the emitted patterns gives us a direct insight on the coupling mechanism between the optical field injected into the probe and the modes excited in the structure. Moreover, in this section, we will show that HE_{11} and TM_{01} modes can be selectively coupled into the probe by injecting focused beam having suitable polarization states.

4.4.1 High Resolution Interference Microscope

The Mach-Zehnder interference microscope used for intensity and phase characterization of the optical fields emitted by the apertureless probe is depicted in Fig.4.7.

The reference and the signal beams are obtained by splitting the light of a linearly polarized He-Ne laser at 633 nm. A system composed of a half wave plate (HWP) and a polarizing beam splitter (PBS), placed at the laser exit, enables a control of the light power sent in the interfering beams. In order to obtain a good quality interferogram, contrast in the fringes system must be as high and uniform as possible. Contrast can be tuned with the help of a pair of polarizers put in front of the HWP. Both reference and object beams are injected in polarization maintaining fibers in order to preserve the polarization orientation and maximize the interference quality. The signal beam is then expandend and sent through a series of Liquid Crystal (LC) elements. With the LC device, a radially polarized beams can be generated. Light injection into the probe is performed by focusing the object beam onto the back-side opening of the probe by means of a NA=0.4 microscope objective mounted on a xyz translation stage. Light emitted at the apex of the SNOM probes is collected by a micro-objective (x50).

Th adjustable 45° mirror in the object arm is mounted on a PZT driver enabling phase shifting interferometry. For this purpose the CCD camera has a pixel synchronous frame grabber coupled to a Personal Computer (PC). The phase calculation algorithm implemented in the acquisition software (PSI, Erlangen-Nürnberg University) exploits a dynamic technique fringes analysis [66]. The relative phase between the reference and the signal beam is varied in a sequence of five constant steps by moving the PZT mirror. At each step, the PC records the intensity signal of the interferogram. The phase map is finally calculated from these five recorded images.
Recombination of reference and object beam is performed by means of a second BS. The super-

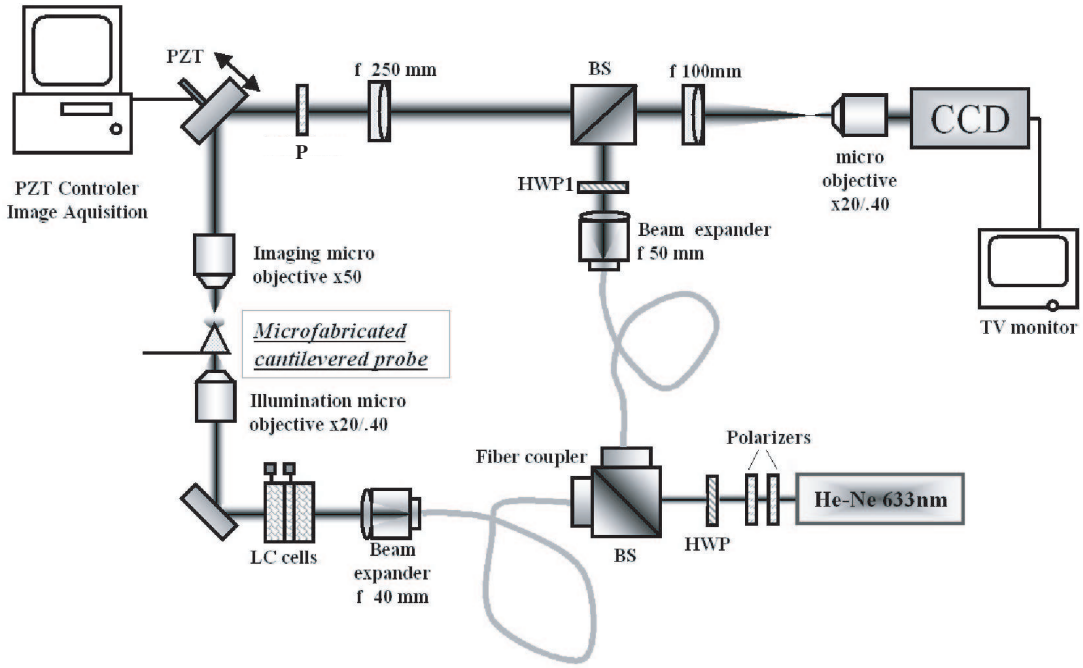

Figure 4.7: *Schematic of the high-resolution interference microscope based on a Mach-Zehnder used for the phase characterization of optical field emitted by apertureless probes.*

posed beams are then collected by a telescopic system providing a further magnification of the interferogram.

4.4.2 Liquid Crystal elements

The Liquid Crystal device employed in the experiment is used for the generation of a radially polarized beam [56]. As displayed in Fig. 4.8 it is composed of three elements: a θ-cell, a π-phase shifter and a polarization rotator. The θ-cell, proposed by Stalder and Schadt [67], provides an axially symmetric arrangement of the polarization vector. Depending on the polarization of the input beam, a radial or an azimuthal distribution are carried out [56]. Since we are interested in the generation of a radially polarized beam a linearly, y-polarized beam should be used as input field. In order to have a fully radially polarized beam, the y component of the output field must present a π phase difference between the upper and the lower half of the beam. The θ-cell alone does not provide such a phase difference, therefore a second LC element is added to the setup. The π-shift plate introduces a voltage controlled phase retardation in one of the two halves of the beam. A calibration of the π-shift plate is, then, necessary in order to find the right voltage corresponding to a phase retardation of π. A third LC element, the *polarization rotator* cell, is finally introduced between the π-phase shifter and the θ-cell. If voltage (10V at $\nu = 1$ KHz) is applied to the *polarization rotator* cell, then the polarization state of the output light is unchanged, but if no voltage is applied, the cell behaves like a $\lambda/2$ plate rotating the polarization by 90°. With this arrangement, we can use a linearly x-polarized beam as input field and obtain a radially polarized field as depicted in Fig. 4.8. With the help of the polarization rotator, it is possible to electrically switch between azimuthally and radially polarized output beams without moving any optical elements. Even if not used in this experiment, this feature is rather interesting because it avoids the risk of introducing malicious misalignments in

the optical setup. All the three LC elements are brought together into a single compact device and mounted on a moving stage allowing transverse displacement with respect to the beam.

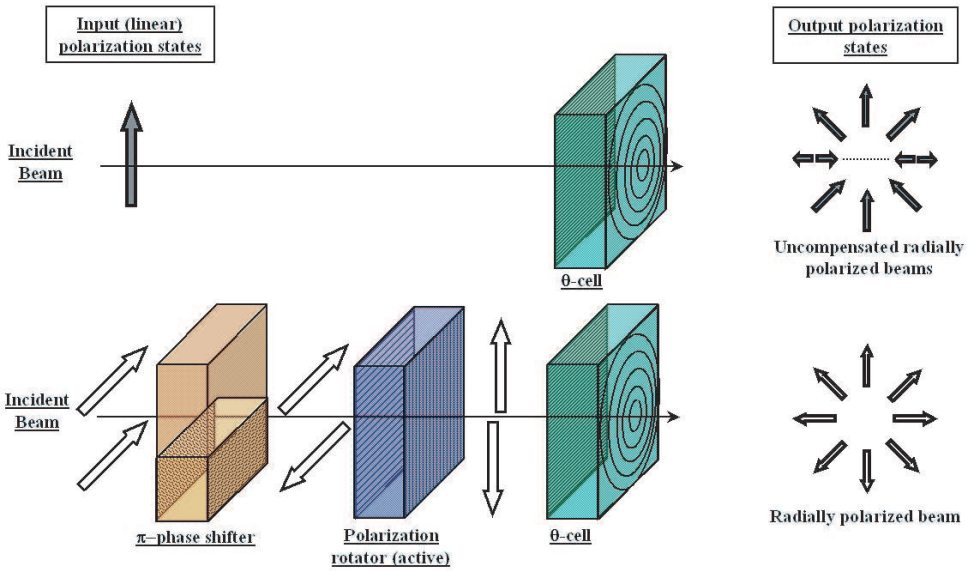

Figure 4.8: *Liquid Crystal elements system employed for the generation of radially polarized beams.*

4.5 Intermediate-field measurements

The investigated sample is a standard micro-fabrictaed SNOM probe [55]. The tip is integrated at the edge of a silicon cantilever. The tip core structure is made of SiO2 and has a conical shape of 12 μm in height. Figs. 4.9 report a SEM image of the whole structure together with a TEM image of the very apex of the tip. A 60nm layer of Aluminium covers completely both the glass cone and the cantilever. Light is injected from the back side. For this purpose a square hole, $6\mu m \times 6\mu m$, is etched on the reverse side of the cantilever at the tip location.

We have seen in the theoretical sections of this chapter that, once the eigenmodes have been calculated at the entrance of the metallic probe, one can selectively propagate them in to the entire structure. From the experimental point of view, this procedure is obviously impossible. Two main difficulties arise when one attempts to inject light into the cantilevered probe. Firstly, the real input aperture has a large size of about $6\mu m$. This means that, at least in the beginning, the structure behaves like a multimodal waveguide. We can, then, imagine that light propagates in the form of a superposition of several modes of different orders. Secondly, even though, according to what discussed so far, only a few modes can propagate till the very end of the probe, the energy stocked in the remaining modes is not lost. Therefore, when a mode runs into cutoff, the associated light is either reflected back or expelled, through the thin metal coating, from the the side of the taper. The throughput field will be, in general, the superposition of guided, reflected and leaked light. The discrimination of a particular pattern associated to a single mode is, therefore, a very task . For this reason, it is a crucial issue to be able to experimentally select those injection configurations enable the selection of a limited, and possibly well known, number of modes. Of course, the choice falls upon those modes that are more likely to produce the highest and most localized throughput at the very end of the tip.

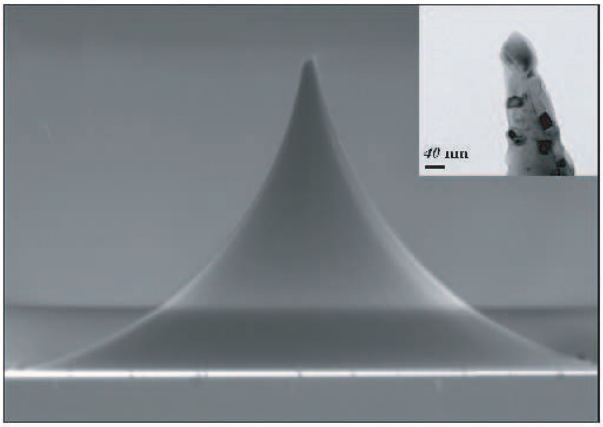

Figure 4.9: *SEM image of the investigated cantilevered probe and TEM image of the very tip apex (inset).*

4.5.1 Coupling of the HE_{11} mode

As mentioned in the previous sections, a number of published works have demonstrated that the coupling of HE_{11} mode in metalized tapered fibers provides the largest optical power throughput. This mode is prevalently characteristic of a linear polarization, therefore, it is quite intuitive to try to excite it by focussing a linearly (let us say parallel to the x-direction) polarized beam at the input base of the tip. The numerical analysis can be exploited in order to choose an injection condition as close as possible to the selected eignemode distribution. In this sense, we find a favorable circumstance in focussing a linearly polarized beam by means of a microscope objective. A numerical analysis of the focal field component distributions has been reported by Lieb and *et al.* in 2001 [68]. It is shown, in the case of linearly polarized light, that the focussing of light towards the focal plane gives rise to a field distribution in which both transverse and longitudinal components appear. In particular, the x-component is characterized by a bright elliptical spot, while the y-component presents a weaker four-lobed distribution. The four lobes are characterized by a π phase jump between to adjacent lobes. The z-component is characteristic of two lobes, oriented along the x-direction. With the exception of the longitudinal component, the transverse field matches quite well, both in terms of intensity ratios and phase distribution, the one obtained for the eigenmode TE_{11} reported in Fig.4.2. As a first selecting procedure, then, we focussed a linearly polarized beam at the entrance of the micro-fabricated probe. In Fig.4.10 we report intensity and phase maps recorded with the Mach-Zehnder microscope at an intermediate-field plane above the probe apex. We find that two different patterns, having orthogonal polarizations, are imaged at the probe exit. A bright spot polarized in the x-direction (the same polarization of the injected beam) is superposed to a less intense four-lobe pattern, y-polarized. The intensity patterns are recorded by shuttering the reference beam and by selecting one pattern at time by means of the polarizer in the interferometer object arm. The observed distribution are comparable, for both components, with the corresponding ones in Fig.4.3. On the contrary, the measurement of the phase maps requires the recording of the interferogram. In order to obtain optimum contrast, the polarization of the reference beam is rotated according to the polarizations of the two intensity distributions. The rotation is enabled by the HWP placed in the reference arm.
In Fig.4.10(b), we observe that the phase map of the spot is well defined only over a rather small

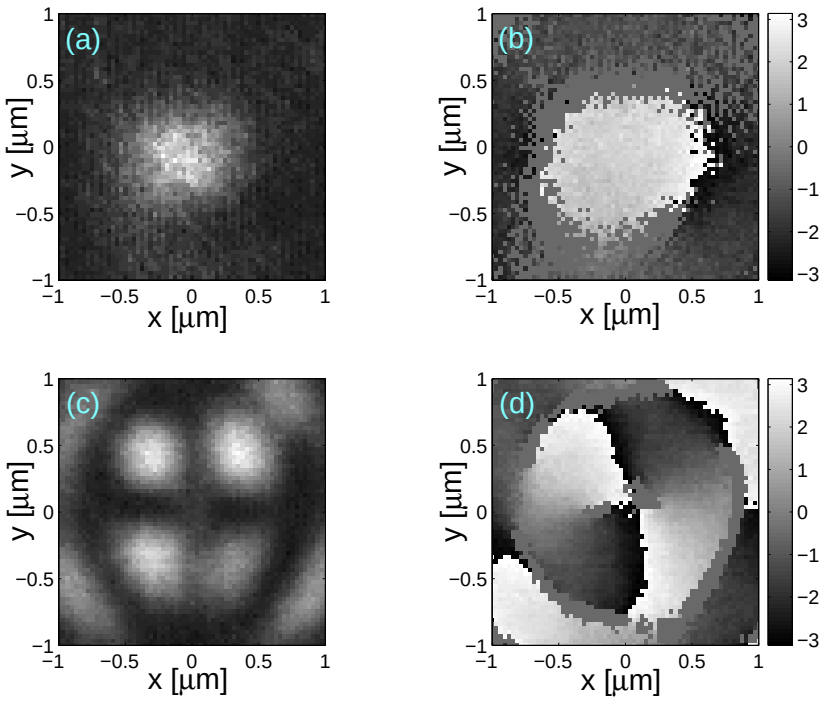

Figure 4.10: *Far-field emission pattern of microfabricated fully metal-coated probe after injection of a focused linearly polarized beam. Intensity distributions recorded for components x (a) and y (c). The corresponding phase maps are reported in (b) and (d) respectively.*

area. This effect is due to the fact that most of the spot light is prevalently concentrated in the middle of the recording surface. The contrast with the reference plane wave is consequently deteriorated at the border region. Nevertheless, the phase distribution and the calculated one in Fig.4.3(d) show a good agreement. Similarly, for the y-component, we measure a phase pattern comparable with the numerical one showed in Fig.4.3(e). The edge dislocations between two adjacent lobes are particularly well defined.

4.5.2 Coupling of the TM_{01} mode

In [68], it is also reported the focal plane field distribution corresponding to the focussing of a radially polarized beam by means of microscope objective. Similarly to the case of the TE_{11} eigenmode, such field distribution matches quite well the characteristics of the calculated eigenmode in Fig.4.4. We, then, attempt to operate the selection by focussing the radially polarized beam generated by the LC element. The quality of the axially symmetric polarized beam has to be verified before injecting light in the probe. We did it by removing the sample and detecting the optical pattern produced in the focal plane of the illuminating objective. The pattern is characterized by a doughnut which presents in the middle a zero value of the field intensity and a phase singularity. For both polarizations, if the polarizer P is interposed between the imaging objective and the CCD camera, the recorded pattern is composed of two lobes characterized by a mutual π-phase jump across the singularity location. The lobes are distributed on a line parallel to the axis of the polarizer. To a rotation of a positive angle of the polarizer , it corresponds a positive rotation of the lobes of the same angle. Good quality axial symmetric beams have been obtained when this effect is always observable by rotating the polarizer from 0^o to 180^o.The

injection of a focused radially polarized beam is highly sensitive to misalignments. The most delicate step consists of bringing the optical axis of the focusing system as close as possible to the probe axis: if the focused beam has not a fully circular symmetry at injection, the dominant linear field component will couple to other modes in a non controlled way.

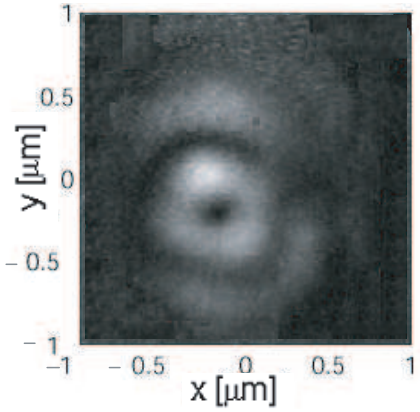

Figure 4.11: *Far-field emission pattern of microfabricated fully metal-coated probe after injection of a focused linearly polarized beam. Intensity and phase distribution of (a,b) x component and (c,d) y component of the optical field respectively.*

An example of the characteristic intensity pattern is reported in Fig.4.11. The measurement was obtained by screening the reference beam.
According to simulations reported in section 4.3.2, the field distribution, at some microns above the probe apex, should be characterized by a radially polarized annular distribution. This condition can be proven by a series of measurement. With the help of the polarizer P, it is possible to select alternatively the x and the y components. Optimum contrast in the interferogram is obtained by opportunely rotating the reference beam polarization. Recorded measurements are reported in Fig. 4.12. When the polarizer is oriented parallel to the x-direction (Fig. 4.12(a)), the interferogram is characterized by two lobes oriented parallel to the field polarization. The corresponding phase distribution is characterized by a π-phase across the central singularity. Similar patterns are recorded, both in intensity and in phase, for the y-component after rotating polarizer and reference beam by 90^o. A definitive verification of the polarization state can be performed by removing the polarizer P. In this case, the reference beam interferes with only one component at time. The resulting interferogram and phase patterns are reported in Fig.4.13 for the case in which the reference beam is polarized along the y-direction. It is interesting to notice that the phase pattern is well defined only along the y-axis. Along the x-direction it is possible to observe two lobes, just beside the central singularity, in which the phase is not defined. Actually, at these locations reference and object beams are orthogonally polarized, any interference can occur and the retrieval algorithm fails in determining the corresponding phase distribution.
The recorded intensity patterns correspond quite well to the ones expected from numerical simulations in planes far from the probe apex. This results suggest that, in the near-field of the probe, a longitudinally polarized super-resolving spot is actually generated.

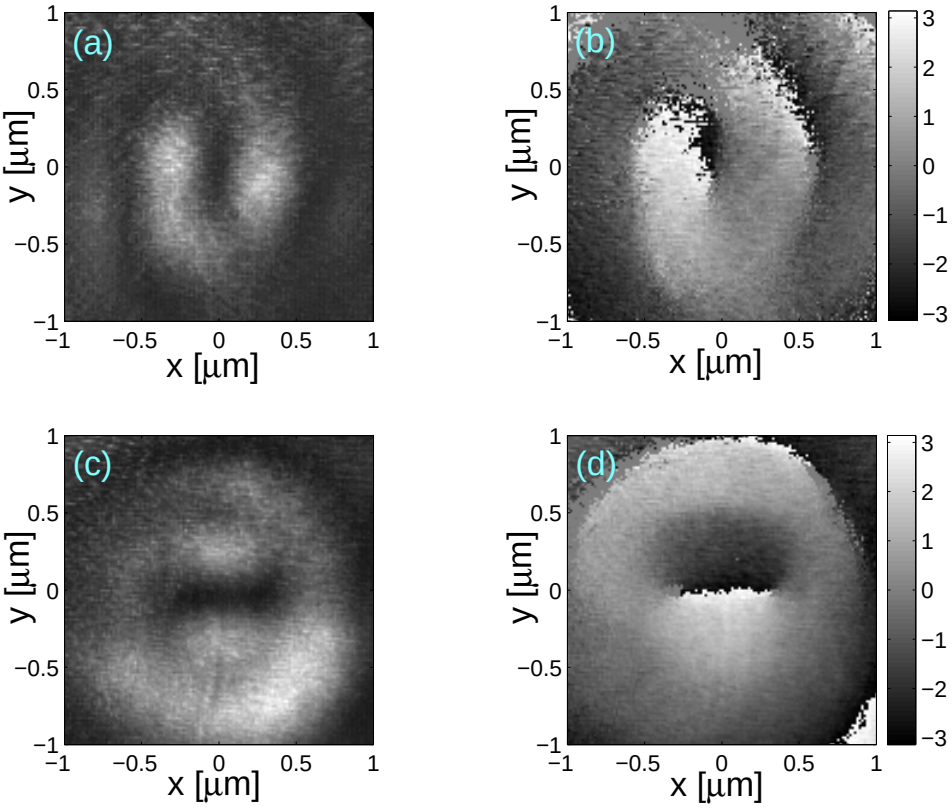

Figure 4.12: *Far-field emission pattern of microfabricated fully metal-coated probe after injection of a focused radially polarized beam. Intensity and phase distribution of (a,b) x component and (c,d) y component of the optical field respectively.*

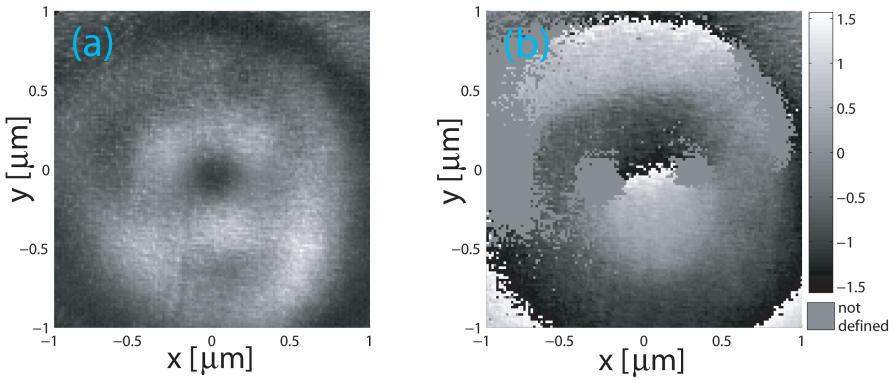

Figure 4.13: *Intensity throughput pattern generated in the far-field of the meatl-coated probe after injection of a longitudinally polarized beam. The intensity pattern is recorded by shuttering the reference beam in the Mach-Zehdher microscope.*

4.6 Conclusions

The guiding properties of microfabricated, fully metal-coated quartz probes have been theoretically and experimentally investigated. A 3D computational model of the probe has been

presented. The model enables the investigation of both light propagating in the structure and the corresponding probe throughput. The numerical analysis allowed to individuate two modes of particular interest: the fundamental linearly polarized HE_{11} mode and the radially polarized TM_{01} mode. We have discussed the the different mechanisms that allow to guide these modes as far as the probe apex. In particular, the transmission of the TM_{01} mode gives rise in the near field of the probe to a longitudinally polarized hot-spot whose lateral dimensions are smaller than the probe apex. This result opens the perspective to use this polarization to improve the lateral resolution of the probe in scanning near-field optical experiments. On the basis of the numerical results, we have individuated experimental techniques for the selective injection of the HE_{11} and the TM_{01} mode. The reliability of the techniques has been verified by imaging the probe throughput for each injection configuration by means of a Mach-Zehnder interference microscope. The interferometric set-up allowed to record simultaneously intensity and phase patterns of the imaged fields. We have imaged optical patterns at a few microns above the probe apex. The comparison of the experimental results with the calculated optical patterns demonstrate the effectiveness of the proposed techniques. In particular, the experimental results demonstrate that a superresolving longitudinally polarized spot is actually produced at the probe apex when a radially polarized mode is selectively injected.

Chapter 5

Observation of amplitude and phase in ridge and photonic crystal waveguides operating at $1.55\mu m$ using heterodyne scanning near-field optical microscopy

5.1 Introduction

Photonic crystals (PhC) are a new class of materials whose electromagnetic properties allow confinement, guiding and molding of light [77]. The structure of a photonic device affects the photon properties as the atomic lattice of ordinary semiconductor crystals affects the electron properties. This analogy was first suggested by Yablonovitch and John in 1987 [81, 82]. In the case of a PhC, the atomic lattice is substituted by a periodic array of macroscopic dielectric elements. In a similar crystal, the photonic states are described in terms of band structures as in the case of electrons [75]. Analogously to the case of semiconductor electronic bands, PhC crystal can be projected in such a way to open complete forbidden band gaps in the photonic band structure. Hence, for some range of optical frequencies light propagation in the device is forbidden. The introduction of defects in the crystal gives rise to localized photonic states in the forbidden gap. The shape and the properties of such states depend on the nature of the defect. This means that, by changing the value of the dielectric constants (i.e., materials) and the shape of the defects, a photonic structure can be forced to select any desired range of wavelengths. The nature of the defect influences also the symmetry of the photonic states and, then, the characteristics of the confined electromagnetic modes. From a numerical point of view, PhCs are ideal materials. Actually, Maxwell's equations can be solved in the modeled structure with any desired degree of accuracy. The numerical approach consists in casting Maxwell's equations in a form comparable to Schrdinger's equations. In this way, the techniques used to study the electron properties in solids can be also applied to the study of photonic states in the PhC [83, 84]. The additional advantage in dealing with photons is that, contrarily to electrons, they are non-interacting particles. Therefore, equation solutions do not rely on approximations and the numerical problem can be solved exactly.
The properties mentioned above open wide perspectives in the application of photonic structures to ligthwave systems [85].

In this chapter, we present an investigation of the optical properties of photonic crystal waveguides, designed to work in a range of wavelength around $1.55\mu m$, by means of a heterodyne scanning near-field optical microscope. We investigated a standard air-bridge waveguide, a straight PhC waveguide and a corner PhC waveguide. All the structures are produced from Silicon-on-Insulator (SOI) wafers [86].
Contrarily to the most common used far-field investigation, SNOM measurements allow to visualize directly the propagation characteristics of the electromagnetic modes supported by the PhC waveguide [87–91]. The additional information on the phase, provided by the heterodyne signal, enables the experimental determination of the complex amplitude of the investigated fields. A Fourier analysis of the data provides useful information on parameters like the effective wavelength (i.e., the propagation constant) and the effective refractive index for the modes supported by the waveguide.

5.2 Experimental set-up

A schematic diagram of the heterodyne SNOM, optimized for the investigation of the optical properties of photonic structures, is reported in Fig. 5.1. The present system is completely fibred. The laser source is a tunable (CW) laser operating in the range of wavelengths 1.520-1.570μm with a minimum step of 0.1 nm (*New Focus, Model 6247*). The source has an initial power of 1 mW, and is subsequently amplified by means of an Erbium-doped Fiber Amplifier (EDFA) till a final power of 40mW. The light is directly injected in a single mode fiber and the splitting of the reference and the object beam is operated by means of a fiber coupler. The frequency shift, enabling the heterodyne detection, is operated on the reference channel by means of two acoustooptic modulators (AOM). The AOM are driven at 40.07 and 40.00 MHz, generating a heterodyne frequency modulation of 70 kHz. The signal channel is provided with a polarization controller which enables the selection of TE and TM polarized light. The scanning microscope is the model AFM/SNOM MultiView 2000 produced by Nanonics Imaging Ltd. (Israel). This innovative instrument is provided with two sets of three-axis computer-controlled translation stages for independent positioning of the specimen and the probe. This property revealed itself to be very useful during the experiment. By means of the bottom scanner one can move, with nanometric precision, the sample with respect to the injection system. Once the optimum injection has been obtained, one can move the tip above the area of interest and scanning it with the independent upper scanner. Beside this advantage, there is the inconvenience that the distance between the two scanners is reduced to a little more than one centimeter. Therefore, the injection cannot be performed by focussing the light with conventional micro-objectives, which are generally embedded in larger holders. Therefore, we adopted an injection system composed of a fiber collimator and a cylindrical microlens that was suited to be inserted between the scanner surfaces. The upper scanner has an annular shape with the probe placed in the middle. This condition allows to observe the sample surface from atop by means of a long working distance microscope. The microscope is provided with an infrared CCD camera which simultaneously enables to monitor the injection quality. The scanning probe is a bent metalized tapered fiber with an aperture of 200nm in diameter. In the range of the investigated optical frequencies, such diameter provides a sub-wavelength resolution both for the light propagation in free space and in the bulk silicon. The probe is glued on one prong of a quartz tuning fork which is vibrated at the resonance frequency and that provides the current signal for the closed-loop adjustment of the tip-sample separation. Since the fork is oriented with its prongs parallel to the sample surface, the vibration occurs in the vertical direction. The SNOM is therefore operated in tapping-mode. This technique particularly indicated for imaging delicate and fragile samples in

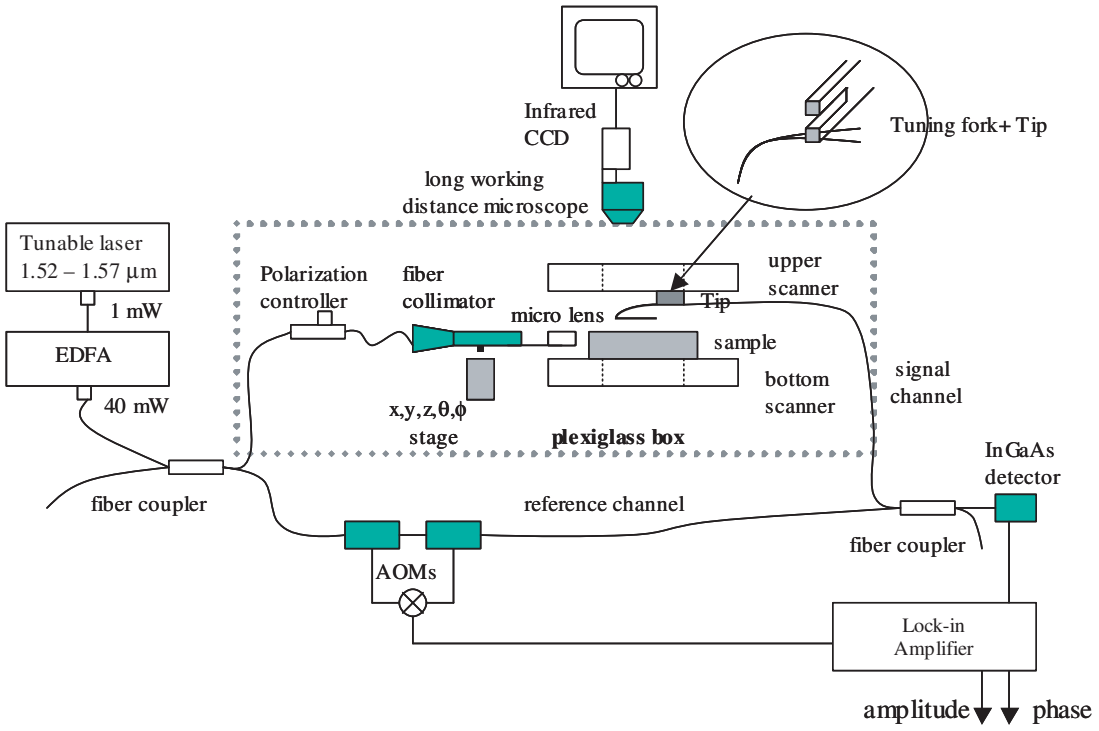

Figure 5.1: *H-SNOM set-up optimized for the investigation of the optical properties of photonic crystal waveguides.*

biology and polymer materials [70]. In fact, compared with a shear-force operating system [71], the intermittent interaction reduces the friction effects between sample surface and probe. In this experiment, the probe is scanned above very thin suspended membranes. Therefore, the tapping mode technique results the more appropriated.
The SNOM head with the injection system are embedded in a plexiglass box to screen from the environmental noise the free propagating light at the injection location. The heterodyne signal is detected by means of an InGaAs detector. The lock-in output channels provide the acquisition program (*Quartz for NSOM, Cavendish Instruments Ltd*) with the optical amplitude and phase signal, while the topography is recorded through the closed-loop position adjustment, which is operated in constant force mode. During a scan process, the software records simultaneously topography, force, amplitude and phase maps.

5.3 Air-bridge waveguide

The first investigated sample is a standard ridge waveguide. This device is fabricated using an Silicon On Insulator (SOI) wafer, with an approximately 290 nm thick silicon guiding layer and $1\mu m$ thick oxide layer. The oxide separation layer under the thin central section of the waveguide is undercut, resulting in an air-bridge structure. A SEM image of the air bridge region is reported in Fig.5.2(a). The input and output structure are identical and are fabricated as displayed in Fig.5.2(b). The initial part of the structure has a width of $10\mu m$. Subsequently the waveguide tapers little by little till reaching the width of 500 nm at the entrance of the air-bridge. The efficiency of this injection technique has been demonstrated by Märki *et al.* in 2004. The output

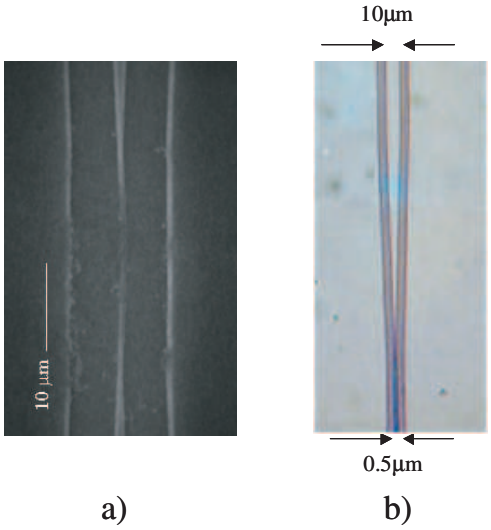

Figure 5.2: *(a) SEM image of the Air-Bridge waveguide. (b) Magnified image of the input injection structure.*

structure is similar, so that the injection can be operated on both sides of the device. A similar structure can guide both TE and TM polarized light. The experiment discussed in this section is conducted by injecting TM polarized light into the waveguide at a wavelength of $1,55\mu m$. In

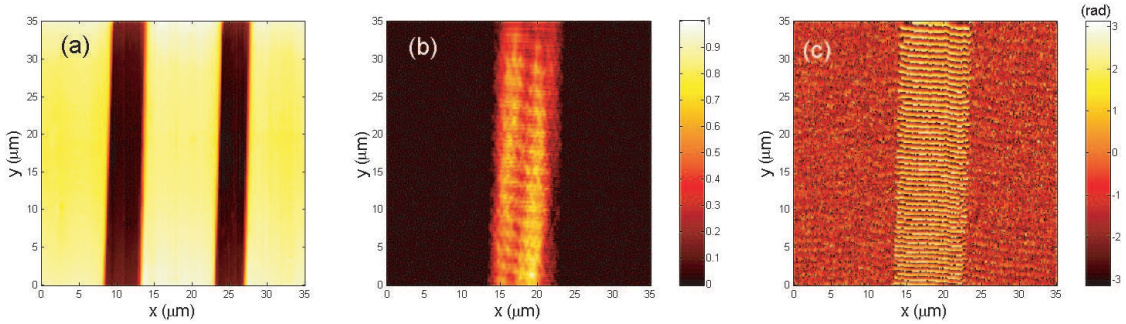

Figure 5.3: *(a)Topography, (b) amplitude and (c) phase maps simultaneously recorded over the wide part of the waveguide. The amplitude map is normalized to the maximum value of the detected optical signal.*

this case the electric field is oriented orthogonally with respect to the surface of the waveguide. We first investigated the light propagation in the wide region of the waveguide. In Fig.5.3, are reported topography, amplitude and phase maps recorded while the probe was scanned over an area of $35\mu m \times 35\mu m$. The scan is performed by recording 256 pixel in each direction, which corresponds to a spatial sampling of $\sim 137nm$. The sampling is therefore smaller than the lateral resolution of the scanning probe. A comparison of the optical signal with the topography shows a good confinement of the light in the waveguide. Both amplitude and phase maps show a significant signal only over the waveguide area. We observe that the amplitude signal presents some inhomogeneities. In fact, this part of the structure has a width much larger than the wavelength, therefore, it is supposed to support several modes. From the experimental point of

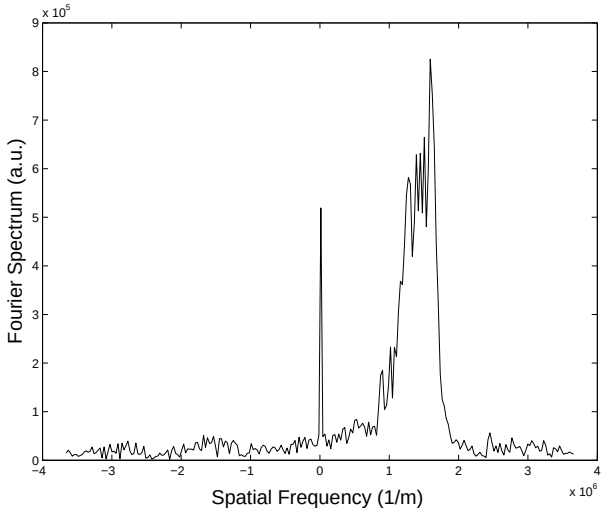

Figure 5.4: *Absolute value of the Fourier transform of the complex amplitude field, recorded over the wide part of the air-bridge waveguide and computed along the direction of propagation.*

view, it is not an easy task to be selective on the mode injection. One could wish, for instance, to let only the fundamental mode propagate in the waveguide. However, in the most general case, several modes, with different propagation constants, are simultaneously excited. The beating between the different modes produces the observed inhomogeneities. This hypothesis can be confirmed by operating a Fourier analysis of the optical signal. In this case, the heterodyne detection provides an important advantage. As a first step, since we measure simultaneously amplitude and phase of the guided light, we can obtain experimentally the complex amplitude of the field. By indicating with $\mathbf{a}(x, y)$ the recorded amplitude signal and with $\mathbf{p}(x, y)$ the corresponding phase, we can write the complex field amplitude $\mathbf{A}(x, y)$ as

$$\mathbf{A}(x, y) = \mathbf{a}(x, y) \cdot e^{i \cdot \mathbf{p}(x,y)}. \tag{5.1}$$

Secondly we compute the Fourier transform of the expression in Eq.(5.1) along the direction of propagation. In Fig.5.4, we report the results of the calculation for the data reported in Fig.5.3. The computation of the complex Fourier transform provides not only an information on the spatial frequencies composing the optical pattern, but also the direction of propagation of such frequencies. In the spectrum in Fig.5.4, for instance, we observe that the most significant peaks are found on the positive side indicating that in the scanned region no light is reflected back. This additional information on the propagation direction can be extremely useful in the interpretation of the optical properties of a waveguide device, and can be provided only by a simultaneous measurement of amplitude and phase of the probed field. The inverse of the frequency values provides the effective wavelengths for each propagating mode from which one can determine the corresponding propagation constant. In Fig.5.4, we find the most significant peaks in the range of frequencies $(1.2-1.6)\times 10^6 m^{-1}$, which corresponds to the range of effective wavelengths $0.84 - 0.62\mu m$. We find, for the highest peak, an effective wavelength of $0.62\mu m$, which corresponds to an effective refractive index $n_{eff} = 2.5$. Numerical results performed by means of a commercial software (Microwave Studio, CST, Darmstadt, Germany) predict, for the fundamental TM-like mode, a value of $0.61\mu m$, which is in very good agreement with the experimental value. This analysis confirms that the fundamental mode is actually propagated

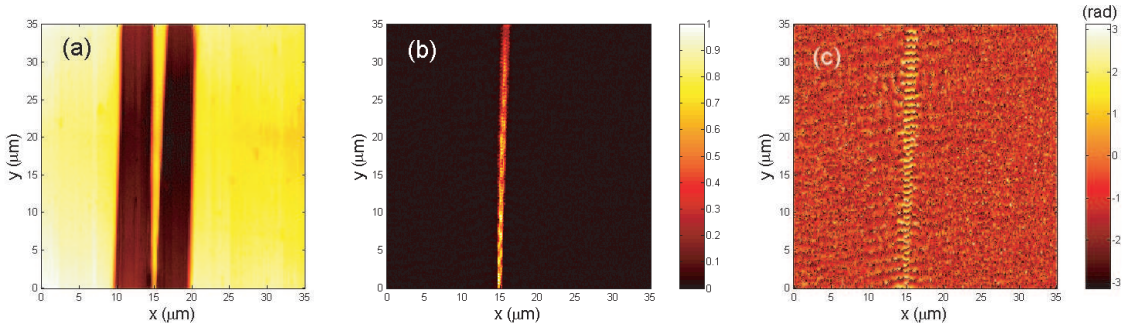

Figure 5.5: *(a)Topography, (b) amplitude and (c) phase maps simultaneously recorded over the air-bridge area. The amplitude map is normalized to the maximum value of the detected optical signal.*

in the waveguide and that it is superposed to several higher order modes.
As a second step, we moved to the region of the air-bridge. In Fig.5.5, are reported topography, amplitude and phase map recorded over an area of $35\mu m \times 35\mu m$ including the air-bridge and a part of the tapered zone. Also in this case we can observe a very good confinement of the light

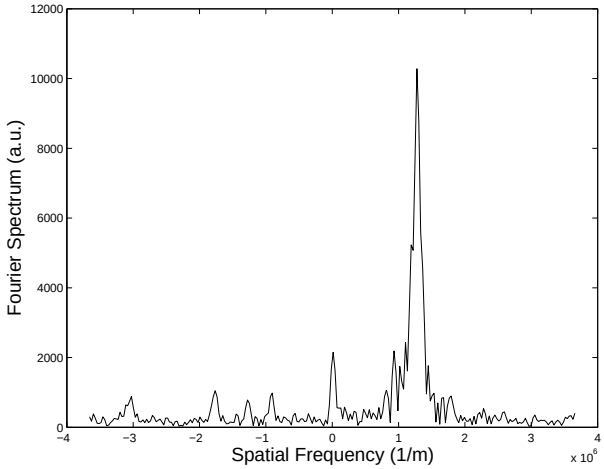

Figure 5.6: *Absolute value of the Fourier transform of the complex amplitude field, recorded over the air-bridge area, computed along the direction of propagation.*

in the waveguide region. The Fourier analysis, reported in Fig.5.6, shows a rather large peak centered at 1.27×10^6, which corresponds to an effective wavelength of $0.78\mu m$ and an effective refractive index $n_{eff} = 1.98$. Numerical simulations leads to a value for the fundamental TM-like mode of $0.71\mu m$, which is in good agreement with the experimental value. The reason why the effective wavelength for the fundamental mode changes from the wide to the bridge waveguide, is due to the fact that the latter, being a suspended membrane, is completely surrounded by air. Therefore, the radiation experiences an effective refractive index which is lower than the one of the bulk silicon. As a consequence the effective wavelength increases.
The results reported in this section show an excellent agreement with the theoretical expectations and demonstrate the capability of the present set-up to characterize photonic devices operating

in the 1.55μm wavelength regime.

5.4 Straight photonic crystal waveguide

The second investigated structure is a straight photonic crystal waveguide (PhC). The crystal lattice consists of a square array of microfabricated cylindrical holes. Also in this case, the region of the crystal is undercut resulting in a suspended membrane. A SEM image of the structure is displayed in Fig.5.7. The design parameters of the PhC structure are lattice constant a = 496nm, hole radius r = 190nm and slab thickness t = 290nm. These values are chosen to give rise to a TE-like (in-plane polarization) photonic band gap for wavelengths around 1.5 μm. All the measurements reported in the following have been performed in TE polarization. The waveguide is formed by eliminating a single row of holes such that the propagating modes are confined within the defect [9]. The input and the output structures are similar to the ones described for the air-bridge waveguide.

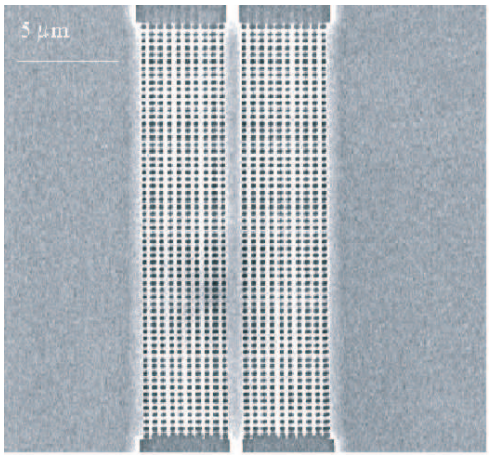

Figure 5.7: *SEM picture of the straight photonic crystal waveguide.*

5.4.1 Comparison of far- and near-field measurements

The spectral and the transmission properties of photonic structures are often investigated by means of far-field experiments. The SNOM technique provides the unique opportunity to image the optical patterns generated by the light propagating inside the photonic device. It can also represent a useful tool for the interpretation of the far-field measurements. In Fig. 5.8, we report a far-field spectral transmission curve for the investigated PhC. The curve has been obtained with the experimental set-up reported in [74]. Data are recorded in the wavelength range 1440-1580nm. We observe that only in a limited interval the device shows a significant transmission. Optimum throughput is observed for wavelengths around 1.55μm, whereas, as the wavelength decreases, the transmission deteriorates reaching a cutoff at 1.52μm. The curve presents a periodic modulation which is due to internal Fabry-Perot cavity effects. However, the period in the peaks cannot be directly related to the free spectral range of the internal cavity. Actually, it is modified according to the wavelength sampling adopted during the measurement.

In Fig. 5.9, we report topography, amplitude and phase maps recorded at a wavelength of 1560nm by scanning the probe over an area of 14μm×14μm around the defect line. The

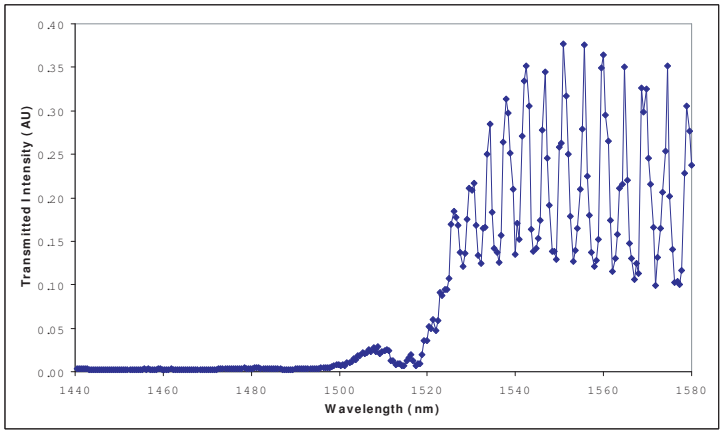

Figure 5.8: *PhC far-field transmission curve.*

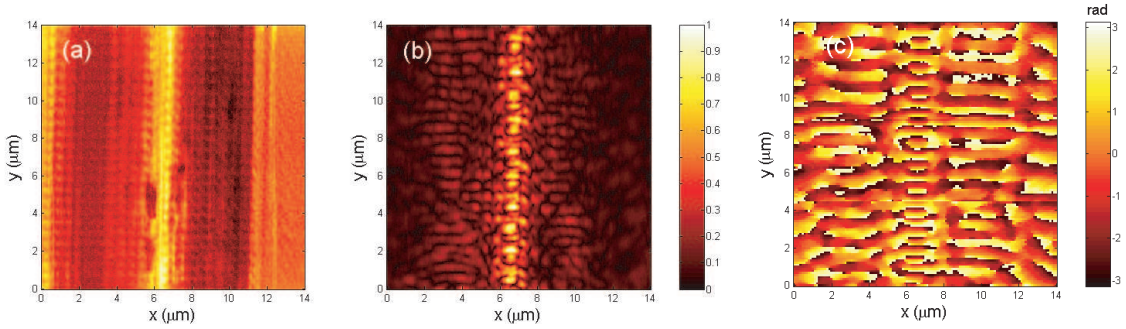

Figure 5.9: *(a)Topography, (b) amplitude and (c) phase maps simultaneously recorded over the PhC defect line at a wavelength of 1560nm. The topographical signal is treated with a plane removal algorithm in order to highlight the defect line location. The amplitude map is normalized to the maximum value of the detected optical signal.*

comparison of the amplitude map with the recorded topography shows that most of the light is confined in the defect line. A plane removal algorithm has been applied to the topographical signal in order to highlight the defect line location. A modulated optical pattern is observable along the direction of propagation. This effect is assumed to be determined by the Fabry-Perot resonances of the cavity formed by the edge facets of the waveguide. The phase map presents regular patterns overall the scanned zone. In particular, along the length of the defect line, the wavefronts look planar with a more frequent repetitions compared to the surrounding zone. In Fig. 5.10, we report topography and amplitude recorded at two other selected wavelengths, 1533 and 1520nm. In this case the probe was scanned over a smaller area of $7\mu m \times 7\mu m$. By comparing Figs. 5.10(a) and (b), we can observe that the optical signal is still mostly concentrated along the defect line, however, the light pattern distribution seems to suggest that the guiding mechanism has changed. Finally, from Figs. 5.10(c) and (d) we observe that at a wavelength of 1520nm, corresponding to the cutoff observed in the far-field transmission curve, the optical signal is mostly detected outside the defect and a higher signal is recorded in the surrounding zone of the holes.
This first rough near-field analysis represents an alternative visualization of the spectral behavior

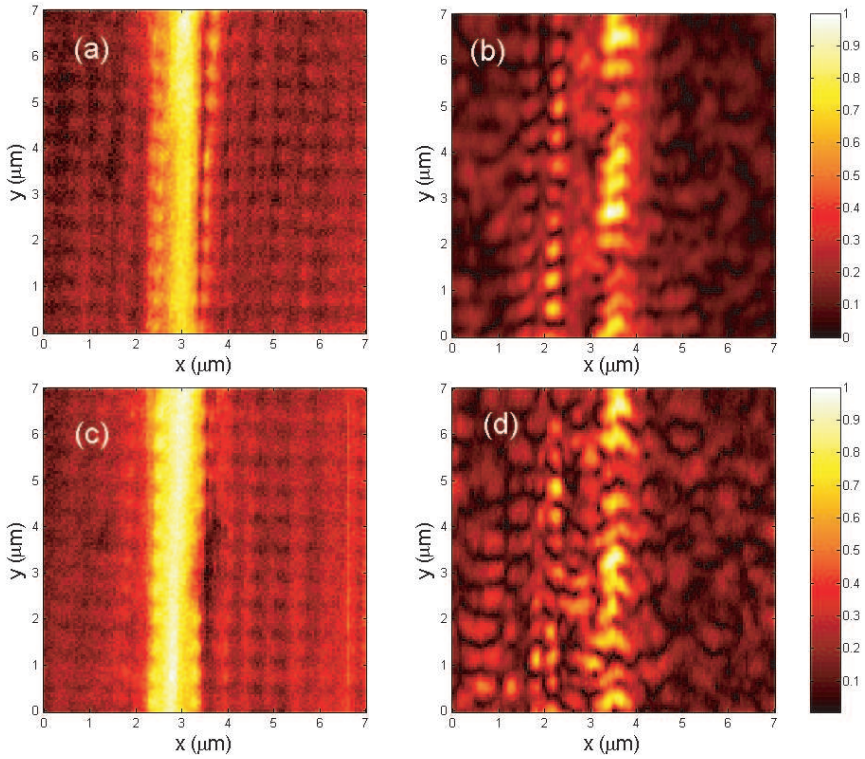

Figure 5.10: *(a)Topography and (b) amplitude map recorded at 1533nm. (c)Topography and (d) amplitude map recorded at 1520nm. Topographical signals are treated with a plane removal algorithm in order to highlight the defect line location. Amplitude maps are normalized to the respective maximum values of the detected optical signals.*

of the light coupled in the PhC structure. In particular, it demonstrates that, by decreasing the wavelength in the optimum transmission range, the guiding mechanisms are modified and eventually, at the cutoff wavelength, the light couples to modes of the crystal, which diffuse light overall the membrane and are no longer guided toward the output waveguide structure.

5.4.2 Influence of topography on SNOM images

The topographical images recorded simultaneously to the SNOM have been useful, so far, to estimate the confinement of the propagating light into the investigated waveguide structures. The probe aperture has a diameter of 200nm, however, because of the metallic layer, the resulting surface, which is actually scanned over the sample surface, has a diameter of 400nm. The topographical resolution is then lower than the one achievable in SNOM images. The size of the apex is comparable with the diameter of the holes, which can be barely resolved in the topographical images (see Fig. 5.9(a)). However, the topographical images recorded by means of the scanning probe on the PhC surface present interesting aspects which are worth to be mentioned. In Fig. 5.11(a) we report the topography relative to the measurement at 1560nm reported in section 5.4.1. In this case, no plane removal algorithm was applied. In Fig. 5.11(c) we report normalized cross sections of the topographical signal for three selected y positions. At the very right side we can observe the point of junction between the membrane and the

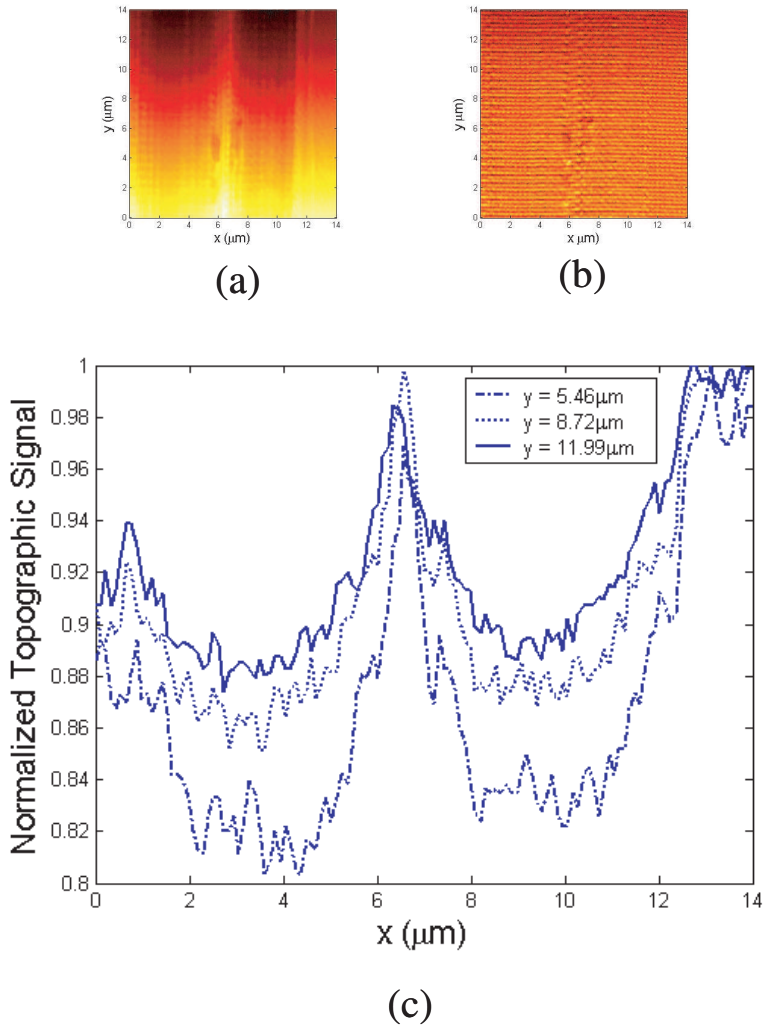

Figure 5.11: *(a) Topographical signal recorded over an area surrounding the defect line.(b) Corresponding probe-surface interaction force map. (c) Cross sections of the topography map. The corresponding y position are reported on the plot.*

silicon layer. We observe that when the probe scans the holes region, the topography presents a valley, whereas the height of the defect line is the same than the one recorded at the junction. This effect is due to the dumping in the interaction force between the probe and the surface. In fact, the measurement is operated in constant force mode. The map of the force signal is, therefore, constant over the scanned region (see Fig. 5.11(b)). When the probe is scanned over the region of the holes, it experiences an average interaction between the air in the holes and the surrounding silicon. As a consequence the interaction force decreases and, in order to keep it constant, the probe is lowered towards the surface, producing the observed valleys. We observe that, all over the holes region, the height decreases of 20% compared to the junction and the defect line zone. This circumstance can produce an effect on SNOM images. In fact, when the probe is closer to the surface the damping in the evanescent field intensity is lower and more light can be transferred to the detector. Therefore, one has to be aware of this effect in estimating the ratio between the amount of light propagating in the defect line to the one propagated in

the surrounding crystal.

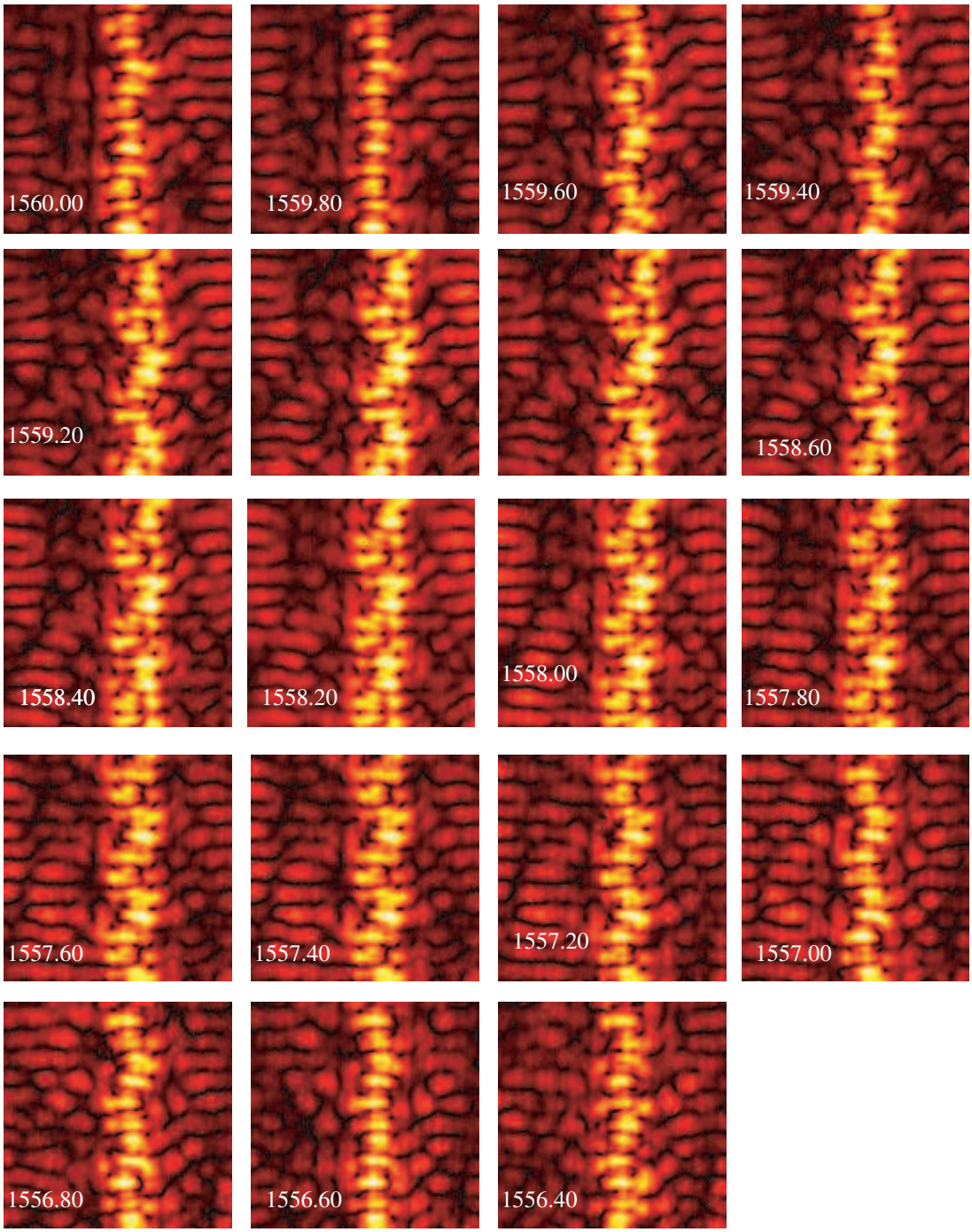

Figure 5.12: *(Series of amplitude maps recorded over an area of 7μm×7μm around the defect line. The corresponding wavelengths are indicated on the maps in nanometers. All the maps are normalized to the respective maximum values of the detected optical signals.*

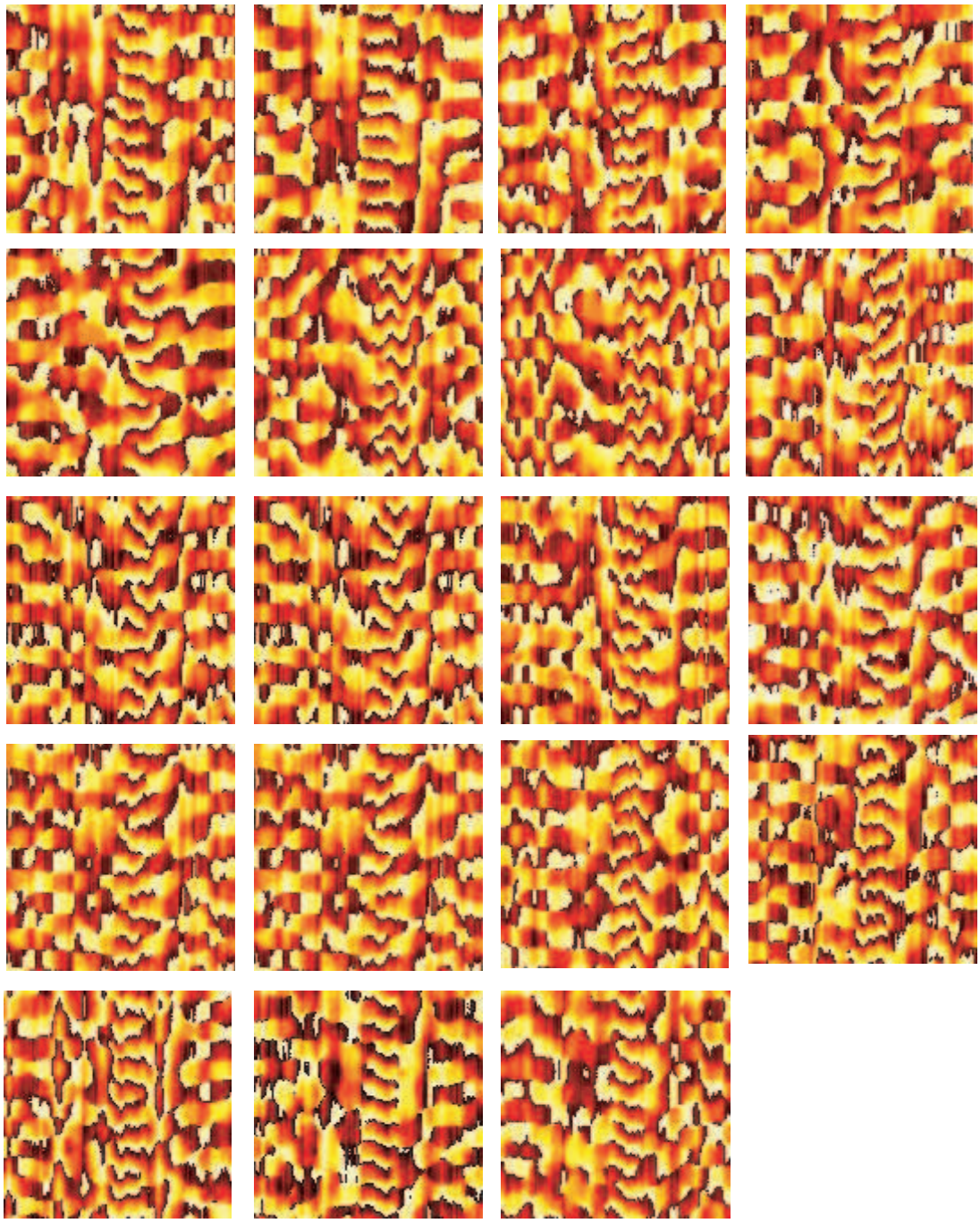

Figure 5.13: *Series of phase maps recorded simultaneously to the amplitudes reported in Fig.5.12. Data are reported in radians. Phase values are in the range $+\pi$ (white) and $-\pi$ (black).*

5.5 Near-field spectral analysis

In this section, we present a near-field spectral investigation of the light propagating in the PhC waveguide. First, we select a scanning area of $7\mu m \times 7\mu m$ around the defect line. Second, we fix the injection conditions and the polarization of light (TE) and keep them constant during the

whole experiment. Third, we change the injected wavelength by tuning the laser source. Scans are performed by acquiring 128 points both in x and y-direction, which corresponds to a spatial sampling of $\sim 55nm$.
In Fig.5.12 and 5.13, we report the sequence of amplitude and phase maps recorded by scanning the wavelength in the decreasing interval 1560-1556.40nm with a step of 0.2nm. We notice that at 1559.80nm the amplitude presents a straight pattern characterized by an even symmetry. The phase map along the defect line reveals a sequence of planar regular wavefront repetitions. By decreasing the wavelength, we observe that the amplitude pattern is modified, showing a lateral oscillation, whose amplitude increases by decreasing the wavelength. The corresponding phase maps present irregular behaviors which barely allow to individuate the defect line location. This effect reaches a maximum in the intermediate wavelength range and then gradually reverts to the initial condition. In fact, we observe that at 1556.60nm the amplitude presents again a straight even-symmetric pattern and the phase becomes again regular. The reverting process occurs in 3.2nm. In order to investigate the periodicity of this effect, we extended the measurements by further decreasing the wavelength. We found that the process was repeated almost identically. A new straight patter was found after 3.1nm at a wavelength of 1553.50nm. The corresponding amplitude and phase maps are reported in Fig. 5.14. This series of measure-

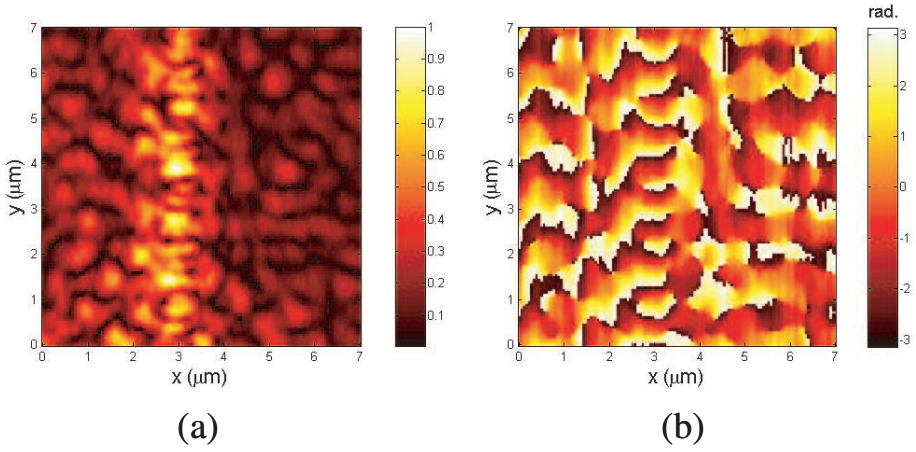

Figure 5.14: *(a) Amplitude and (b) phase maps simultaneously recorded over the PhC defect line at a wavelength of 1533.50nm. The amplitude map is normalized to the maximum value of the detected optical signal.*

ments demonstrate that the guiding mechanism has a periodic behavior with the wavelength. Its period corresponds to $\sim 3.1nm$. Since the experimental conditions were preserved during the measurements, this behavior is presumably due to the geometrical characteristics of the PhC waveguide and to resonances of internal Fabry-Perot cavities delimited by the discontinuities in the waveguide structure.
A more rigorous analysis of the experimental data can be conducted by means of the Fourier analysis. The recorded data present two main behaviors. In some cases, the amplitude map has an even-symmetric straight pattern, whereas in some others we observe an odd-symmetric snake-shaped pattern. In Fig.5.15 (a) and (b), we report the normalized Fourier spectrums, relative to wavelengths 1559.80 and 1559.40nm respectively, calculated along the direction of propagation. At 1559.80nm, corresponding to the case of a straight optical pattern, we observe a single important peak at a spatial frequency of $(0.15\times10^7 m^{-1}$, which yields to an effective

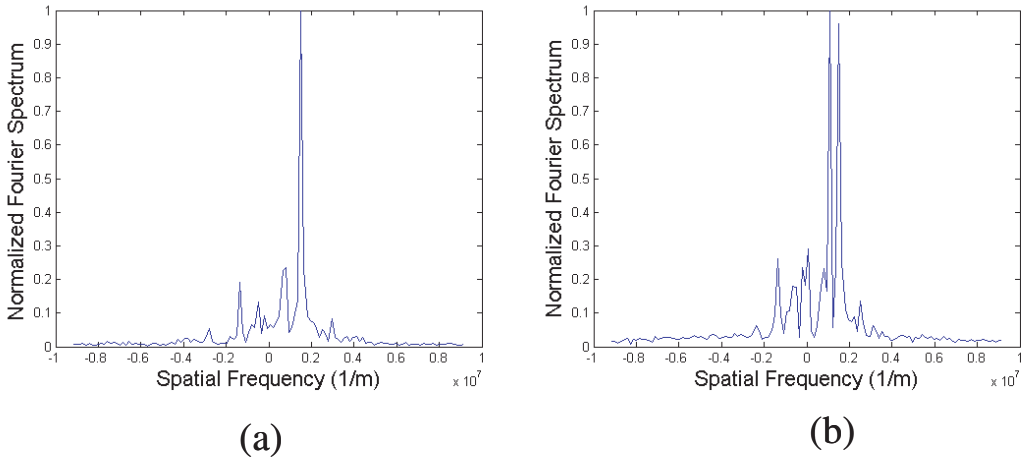

Figure 5.15: *Absolute value of the normalized Fourier transform, computed along the direction of propagation, for the case of (a)*$\lambda = 1559.80nm$ *and (b)* $\lambda = 1559.40nm$.

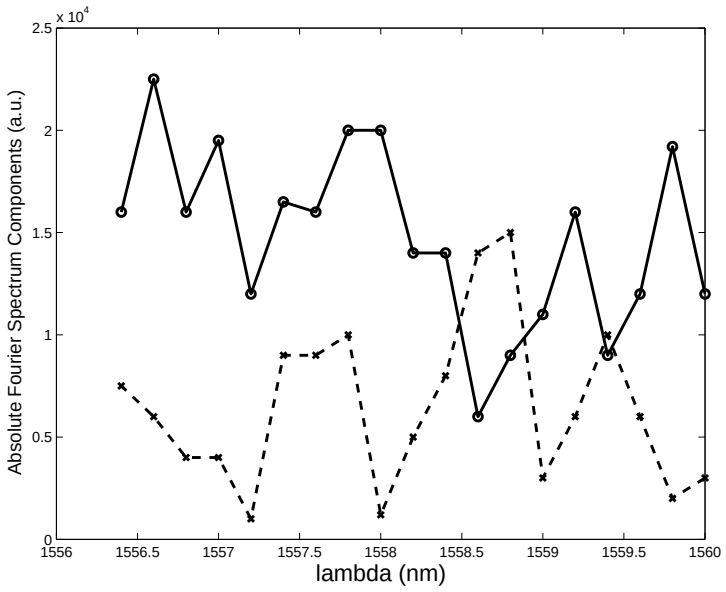

Figure 5.16: *Absolute value of the Fourier transform components, associated to the first (-o-) and the second (-x-) mode in the PhC waveguide plotted like a function of the wavelength.*

wavelength of $\lambda^1_{eff} \cong 0.67\mu m$ and an effective refractive index $n^1_{eff} \cong 2.4$. This result indicates that in this case a single mode is propagating in the defect line. We can observe a smaller peak, corresponding to the same effective wavelength, propagating in the negative direction. Its height correspond to the 20% of the forward propagating peak. We suppose that this backward propagation is determined by the reflection of the propagating mode at the edge facet of the waveguide.

The second selected wavelength corresponds to a case in which the amplitude map is characterized by a snake-pattern. The relative Fourier spectrum, in Fig. 5.15(b), shows the appearance

of a second peak at a spatial frequency of ($0.108\times10^7 m^{-1}$, corresponding to a $\lambda^2_{eff} \cong 0.925\mu m$ and a $n^2_{eff} \cong 1.65$.
These results show that the two main optical patterns recorded in the measurements are determined by the simultaneous excitation of two modes with different propagation constants. In order to estimate the absolute contribution of the two modes in the series of recorded measurements, we computed the Fourier spectrum for each wavelength. Calculations are resumed in Fig.5.16. We notice that the curve associated to the first mode ($\lambda^1_{eff} \cong 0.67\mu m$) is always higher than the one for the second mode. This result indicates that the first mode is coupled with a higher efficiency for almost all wavelengths. This condition has an inversion in a short interval where the curve presents a valley. The minimum value is found at 1558.60nm where the second mode becomes prevalent.

5.6 Theoretical optical properties of the PhC waveguide

The reliability of the experimental results reported in the previous section is verified by analyzing some theoretical aspect of the PhC waveguide. The optical properties of a photonic structure are generally represented by means of a dispersion diagram. The diagram reports, in general, the association of the propagation constant to the optical frequency for all the electromagnetic modes supported by the structure [77]. In Fig.5.17 is reported the dispersion diagram for a TE-like guided modes of the investigated PhC waveguide. Calculations are obtained by a fully three-dimensional model [75]. A detailed description of this diagram is reported in [72]. Here,

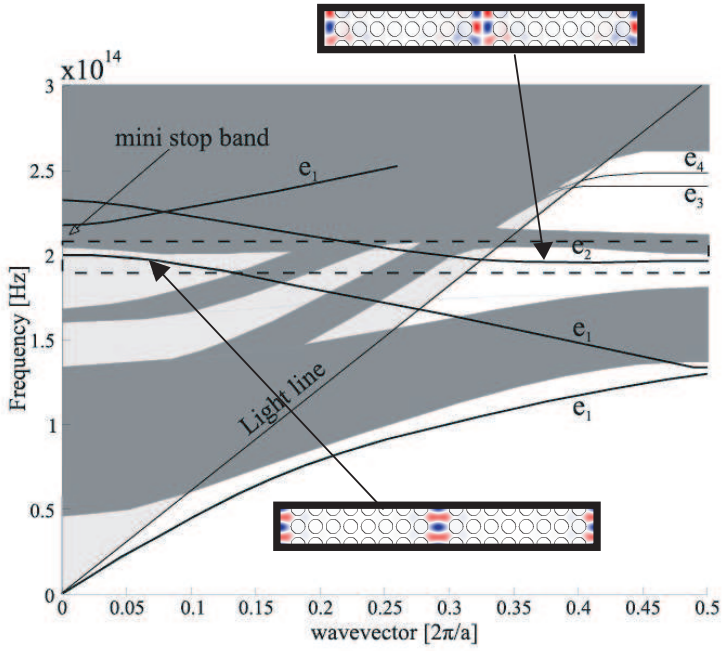

Figure 5.17: *Dispersion diagram for the TE-like mode of the straight PhC waveguide. Pictures in insets show the laterally symmetry associated to defect modes* e_1 *and* e_2.

we will focus on those aspects which provide an interpretation of the reported experimental re-

sults. The interval of optical frequencies corresponding to the investigated range of wavelengths is highlighted by the two dashed lines. The gray regions represent the ensemble of modes supported by the PhC. The white regions represent modes whose propagation is forbidden in the crystal. We observe that the highlighted region overlaps mostly with a white region. However, the introduction of the defect line, produces additional dispersion curves which are indicated by the black lines. The curves of two modes are of particular interest because they cross the forbidden region. Such modes are called the defect modes and are here indicated as e_1 and e_2. Mode e_1 is called the fundamental *refractive-like* mode. It is barely influenced by the periodicity of the PhC. As it propagates in the defect line, it experiences an average value of the refractive index and is guided by total internal reflection at the air-silicon interface [76] like in a standard ridge-waveguide. As depicted in Fig.5.17, the mode is characterized by a laterally even symmetry. Mode e_2 is called the *diffractive-like* mode. The properties of this mode are strongly influenced by the lattice periodicity. The guiding mechanism is determined by Bragg diffraction of the light on the hole planes surrounding the defect line. The mode is characterized by a laterally odd symmetry. In Fig. 5.18, we report simulated amplitude patterns of light propagating

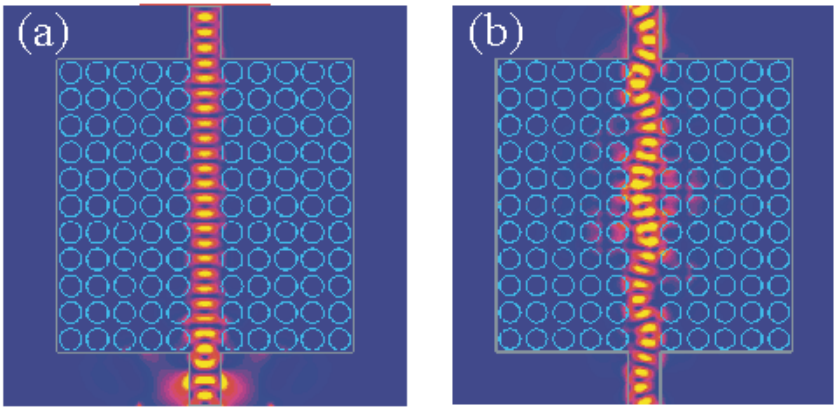

Figure 5.18: *Computed amplitude patterns in the defect line of the PhC waveguide. (a) Fundamental TE-like mode (e_1), (b) superposition of e_1 and e_2 with equal intensity.*

in the defect line of the PhC waveguide. Calculations are performed with a FDTD algorithm. The first case (Fig. 5.18(a)) corresponds to the excitation of the fundamental mode e_1. Due to the limited calculation capacity, the modeled structure does not coincide with the real sample. However, we can remark that the computed optical pattern is comparable with the one obtained experimentally for measurements at 1559.80, 1556.60 and 1553.50nm. Since the Fourier analysis showed in those cases the presence of a single mode, we conclude that such a mode coincides with the calculated fundamental *refractive-like* mode. Calculations of the effective wavelength, for a wavelength of $1.5\mu m$, yields for the modeled structure to a value $\lambda_{eff}^{e1} = 0.560nm$ which is comparable with the one determined experimentally for the first observed mode.
In Fig. 5.18(b), we report a case in which mode e_1 and e_2 simultaneously propagates into the defect line. In the calculation the intensity associated to the two modes is the same. We observe that, as an effect of the superposition, the resulting pattern is snake-shaped and is comparable with the snake-shaped pattern measured experimentally. In those cases, the Fourier analysis showed the presence of two modes simultaneously propagating in the defect line. The experimental effective wavelength for the second mode was found to be $\lambda_{eff}^{2} \cong 0.925\mu m$. Calculations

for the modeled structure yields for the second mode to $\lambda_{eff}^{e2} = 0.720\mu m$. We conclude that the recorded snake-shape is determined by the superposition of the fundamental laterally even mode and the second laterally odd mode.
The experimental and numerical results discussed so far are qualitatively very consistent. However, a quantitative analysis is more delicate and is influenced by different aspects. Firstly, the numerical results are rescalable with the wavelength and with the geometrical characteristics of the modeled structure. This means that a quantitative comparison with the experimental results can be performed only if the modeled structure coincides identically with the investigated one. Secondly, the experimental results are surprising if compared with the dispersion diagram. Actually, for all the investigated wavelengths we find, associated to each mode, a single effective wavelength. The dispersion diagram shows that the curves for the defect modes, especially for the case of mode e_2, are nearly flat in the region of the investigated frequencies. This means that, in principle, small wavelength variations can lead to large variations of the propagation constants. However, the dispersion diagram is calculated for an infinite structure, whereas the investigated sample has obviously finite dimensions. The fact that we find constant values for the effective wavelengths can be attributed to the particular experimental conditions. For instance, we suppose that the injection conditions and the actual geometrical characteristics might influence, in a selective way, the propagation properties of the injected modes.

5.7 Investigation of the coupling efficiency

The analysis of the experimental and theoretical results leads to the conclusion that the PhC waveguide supports only the fundamental laterally even mode and the second laterally odd mode. We attempted to estimate the coupling efficiency of both modes by performing a spectral set of measurements at the input region of the PhC waveguide. In Fig. 5.19, for instance, we report topography, amplitude and phase maps, recorded, at a wavelength of 1559.5nm, over an area of $14\mu m \times 14\mu m$ including the junction between the tapered waveguide and the crystal on the input side of the PhC. The topography shows the location of the scanning area. We notice

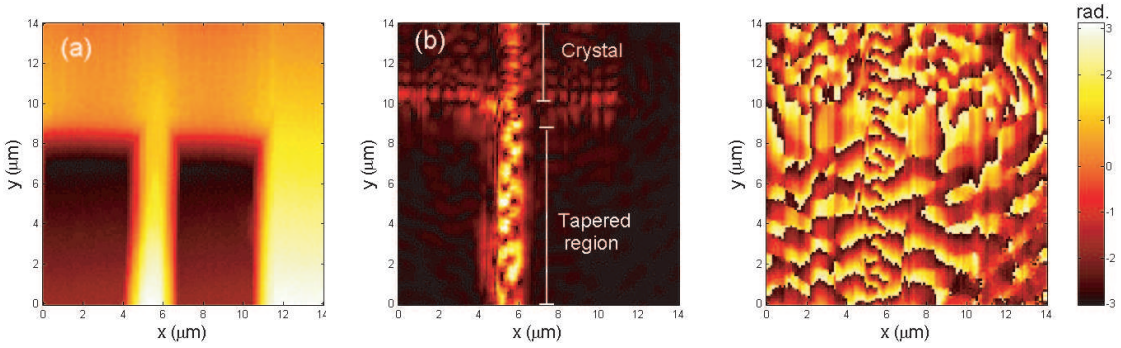

Figure 5.19: *(a) Topography, (b) amplitude and (c) phase maps recorded over an area of $14\mu m \times 14\mu m$ at the input region of the PhC waveguide. The amplitude is normalized to the maximum recorded value of the optical signal.*

that the recorded optical signal is much stronger in the tapered region than in the crystal. This indicates that most of the light is leaked outside the structure or reflected back at the junction facet. As mentioned in previous sections, the input structure behaves like a multi-mode waveguide. However, as the structure tapers, most modes run into cutoff. We expect only the

fundamental and the second mode to be guided till the entrance of the PhC.
As a parameter to investigate the light coupling efficiency, we adopt the ratio $\mathbb{R}$ of the amount of light detected in the crystal to the one detected in the tapered region for the different wavelengths. Both values are obtained by integrating on the optical signal in the corresponding area. The investigated wavelengths ranged from 1553 to 1560nm with a step of 0.5nm. The $\mathbb{R}$ values

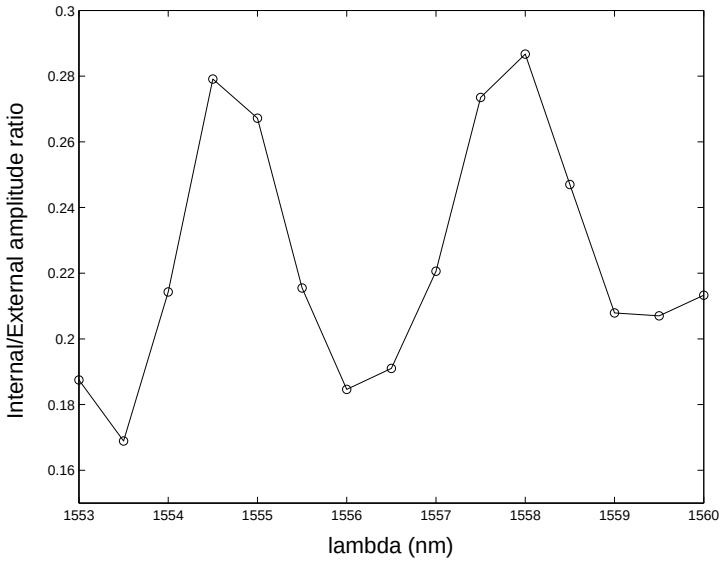

Figure 5.20: *Ratio $\mathbb{R}$ of the total optical signal detected in the tapered region to the total optical signal detected in the crystal region plotted as a function of the investigated wavelengths.*

are resumed like a function of the wavelength in Fig. 5.20. We observe that the curve shows a periodic pattern with a period of $\sim 3nm$. This value reminds the period of the fundamental mode excitation estimated during the internal spectral analysis. In particular, we observe that the curve in Fig.5.20 presents minima at those wavelengths for which the internal spectral analysis indicates the single excitation of the fundamental mode.
The $\mathbb{R}$ curve presents an interesting correlation with a previous reported result. Actually, in Fig. 5.16, we have resumed the internal contributions of the propagating modes by plotting the intensities of the Fourier spectrum like a function of the injected wavelength. In the interval of wavelengths around 1558.60nm, we found that the second mode becomes prevalent compared to the first one. This suggests that at those wavelengths the second mode is coupled with a higher efficiency. As a consequence one would expect to find more light coupled into the PhC. This expectation is in agreement with the results reported in Fig. 5.20. Actually, in the same interval of wavelengths, the curve shows a maximum. On the contrary, when only the first mode is excited in the waveguide, one would expect most of the second mode to be reflected back and less light to be coupled to the PhC. This condition is again well visible in the curve in Fig. 5.20, which presents minima for those wavelengths at which only the fundamental mode propagates in the PhC. We conclude that the reported oscillation in the light coupling efficiency is prevalently related to the coupling efficiency of the second mode. For some wavelengths, such efficiency is so low that only the first mode is detected in the waveguide. This conclusion was partially expected from numerical simulations, which indicate that the coupling efficiency of the second mode is inferior to the one for the fundamental mode.

5.8 Corner PhC waveguide

The last investigated sample is the corner PhC waveguide. A SEM image of the structure is displayed in Fig.5.21. The device is fabricated with the same technology described for the previous investigated structures. In this case, the defect line is characterized by a 90° bend. In

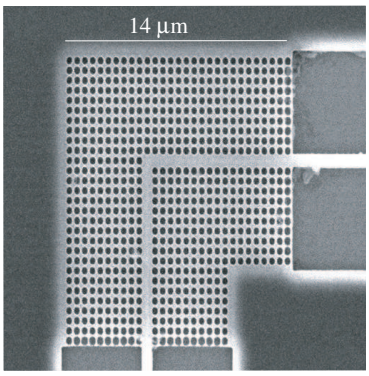

Figure 5.21: *SEM image of the corner PhC waveguide.*

a dielectric structures, like optical fibers, one achieves light guiding by total internal reflection. When the fiber is bent very tightly the angle of incidence becomes too large and total internal reflection can no longer occur. The possibility to guide light even around tight angles would open interesting perspectives in lightwave circuit technology. A similar device can be fabricated by means of the SOI technology and relies on the high refractive index difference between the cladding and the core [78]. Promising alternatives, in this sense, are provided by the PhC technology [79,80]. In a PhC, the confinement and guiding mechanisms are no longer related to the total internal reflection conditions and are then independent from the angle of incidence. The device reported in Fig.5.21 has been studied and developed for this purpose. Unfortunately, the fragile membrane collapsed during the scanning processes and a detailed spectral analysis could not be accomplished. However, some recorded near-field images demonstrate the effectiveness of the proposed design. With respect to Fig.5.21, the light was injected from the bottom. In Fig.5.22, are reported two examples of near-field measurements recorded by scanning the probe over the area of the corner. Figs.5.22(a) and (b) show the amplitude and the phase maps recorded at a wavelength of 1550nm respectively. First, we can observe a very good confinement of the light into the bent defect line. In both the arms of the corner it is possible to observe a rather straight pattern similar to the one observed in the straight PhC for the fundamental laterally even mode. In the region of the waveguide bend, we can observe a significant penetration of the light into the PhC lattice. A significantly higher amplitude signal is detected by the SNOM in this region due to two mechanisms: first, the corner region acts as a resonant cavity, resulting in a significantly higher field amplitude inside; and second there is significantly greater leakage or scattering of light from the vicinity of the corner, as compared with the straight waveguides. Fig.5.22 (c) and (d) shows amplitude and phase maps recorded at a wavelength of 1549.60nm. We observe that, in this case, the optical pattern in the two arms shows significant differences. In the input arm, the amplitude pattern shows an even symmetry, whereas in the output arm we recognize the well-known snake-shaped pattern. Both penetration in the crystal and field enhancement are reduced at the corner. In both the reported measurements the phase maps are very noisy and the application of the Fourier analysis does not provide significant results. However, the recorded optical patterns remind the ones associated to the modes of the straight

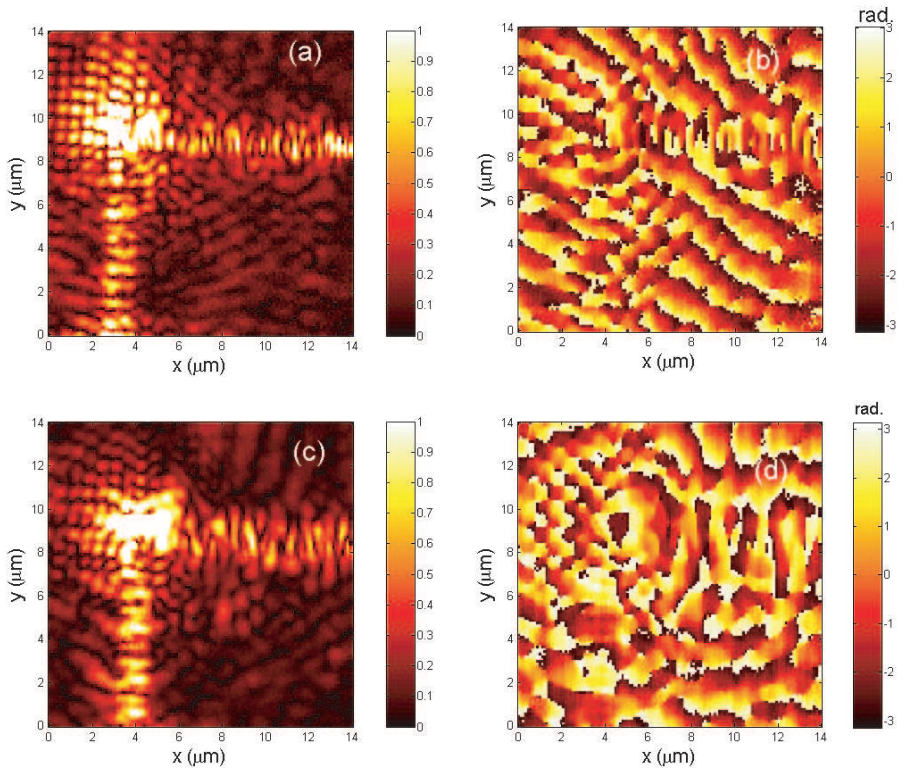

Figure 5.22: *Amplitude (a) and phase (b) maps recorded over an area of* $14\mu m \times 14\mu m$ *surrounding the* 90^o *bend at a wavelength of 1550nm. (c) Amplitude and (d) phase map recorded in the same region at 1549.60nm. The amplitude maps are normalized to the respective maxima of the recorded optical signal.*

PhC. Numerical simulations relative to this structure are reported in [72]. Calculations show that, in a limited range of wavelengths, both fundamental and second mode can be guided by this structure through the 90^o bend.

5.9 Conclusions

We have demonstrated the direct observation of the amplitude and phase of an optical field propagating in ridge and photonic crystal SOI-based waveguides for wavelengths around 1.55m using heterodyne scanning near-field optical microscopy (SNOM). The simultaneous information on amplitude and phase allowed to determine experimentally the complex field amplitude of the probed fields. In the case of the standard ridge waveguide, we have investigated the propagation characteristics of the fundamental TM-like mode. A Fourier analysis of the complex amplitude allows to determine parameters like the effective wavelength and the effective refractive index for the investigated mode. Such parameters have been compared to numerical values, obtained from a computational model of the structure, showing an excellent agreement.
We have demonstrated a near-field spectral analysis of the modes propagating into a straight PhC waveguide. The structure is designed to support TE-like modes. The range of wavelengths has been chosen according to the far-field transmission curve of the device. We have investigated both regions of optimum transmission and regions where the curve shows a cut-off. In the region

of optimum transmission the near-field analysis revealed the propagation of the fundamental and the second order mode. In particular, we have individuated a discrete set of wavelengths for which only the fundamental mode is guided in the defect line. Such circumstance occurred with a period in the wavelength of $\sim 3.1nm$. This observation is probably attributable to an internal Fabry-Perot cavity effect. The investigation of the coupling efficiency has been performed by scanning the microscope in the input region of the PhC. This analysis revealed that the coupling efficiency of the second mode has a periodic behavior with the wavelength. In particular, we have demonstrated that the second mode is coupled with a lower efficiency for those wavelengths for which only the fundamental mode was observed in the defect line.
The experimental determined effective wavelengths of the investigated modes are consistent with numerical results obtained from a 3D computational model of the structure.
The near-field analysis in the cut-off region showed that for those wavelengths the light starts to propagate in the whole crystal producing the deterioration of the transmission signal observed in the far-field measurements.
Finally, we have investigated the case of a corner PhC waveguide. Since the structure collapsed during the experiment, the spectral analysis has been limited to only some wavelengths. However, a few images allow to individuate also in this case the propagation of the fundamental and the second order mode around the 90^o bend. In particular, effects of field enhancement and penetration in the structure have been demonstrated by scanning the probe in the region of the corner.

Conclusions

In this thesis, we have demonstrated the use of optical interferometric techniques for the study of the optical properties of nano-structured materials. Interferometric set-ups allow to detect simultaneously the amplitude (or the intensity) and the phase of the investigated optical fields. The amplitude signal enables to determine the optical patterns generated by the interaction of the light with samples. However, in experiments aiming to study the propagation properties of the light, both in bulk materials or in free space, the additional information on the phase field evolution is crucial. Similar properties have been investigated in the case of optical scanning probes and photonic crystal waveguides.

The vectorial transmission properties of an uncoated tapered fiber tip have been investigated by integrating the probe into a Multiple-Heterodyne Scanning Probe Optical Microscope (MH-SPOM). This novel apparatus is characterized by two new capabilities:*polarization sensitivity of the detection system* and *beam labeling*. The polarization response of the probe to transverse and longitudinal field components has been investigated by scanning the tip in suitable 3D optical configurations. Two main results have been obtained. Firstly, we have demonstrated that in case of transverse field configurations the polarization transfer function of the microscope collecting system *probe+fiber* can be characterized by a single Jones matrix. Secondly, we have demonstrated that longitudinal field components couple to the probe as well as transverse field components. The mechanism that transforms the longitudinal field into transverse eigenmodes of the optical fiber has been described by means of a simplified coupling model.
The technique described in this work is of general application and is suitable to be applied to an even wider set of scanning optical probes.

The propagation properties of electromagnetic modes guided into standard microfabricated fully-metal coated scanning optical probes have been investigated both theoretically and experimentally. When a light beam is injected into the probe, several modes are in general excited. A 3D computational analysis of the probe structure allowed to individuate two modes of particular interest: the fundamental linearly polarized HE_{11} mode and the radially polarized TM_{01} mode. We have discussed the propagation mechanisms that allow to guide these modes as far as the probe apex and to provide the best performances in terms of intensity throughput and lateral resolution. We have individuated experimental injection techniques that allow to selectively excite modes HE_{11} and TM_{01}. Such techniques have been applied to the case of a standard aperture-less probe. The optical patterns transmitted at a few microns above the probe apex for each injection condition have been imaged by means of a high resolution Mach-Zehnder interference microscope. This instrument allows to simultaneously record intensity and phase patterns of the imaged field. The effectiveness of the techniques has been demonstrated by comparing the experimental patterns with the ones calculated by means of the 3D computational model.

Propagation properties of the light in photonic crystal waveguides operating at wavelength around $1.55\mu m$ have been investigated by means of a canonical heterodyne SNOM (H-SNOM). Contrarily to the conventional far-field spectral investigation, SNOM measurements allow to visualize the flux of the light inside the waveguide. Effective wavelengths and effective refractive indexes for the different modes have been determined by means of the Fourier analysis of the experimentally determined complex field amplitudes. The reported experimental results are consistent with numerical expectations obtained from computational models of the investigated structures. Our conclusions demonstrate the effectiveness of the heterodyne SNOM technique in the study of the electromagnetic properties of photonic devices.

Acknowledgments

I owe the success of this thesis work to the support and the collaboration of many people.
I want to thank Prof. René Dändliker for giving me the chance to join the Applied Optics group as a PhD student and a research assistant. I am grateful to him for providing me with his scientific support and for eventually being a jury member. I will jealously keep his corrections to my drafts and manuscripts as an example of great professionalism.
I thank Dr Luciana Vaccaro for inviting me to join her scientific activity and for introducing me to the Nanooptics field. Her support has been very important for me, especially in the beginning, when I had to deal with the difficulties of living and working in a foreign country.
Events led Prof. Hans Peter Herzig to be my eventual supervisor and a jury member. I am aware this was not a comfortable task and I am very grateful to him for his help and his contribution to the final version of this manuscript.
I thank the other jury members, Prof. Daniel Courjon and Prof. David Sandoghdar, for their editorial and scientific advices.
I thank my friend and colleague Dr Emiliano Descrovi for the great time we have been spending together in and outside our institute (Antani!). I'm very glad that our friendship was finally fulfilled by a scientific collaboration that led to the excellent results presented in the fourth chapter of this thesis work. Our collaboration was supported by Dr Toralf Scharf who I thank for his technical advices and his great sense of humor.
Most electronics in my experimental set-up was 'home-made'. I thank Marcel Groccia for providing me with all those nice and efficient devices.
The experiment presented in the fifth chapter of this thesis is the fruit of a collaboration between the IMT of Neuchâtel and the Department of Electrical and Computer Engineering of the University of California, San Diego (US). I thank the Californian group, Prof. Yeshaiahu Fainman, Dr Uriel Levy and Maxim Abashin, for their contribution to the experiment and for the logistic and instrumental support. I thank my colleagues Iwan Märki and Dr Martin Salt for providing me with numerical simulations and the many advices and suggestions. The collaboration was coordinated by Dr Wataru Nakagawa. I am very grateful to Wataru for his constant support and kindness and for the several conversations we had in these years that, doubtless, contributed to improve my English. Most results reported in these pages have been published thanks to his precious contribution.
I would like to thank the present and the old colleagues of the Applied Optics group together with the administration staff of the IMT for allowing me to work in a friendly and stimulating environment.
I enjoyed very much my PhD experience because, even in the darkest time, I could count on the nearness and the support of my family and my friends.
I thank my family in Naples. Our weekly phone conversations always gave me reasons to go ahead in my work and to overcome the inevitable moments of demoralization.
I want to thank my friend and room colleague, Felix Schdelin, for sharing my passion for beach

volleyball and sports in general. He always had some new joke for cheering me up.
I thank my colleague and friend Dr Omar Manzardo for the infinite talks and discussions about science and nearly everything. It was for sure a lot of beer!
I thank Sara and Giacomo (The Orange Living Room acoustic band) for playing music together, and my dear friends Caterina, Giuseppe, Myriam, Iovanna, Rolf and Laura for sharing all that fun.
Finally, I would like to thank all the lovely people who crossed my way in the past four years and who helped me to grow as a scientist and, above all, as a man.
Thank you!

Publications

Most results of this thesis work have been published in international journals and presented to international conferences:

- P.Tortora, E. Descrovi, L. Vaccaro, L. Aeschimann, R. Dndliker "Selective coupling of HE_{11} and TM_{01} modes into microfabricated fully metal-coated quartz probes", submitted to Ultramicroscopy (16th of January 2006).
- M. Abashin, P. Tortora, I. Maerki, U. Levy, W. Nakagawa, L. Vaccaro, H. P. Herzig, and Y. Fainman, "Near field characterization of propagating modes in photonic crystal waveguides" , accepted for publication in Optics Express (6th January 2006).
- P. Tortora, R. Dndliker, W. Nakagawa, L. Vaccaro,' Detection of Non-Paraxial Optical Fields by Optical Fiber Tip Probes', accepted for publication in Optics Communication.
- P. Tortora, M. Abashin, I. Mrki, W. Nakagawa, L. Vaccaro, M. Salt, U. Levy, H. P. Herzig and Y. Fainman, "Observation of amplitude and phase in ridge and photonic crystal waveguides operating at $1.55\mu m$ using heterodyne scanning near-field optical microscopy", Opt. Lett. **30**, 2885-2887 (2005).
- R. Dndliker, P.Tortora, L. Vaccaro, A. Nesci, 'Measuring 3D polarization with scanning optical probes', Journal of Optics A: Pure and Applied Optics **6**, issue 3, S18-S23 (2004).
- P. Tortora, M. Abashin, I. Mrki,1 W. Nakagawa, L. Vaccaro, U. Levy, M. Salt, Y. Fainman, and H. P. Herzig, 'Investigation of optical propagation in photonic structures by heterodyne scanning near-field optical microscopy (H-SNOM)', EOS Topical Meeting on Advanced Imaging Techniques, June 29-July , 1 London(UK) 2005.
- M. Abashin, U. Levy, Y. Fainman, P. Tortora, W. Nakagawa, and L. Vaccaro, 'Near-field investigation of mode structure in photonic crystal waveguides', Quantum Electronics and Laser Science (QELS) Conference, Baltimore, MD, USA, May 22-27, 2005.
- P.Tortora, M. Abashin, I. Mrki, W. Nakagawa, L. Vaccaro, M. Salt, H. P. Herzig, U.Levy, and Y. Fainman, 'Investigation of the spectral characteristics of photonic crystal waveguides with heterodyne scanning near-field optical microscopy' OSA Topical Meeting on Nanophotonics for Information Systems, San Diego, CA, USA, April 13-15, 2005.
- P. Tortora,W. Nakagawa, L.Vaccaro, R. Dndliker, 'Scanning Probe 3D Polarization Coupling Properties', The 8-th International Conference on Near-Field Optics & Related Techniques (NFO-8), Technical Digest p. 94, Seoul, Korea (2004).

Bibliography

[1] E.H. Synge, "A suggested method for extending microscopic resolution into the ultramicroscopic region", Philos. Mag. **6**, 356-362 (1928).

[2] Lewis, A. Isaacson, M. Harootunian, A. Muray, A. "Development of a 500-Å spatial-resolution light-microscope" Biophys. J. **41**, 405406 (1983).

[3] D. W. Pohl, W. Denk and M. Lanz, "Optical stethoscopy: image recording with resolution $\lambda/20$", Appl. Phys. Lett. **44**, 651-653 (1984).

[4] O.J.F. Martin, C. Girard, A. Dereux, "Generalized Field Propagator for Electromagnetic Scattering and Light Confinement", Phys. Rev. Lett. **74**, 526-529 (1995).

[5] M. Xiao, "Polarization effects in reflection scanning near field optical microscopy", Opt. Comm. **74**, 213-218 (1997).

[6] K. Nakajiima *et al.*, "Polarization effect in scanning near-field optic/atomic-force microscopy (SNOM)/AFM)", Ultramicroscopy **74**, 257-262 (1998).

[7] Interesting presentations have recently been held on these subjects at "European Optical Society Advanced Imaging Tecnique Topical Meeting", London 29 June-1 July 2005.

[8] J.F. Nye and J.V. Hajnal, "The wave structure of monochromatic electromagnetic radiation", Proc. R. Soc. Lond. A **409**, 21-36 (1987).

[9] M.A. Johnson, C.H. Towes, " Quantum effects and optimization of heterodyne detection", Opt. Commun. **179**, 183-187 (2000).

[10] M.A. Paesler, P.J. Moyer,"Near Field Optics: Theory, Instrumentation, and Applications", Wiley, New York, 1996.

[11] D. Courjon *et al.*,"External and internal reflection near field microscopy experiments and results", Appl. Opt. **29**, 3734-3740 (1990).

[12] J.M. Guerra, "Photon tunneling microscopy", Appl. Opt. **29**, 3741-3752 (1990).

[13] D. W. Pohl, D. Courjon (Eds),"Near Field Optics", Kluver, Dordrecht (1993).

[14] K. Kaufmann,"Choosing Your Detector", SPIE's *oe*magazine, March 2005.

[15] M. Vaez-Ivarani and R. Toledo-Crow,"Phase contrast and amplitude pseudoheterodyne interference near field scanning optical microscopy", Appl. Phys. Lett. **62**,1044-1046 (1993).

[16] P.L Phillips *et al.*,"Direct measurement of optical phase in the near field", Appl. Phys. Lett. **76**,541-543 (1999).

[17] M.L.M. Balistreri *et al.*,"Local observation of phase singularities in optical fields in waveguide structures", Phys. Rev. Lett. **85**,294-297 (2000).

[18] M.L.M. Balistreri *et al.*, "Quasi interference of perpendicularly polarized guided modes observed with a photon scanning tunneling microscope", Opt. Lett. **25**, 637-639 (2000).

[19] A. Nesci, R. Dändliker, M. Salt, H-p. Herzig," Optical near-field phase singularities produced by microstructures", Proceed. of SPIE **4456**,68-77 (2001).

[20] G.P. Agrawal, "Fiber-optic communication systems", John Wiley & Sons, Inc., USA (1992).

[21] See, for example, A. Yariv, "Optical Electronics, 3rd ed. (Holt, Rinehart and Winston, New York (1985).

[22] R. Dändliker, "Heterodyne holographic interferometry", in Progress in Optics, E. Wolf, ch.1, North-Holland Ed., Amsterdam, The Netherlands (1980).

[23] P.S. Theocaris, E.E. Gdouts," Matrix Theory of Photoelasticity", Springer Series in Optical Science, Vol.11, edited by D.L. MacAdam (1979).

[24] (See for a review)D. Marcuse, "Light transmission Optics", Van Nostrand Reinhold Company Inc., New York (1982).

[25] S.I. Bozhevolnyi, B. Vohnsen, E.A. Bozhevolnya,"Transfer function in collecting near-field optical microscopy", Opt. Comm. **172**, 171-179 (1999).

[26] Courtesy of A.Nesci,"Measuring amplitude and phase in optical fields with sub-wavelength features", UFO Atelier fr Gestaltung & Verlag GbR, Allensbach (2001).

[27] J.W. Goodman,"Introduction to Fourier Optics", McGraw-Hill, New York (1996).

[28] D.P. Tsai *et al.*,"Estimating the effective optical aperture of a tapered laser probe in PSTM imaging",Proc. SPIE Int. Soc. Opt. Eng. **1855**, 93 (1993).

[29] A.J. Meixner *et al.*,"Direct measurement of standing evanescent waves with a photon-scanning tunnelling microscope", Appl. Opt. **33**, 7995 (1994).

[30] R. Carminati and J.J. Greffet, "Two dimensional numerical simulation of the photon scanning tunnelling microscope. Concept of transfer function", Opt. Comm. **116**, 316-321 (1995).

[31] P. Blattner, H.P. Herzig, R. Dndliker,"Scanning near-field microscopy: transfer function and resolution limit" Opt. Comm. **155**, 224-250 (1998).

[32] D. Barchiesi, "Pseudo modulation transfer function in reflection scanning near-field optical microscopy", Opt. Comm. **154**, 167-172 (1998).

[33] D. Van Labeke and D. Barchiesi,"Probes for scanning tunnelling optical microscopy: a theoretical comparison", J. OPt. Soc. Am. A **10**, 2193 (1993).

[34] R.L. Williamson *et al.*,"Are artefacts in scanning near-field optical microscopy related to the misuse of shear force?", Ultramicroscopy **71**, 165-175 (1998).

[35] J.N. Walford *et al.*,"Influence of tip modulation on image formation in scanning near-field optical microscopy", J. Appl. Phys. **89**, 5159-5169 (2001).

[36] S.I. Bozhevolnyi, 'Topographical artifacts and optical resolution in near-field optical microscopy", J. Opt. Soc. Am. B **14**, 2254-2259 (1997).

[37] M. Nevire and P. Vincent, in: "Near Field Optics", eds. D.Pohl and D. Courjon, Kluwer Dordrecht, p.337 (1993).

[38] N. Garcia and M. Nieto-Vesperinas," Ner-field optics inverse-scattering reconstruction of reflective surfaces", Opt. Lett. **18**, 2090 (1993).

[39] R. Carminati *et al.*,"Electromagnetic wave scattering from a cylinder in front of a conducting surface-relief grating", Opt. Comm. **111**, 26-33 (1994).

[40] F. de Fornel *et al.*,"Analysis of image formation with a photo scanning tunnelling microscope"J. Opt. Soc. Am. A **13**, 35 (1996)

[41] J.J. Greffet and R. Carminati," Image formation in neqar-field Optics", Prog. Surf. Sci. **56**, 133 (1997).

[42] J. J Stamnes,"Waves in focal regions", Adam Hilger Impr., Bristol, USA (1986).

[43] A. Nesci, R. Dndliker, and H-P. Herzig,"Quantitative amplitude and phase measurement by use of heterodyne scanning near-field optical microscope", Opt. Lett. **26**, 208-210 (2001).

[44] L. Vaccaro, L. Aeschimann, U. Staufer, H. P. Herzig and R. Dändliker, "Propagation of the electromagnetic field in fully coated near-field optical probes", Appl. Phys. Lett. **83**, 584-586 (2003).

[45] A. Nesci, R. Dändliker, M. Salt, and H.P. Herzig,"Measuring amplitude and phase distribution of fields generated by gratings with sub-wavelength resolution",Opt. Comm. **205** ,229-238 (2002).

[46] A. Bouhelier, M.R. Beversluis, L. Novotny ,"Ner-field scattering of longitudinal fields" Appl. Phys. Lett. **205**, 4596-4598 (2003).

[47] T. Grosjean, D. Courjon, D. Van Lebeke,"Bessel beams as virtual tips for near-field optics", Journal of Microscopy **210**, 319-323 (2003).

[48] E. Descrovi *et al.*," On the coupling and transmission of longitudinal fields into fully metal-coated optical nano-probes", Appl. Phys. Lett. **85**, 5340-5342 (2004).

[49] R. Dändliker, P. Tortora, L. Vaccaro, A. Nesci,"Measuring three-dimensional polarization with scanning optical probes", J. Opt. A, Pure Appl. Opt **6**, S18-S23 (2004).

[50] K. Okamoto, "Foundamental of Optical Waveguides", Academic Press, USA (2000).

[51] R. F. Harrington,"Time-Harmonic Electromagnetic Fields, McGraw Hill, New York, New York (1961).

[52] L. Novotny and C. Hafner," Light propagation in a cylindrical waveguide with a complex, mettallic, dielectric function", Phys. Review E **50**, 4094-4106 (1994).

[53] T. Yatsui *et al.*,"Metalized pyramidal silicon probe with extremely high troughput and resolution capability for optical near-field technology", Appl. Phys. Lett. **80**, 2257-2259 (2002).

[54] R. Eckert *et al.*,"Near-field flourescence imaging with nm resolution based on microfabricated cantilevered probes", Appl. Phys. Lett. **77**, 3695 (2000).

[55] L. Aeschimann, T. Akiyama, U. Staufer, N. F. de Rooij, L. Thiery, R. Eckert and H. Heinzelmann, "Characterization and fabrication of fully metal-coated scanning near-field optical microscopy SiO_2 tips", J. Microscopy **209**, 182-187 (2003).

[56] E. Descrovi, L. Vaccaro, L. Aeschimann, W. Nakagawa, U. Staufer and H. P. Herzig, "Optical properties of microfabricated fully metal-coated near-field probes in collection mode," J. Opt. Soc. Am. A, (*in press*).

[57] B. Hecht *et al.*,"Scanning near-field optical microscopy with aperture probes: Fundamentals and applications", J. of Chem. Phys. **12**, 7761-7774 (2000).

[58] L. Novotny *et al.*,"Scanning near-field optical probe with ultrasmall spot size", Opt. Lett. **20**, 970 (1995).

[59] J. Michaelis *et al.*, "A single molecule as a probe of optical intensity distribution", Opt. Lett. **24**, 581-583 (1999).

[60] V. Sandoghdar and J. Mlynek,"Prospects of aperturless SNOM with active probes", J. Opt. A **24**, 523-530 (1999).

[61] V. Sandoghdar *et al.*, "Results and Thoughts on Optical Microscopy Using a Single-molecule Probe", Single. Mol. **2**, 277-281 (2001).

[62] A. Bouhelier *et al.*, "Plasmon-coupled tip-anhanced near-field optical microscopy", J. Microsc. **210**, 220-224 (2002).

[63] F. Keilmann, "Surface-polariton propagation for scanning near-field optical microscope", J. Microsc. **194**, 567 (1999).

[64] L. Novotny *et al.*,"Scanning near-field optical probe with ultrasmall spot size", Opt. Lett. **20**, 970-972, (1995).

[65] H. Raether, "Surface Plasmons. Springer Tracts in Modern Physics III." Springer-Verlag, Berlin (1988).

[66] P. Hariharan, B. F. Oreb, and T. Eiju, "Digital phase-shifting interferometry: a simple error-compensating phase calculation algorithm", Appl. Opt. **26**, 2504–2506 (1987).

[67] M. Stalder and M. Schadt, "Linearly polarized light with axial symmetry generated by liquid-crystal polarization converters", Opt. Lett. **21**, 1948–1950 (1996).

[68] M.A. Lieb and A.J. Meixner,"A high numerical aperture parabolic mirror as imaging device for confocal microscopy", Opt. Express **8**,458-474 (2001).

[69] M. Born, E. Wolf, "Principle of Optics", Cambridge University Press, 7^{th} edition, Cambridge (UK) (1999).

[70] N. Chiba *et al.*,"Observation of Topography and Optical Image of Optical Fiber End by Atomic Force Mode Scanning Near-Field Optical Microscope", J. Appl. Phys. **34**, 321-324 (1995).

[71] R.L. Williamson *et al.*, "Are artefacts in scanning near-field optical microscopy related to the misuse of shear force?", Ultramicroscopy **34**, 165-175 (1998).

[72] I. Märki, M. Salt, H-P. Herzig,"Practical and theoretical analysis of photonic crystal waveguides", J. Appl. Phys. **96**, 7-11 (2004).

[73] S.G. Johnson, P.R. Villeneuve, S. Fan, J.D. Joannopoulos," Linear waveguide in photonic-crystal slabs", Phys. Rev. B **62**, 8212-8222 (2000).

[74] I. Märki, M. Salt, R. Stanley, U. Staufer, H. P. Herzig, "Characterization of photonic crystal waveguides based on Fabry-Prot interference", J. Appl. Phys. **96**, 6966-6969 (2004).

[75] S.G. Johnson, A. Mekis, S. Fan and J.D. Joannoupulos,"Molding the flow of light", Comput. in Sci. Eng. **38**, 38-47 (2001).

[76] X. Letartre *et al.*, "Group velocity and propagation losses measurement in a single-line photonic-crystal waveguide on InP membranes", Appl. Phys. Lett. **79**, 2312-2314 (2001).

[77] J.D. Joannopoulos, R.D. Meade, J.N. Winn, "Photonic Crystals", Princeton Univesrity Press, Princeton, New Jersey (US) (1995).

[78] A. Sakai, G. Hara and T. Baba, "Propagation Characteristics of Ultrahih-Δ Optical Waveguide On Silicon-on-Insulator Substrate", Jpn. J. Appl. Phys. **40**, L383-L385 (2001).

[79] A. Mekis *et al.*,"High transmission through sharp bends in photonic crysatl waveguides ", Phys. Rev. Lett **77**, 3787 (1996).

[80] T. Baba, N. Fukaya and J. Yonekura, "Observation of light propagation in photonic crystal optical waveguides with bends", IEEE Electr. Lett. **35**, 654-655 (1999).

[81] E. Yablonovitch, "Inhibited Spontaneous Emission in Solid-State Physics and Electronics", Phys. Rev. Lett. **58**, (1987).

[82] S. John, "Strong Localization of Photons in certain Disordered Dielectric Superlattices", Phys. Rev. Lett. **58**, 2486-2489 (1987).

[83] S.G. Johnson and J.D. Joannoupulos,"Bloch-Iterative Frequency-Domain for Maxwell's Equations in a Planewave Basis", Optics Express **8** 173-190 (2001).

[84] R.D. Maede *et al.*,"Accurate Theoretical Analysis of Photonic Band-Gap Materials", Phys. Rev. B **48**, 8434-8437 (1993).

[85] E. Ozbay *et al.*," Physics and applications of photonic crystals", Phot. and Nanostr.- Fund. and Applic. **2**, 87-95 (2004).

[86] G.K. Celler and S. Cristoloveanu, "Frontiers of silicon-on-insulator", J. Apll. Phys. **93**, 4599-4978 (2003).

[87] E Flük *et al.*, "Amplitude and Phase evolution of optical Fields Inside Periodic Photonic Strctures", J. Lightwave Tech. **21(5)**, 1384-1393 (2003).

[88] J.C. Gates *et al.*, "Structure and propagation of modes of large area holey fibers", Optics Express **12** 847-852 (2004).

[89] H. Stefanon *et al.*, "Heterodyne detection of guided waves using a scattering-type Scanning Near-Field Optical Microscopy ", Optics Express **13** 5553-5664 (2005).

[90] H. Gersen *et al.*, "Real-Space Observation of Ultraslow Light in Photonic Crystal Waveguides ", Phys. Rev. Lett. **94** (073903-1)-(073903-4) (2005).

[91] H. Gersen *et al.*, "Direct Observation of Bloch Harmonics and Negative Phase velocity in photonic Crystal Waveguides ", Phys. Rev. Lett. **94**, (123901-1)-(123901-3) (2005).

[92] P. Tortora, M. Abashin, I. Mä, W. Nakagawa, L. Vaccaro, M. Salt, H-P Herzig, U. Levy, Y. Fainman, "Observation of amplitude and phase in ridge and photonic crystal waveguides operating at $1.55\mu m$ by use of heterodyne scannijng near field optical microscopy", Opt. Lett. **30**, (???) (2005). *In press.*